AD-A066 741 COMPUTER GENETICS CORP WAKEFIELD MASS F/G 8/10
SUMMARY AND EXPERIMENTAL PLAN FOR REMOTE SENSING OF SUBSURFACE --ETC(U)
JUL 77 D A LEONARD, B CAPUTO N00014-76-C-1007
UNCLASSIFIED CGC-RN105-77 NL

1 OF 2
ADA
066741

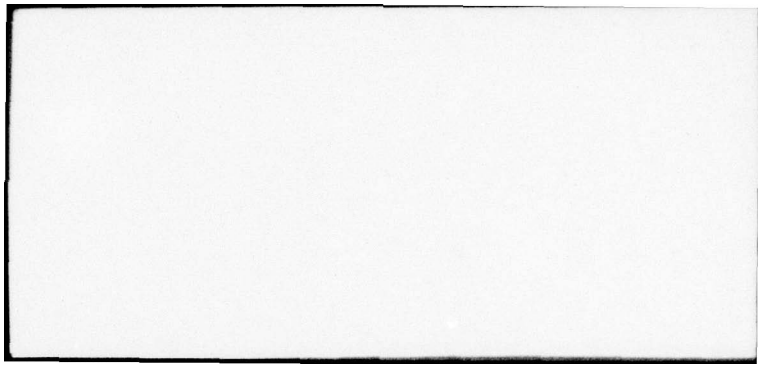

(2)

LEVEL II

Interim Report
CGC-RN105-77

AD A066741

DDC FILE COPY

SUMMARY AND EXPERIMENTAL PLAN FOR REMOTE SENSING OF SUBSURFACE TEMPERATURE AND SALINITY

by

D. A. Leonard and B. Caputo

Computer Genetics Corporation
Wakefield, Massachusetts

July 1977

Prepared For:

Office of Naval Research
800 N. Quincy Street
Arlington, Virginia 22217

SECURITY CLASSIFICATION OF THIS PAGE (When Data Entered)

REPORT DOCUMENTATION PAGE

READ INSTRUCTIONS BEFORE COMPLETING FORM

1. REPORT NUMBER: CGC-RN105-77 Summary
2. GOVT ACCESSION NO.
3. RECIPIENT'S CATALOG NUMBER

4. TITLE (and Subtitle): STUDY AND EXPERIMENTAL PLAN FOR REMOTE SENSING OF SUBSURFACE TEMPERATURE AND SALINITY
5. TYPE OF REPORT & PERIOD COVERED: Interim Report covering the period 1 Jul 31 Oct 76
6. PERFORMING ORG. REPORT NUMBER

7. AUTHOR(s): D. A. Leonard and B. Caputo
8. CONTRACT OR GRANT NUMBER(s): N00014-76-C-1007 NW

9. PERFORMING ORGANIZATION NAME AND ADDRESS
Computer Genetics Corporation
18 Lakeside Office Park
Wakefield, Massachusetts 01880

10. PROGRAM ELEMENT, PROJECT, TASK AREA & WORK UNIT NUMBERS

11. CONTROLLING OFFICE NAME AND ADDRESS
Office of Naval Research
800 N. Quincy Street
Arlington, Virginia 22217

12. REPORT DATE: July 1977
13. NUMBER OF PAGES: 105

14. MONITORING AGENCY NAME & ADDRESS (if different from Controlling Office): 12 10 Mp

15. SECURITY CLASS. (of this report): UNCLASSIFIED
15a. DECLASSIFICATION/DOWNGRADING SCHEDULE: N/A

16. DISTRIBUTION STATEMENT (of this Report)

DISTRIBUTION STATEMENT A
Approved for public release; Distribution Unlimited

17. DISTRIBUTION STATEMENT (of the abstract entered in Block 20, if different from Report)

18. SUPPLEMENTARY NOTES

19. KEY WORDS (Continue on reverse side if necessary and identify by block number)
Water Temperature
Salinity
Subsurface
Remote Sensing
Raman Lidar

20. ABSTRACT (Continue on reverse side if necessary and identify by block number)

The temperature and salinity of liquid water can be inferred from its Raman spectrum. This report assesses and evaluates the prominent factors which influence the ability of a remote sensing Raman lidar to measure subsurface profiles of water temperature and salinity. A plan is developed for the experimental investigation of the feasibility of the technique in ocean and coastal waters. Interferences, including surface wave effects, differential attenuation, differential depolarization and fluorescence are considered.

CONT' over

DD FORM 1 JAN 73 1473 EDITION OF 1 NOV 65 IS OBSOLETE

SECURITY CLASSIFICATION OF THIS PAGE (When Data Entered)

391 873

20. Abstract. (Con't)

CONT'

Preliminary experimental data taken from a boat in the natural coastal environment are also reported.

TABLE OF CONTENTS

Section			Page
1.0	INTRODUCTION AND SUMMARY		1
2.0	PHYSICAL BASIS OF EXPERIMENT AND PRIOR WORK		2
3.0	NEW WORK ACCOMPLISHED UNDER SUBJECT CONTRACT		5
	3.1	Major Interferences and Noise Sources	5
		3.1.1 Surface Wave Effects	5
		3.1.1.1 Differential Transmission of Orthogonal Linear Polarization	6
		3.1.1.2 Depth Resolution	12
		3.1.1.3 Lateral Resolution	14
		3.1.2 Volume Transmission Phenomena	17
		3.1.2.1 Differential Depolarization-Experimental	17
		3.1.2.2 Differential Depolarization-Theoretical	21
		3.1.2.3 Differential Attenuation and the Need for Multiwavelength Polarization Detection	24
		3.1.3 Non-Raman Photon Sources	28
		3.1.3.1 Ambient Light Background	28
		3.1.3.2 Laser Induced Fluorescence	29
	3.2	Detailed Experimental Apparatus Design	30
		3.2.1 Laser Raman Spectrometer for Field Utilization	30
		3.2.2 Research Vessel Facility	32
		3.2.3 Preliminary Experimental Raman Data Obtained From Natural Waters	37
	3.3	Experimental Field Test Plan	41
		3.3.1 Experimental Objectives and Methods	43
		3.3.1.1 Transmission (i.e. K)	43
		3.3.1.2 Fluorescence to Raman Ratio (F)	43
		3.3.1.3 Differential Polarization Analysis	43
		3.3.1.4 Proportionality Between ρ_s and K	43
		3.3.1.5 Temperature vs. Salinity Separability	44
		3.3.2 Sea Truth Requirements	44
		3.3.2.1 Sea Truth Measurement Parameters	45
		3.3.3 Test Site Requirements	46
		3.3.3.1 Water Quality	46
		3.3.3.2 Salinity	47
	3.4	Q & A on Fundamental and Planned Experimental Techniques	62

TABLE OF CONTENTS
(Continued)

Section		Page
4.0	CONCLUSIONS AND RECOMMENDATIONS	67
	REFERENCES	70
	APPENDIX A - Physical and Mathematical Justification	A1 - A8
	APPENDIX B - Computer Program to Determine the Effect of Ocean Surface Wave Shape on Differential Transmission of Orthogonal Polarizations	B1 - B5
	APPENDIX C - Computer Program to Determine the Effect of Ocean Surface Waveshape on Refractive Depth Penetration Correction	C1 - C8
	APPENDIX D - Depolarization Calculations	D1 - D3
	APPENDIX E - Experimental Remote Sensing of Subsurface Temperature In Natural Ocean Water (CGC Research Note 102)	E1 - E4

LIST OF ILLUSTRATIONS

Figure		Page
3-1	Air-Water Interface Geometry in the Plane of Incidence	6
3-2	Differential Polarization vs. Incident Angle	10
3-3	Differential Transmission of Orthogonal Linear Polarizations Averaged Over Various Wave Spectra	11
3-4	Geometrical Optics for Wave Refraction Depth Correction and Lateral Error Correction	13
3-5	Fractional Error in Depth Measurement Due to Refraction as Function of H/L for Stokes, Trochoidal and Sinusoidal Waves	15
3-6	Fractional Error in Depth Measurement Due to Refraction as Function of H/L for Stokes Waves Showing Average, 90% and Maximum Values	16
3-7	Depolarization During Transmission Through Natural Waters Obtained by S. Q. Duntley	18
3-8	Differential Attenuation vs. Wavelength Separation With Depth as a Parameter (K Minimum)	26
3-9	Differential Attenuation vs. Wavelength Separation With Depth as a Parameter (100 Å From K Minimum)	27
3-10	Functional Block Diagram of Dual Polarization Raman Spectrometer	31
3-11	Bistatic Laser Raman Equipment Aboard the Research Vessel Makai	34
3-12	Block Diagram of Laser Raman System Currently Operational on Research Vessel Makai	35
3-13	Bistatic Laser Raman Equipment in the Laboratory	36
3-14	Bistatic Laser Raman Equipment Aboard the Research Vessel Makai	38
3-15	Raman Spectral Data for Liquid Water	40
3-16	Schedule and Plan for Raman Temperature/Salinity Research	42
3-17	Map of Northern Massachusetts and New Hampshire Coastal Region	48
3-18	R/V Berth Near Blyman Canal	55
3-19	R/V Berth and Annisquam River	56
3-20	Gloucester Harbor, Raw Sewage Outlet	57
3-21	Deep (56') "Clear" Water Hole Off Coffins Beach	58
3-22	Deep Open Waters Off Castle Neck	59
3-23	Merrimack River Test Site	60
3-24	Sheltered Shakedown Area	61

LIST OF ILLUSTRATIONS

Figure		Page
A-1	Raman Spectrum and Structure of Liquid Water	A2
1	Block Diagram of Laser Raman System Currently Operational on Research Vessel Makai	E3
2	Raman Spectral Data for Liquid Water	E3
3	Typical System Operating Map (100 Meter Mixed Layer)	E4

LIST OF TABLES

Table		Page
2-1	Comparison of Raman and Volume Scattering Coefficients for Water	4
3-1	Sample Calculation Results for Depolarization During Transmission	20
3-2	Water Discharge Data of Merrimack River Below Concord River at Lowell, Massachusetts in CFS (cubic feet per second)	49
3-3	Climatological Table	52
3-4	Mean Surface Water Temperatures (T) and Densities (D)	53
3-5	Meteorological Table for Coastal Area Off Boston	54
A-1	Baseline System Parameters	A6
A-2	Underwater Windows for Various Ocean Waters	A7

1.0 INTRODUCTION AND SUMMARY

This report summarizes the work accomplished on Contract N00014-76-C-1007 Task I during the period 1 July 1976 to 31 October 1976. The effort concentrated on planning and studying the experimental investigation of the feasibility of applying Raman spectroscopy to obtain subsurface temperature and salinity information in ocean and coastal waters.

A critical review and study was made of the proposed experimental plan described in Computer Genetics Corporation proposal CGC-P121-76 dated April 1976. The calculations and assumptions upon which the experiment is based were expanded, reviewed and with the exception of a newly measured[1] and larger value for the basic cross-section, were found to be consistent with current information.

Much of the new work performed on Contract N00014-76-C-1007 centered on the identification and quantification of the various interferences and noise sources that could limit system performance and which have been quantitatively evaluated with reassuring results.

Areas requiring new and supplemental experimental attention to develop the technique have been identified and a broad as well as detailed experimental plan has been written. An existing government owned apparatus configuration was used to obtain the first Raman data spectrum taken from a boat in the natural coastal environment. The temperature obtained from the spectrum agreed with prior laboratory calibration and the measured fluorescence to Raman ratio was very much less than unity. A preferred configuration which can be readily assembled from additional existing government inventory is presented.

The refractive effects of surface waves related to differential polarization transmission and depth correction were studied and computer programs were written and exercised which show less than a 1.0°C offset in the temperature measurement and less than a few ppt in salinity measurements even if uncorrected. The major limiting factors in depth resolution have been identified as laser pulse duration and the random refractive effects at the air water interface. The former effect is reduced with advanced laser design, while through computer calculation the latter effect appears to stabilize as a 0.1 to 0.3 percent effect.

Depolarization during transmission through natural waters has been studied and the concensus based upon prior work of several investigators is that over 80% of the original polarization remains after traversing 20 attenuation lengths. Also it has been calculated that if the proportionality between the depolarization coefficient ρ_s and the diffuse attenuation coefficient K can be known to within 10%, that after corrections are applied, accuracies of 0.16°C in temperature and 0.7 ppt in salinity per attenuation length can be expected. This means, for example, that at a depth of three attenuation lengths a temperature uncertainty of 0.48°C and a salinity uncertainty of 2.1 parts per thousand would be expected. The range of temperature and salinity considered was -2°C to 35°C and 0 ppt to 40 ppt respectively.

Through computer simulation, tables have been generated to relate the theoretical accuracy of the polarization ratio measurement to spectrometer bandwidth and multiwavelength detection as a function of differential attenuation.

A well researched and documented initial test site which offers a representative cross-section of water quality and natural coastal effects such as sediment loading, salt water intrusion, thermal gradients, etc. is discussed in detail.

This Technical Summary Report highlights the results of the effort. Supporting technical references, computer calculation printouts, design information, component specification and cost backup is on file in various formats at the CGC office in Wakefield, Massachusetts.

2.0 PHYSICAL BASIS OF EXPERIMENT AND PRIOR WORK

The physical basis for the Raman measurement of subsurface temperature and the prior work upon which the current program is based were described in Computer Genetics Proposal CGC-P121-76 dated April 1976. Appendix A of this report repeats the basic information relating to the physical basis and mathematical justification as it appeared in that proposal.

During the course of the literature search performed as part of the new work conducted on Contract N00014-76-C-1007 another more recently measured value for the basic liquid water Raman cross-section was discovered. A paper entitled, "Temperature Dependence and Cross-Sections of Some Stokes and Anti-Stokes Raman Lines in Ice" by Slusher and Derr[1] also reports an experimentally measured value for the liquid water Raman cross-section of $4.5 \times 10^{-33} m^2$/molecule sr. This cross-

section value is approximately a factor of five higher than the value that appeared in an older reference[2] and which has previously served as the basis for our system performance calculations.

In a private conversation with Derr concerning the liquid water cross-section measurements he expressed the opinion that he was not aware of the prior work.[2] He did feel that his own work was accurate to probably much better than a factor of five. Derr also pointed out that it is common for liquid phase Raman cross-sections to be much larger than gas phase even on a per molecule basis and the fact that this is true for water was not surprising.

Table 2-1 shows a representative, but by no means complete, compilation of volume backscattering coefficients that have been measured by various investigators for distilled water and ocean and lake water of various types. Also included in Table 2-1 are Raman backscattering coefficients for distilled water and ice. The wavelength of light used for the measurements cited in Table 2-1 varies somewhat from investigator to investigator, but all use light in the blue-green near 500 nm so that order of magnitude comparisons may be considered valid.

From the data compiled in Table 2-1 it can be noted that the new Slusher and Derr value for the Raman coefficient is essentially equal to the on-frequency backscatter coefficient of Tyler for distilled water. Far from being a "weak" effect the Raman is comparable to the main on-frequency return from the water itself.

This has implications when making comparisons between the Raman method and other laser scattering methods for remote subsurface measurements such as the recently suggested[8] Brillouin measurements to determine sound speed.

It should also be noted that the cross-section for ice is comparable to that of liquid water. Slusher and Derr[1] have obtained temperature measurements using Stokes to anti-Stokes line ratios in ice from $0^{\circ}C$ to $-50^{\circ}C$. A Raman instrument capable of measuring temperature and salinity should also be capable not only of detecting ice but also of measuring ice temperatures.

TABLE 2-1

Comparison of Raman and Volume Scattering Coefficients for Water

	Raman Scattering Coefficient, (λ = 488 nm) (Meters^{-1} Steradian^{-1})	
Distilled Water	.00003	Chang and Young(1974)[2]
	.00015	Slusher and Derr(1975)[1]
Ice	.000093	Slusher and Derr(1975)[1]

	Volume Scattering Coefficient, σ (180°) (Meters^{-1} Steradian^{-1})	
Distilled Water	.00017-.00020	Tyler(1961)[3]
Ocean		
Various Locations, Eastern North Atlantic	.0005	Jerlov(1961)[4]
Off Bermuda (31° 57'N, 65° 11' W)	.002	Morrison(1970)[5]
Coastal		
Between Woods Hole and the 180 m Contour	.003-.004	Spilhaus(1968)[6]
Near Santa Catalina Island (33° 32'N, 118° 17'W)	.00020	Tyler(1961)[3]
Long Island Sound (41° 16'N, 70° 08'W)	.02	Morrison(1970)[5]
Lake		
Winnipesaukee, New Hampshire	.003	Duntley(1963)[7]
Pend Oreille, Idaho	.0017-.0041	Tyler(1961)[3]

3.0 NEW WORK ACCOMPLISHED UNDER SUBJECT CONTRACT

This section of this Technical Summary Report summarizes the work accomplished on Contract No. N00014-76-C-1007 during the four month period 1 July 1976 to 31 October 1976. The effort concentrated on planning and studying the experimental investigation of the feasibility of applying Raman spectroscopy to obtain subsurface temperature and salinity information in natural ocean and coastal waters.

The effort included literature searches, interviews with key personnel in the ocean sciences area, theoretical calculations including the development and utilization of several new computer routines, a survey of the availability and the coordination of the utilization of Government property in a laser Raman coastal experiment, the planning of specific experimental apparatus designs and specific test plans, and the analysis and interpretation of preliminary field data.

This Technical Summary Report highlights the results of the effort. Supporting technical references, computer calculation printouts, design information, component specification and cost backup are on file in various formats at the CGC office in Wakefield, Massachusetts.

3.1 Major Interferences and Noise Sources. An important aspect of the effort was to identify and quantify the major interferences and noise sources that laser Raman spectroscopic measurements of subsurface ocean temperature and salinity would encounter. The purpose was to ensure that subsequent experiments would be properly designed and planned so that the significant questions concerning interferences and noise sources could be adequately answered.

The following subsections summarize the interferences and noise sources as follows: Section 3.1.1 describes surface wave effects both as they influence the depth resolution, and also as a depolarization noise source; Section 3.1.2 describes the volume transmission phenomena of differential attenuation and differential depolarization; and Section 3.1.3 describes the influence of non-Raman photon sources such as fluorescence and ambient backgrounds.

3.1.1 Surface Wave Effects. The effect of surface waves were found to relate in three significant ways to the subsurface measurement of temperature and salinity. These are (a) the differential transmission of orthogonal linear polarizations through the air-water interface, (b) the loss of depth resolution

due to variable refraction angles produced at a wavy water surface and (c) lateral error due to the same variable refraction angles.

3.1.1.1 Differential Transmission of Orthogonal Linear Polarization. The differential transmission of orthogonal linear polarizations through an oblique air-water interface in terms of typical wave spectra was investigated by means of "exact" one-dimensional calculations on an IBM 360 computer. New computer routines were written which used the basic Fresnel refraction equations.[9] Sinusoidal as well as finite amplitude[10] trochoidal and "Stokes" waves were employed in the program. The effect of variable crest height to wavelength ratios was investigated in order to study the effect of sea state on the measurement.

The results showed that even at the worst case sea state condition of a Stokes limit[10] wave amplitude peak-to-peak to wavelength (H/L) ratio of 0.143 the effect is to introduce a bias of less than 1.0% in the Raman depolarization ratio measurement. This would mean less than a 1.0°C off-set in the temperature measurement or a few parts per thousand error in the salinity measurement if uncorrected. It was, therefore, concluded that in the initial experimental configuration no attempt should be made to improve the accuracy by correlation on a pulse-to-pulse basis of the wave angle, an average over a given wave spectra being adequate for initial experimental investigation.

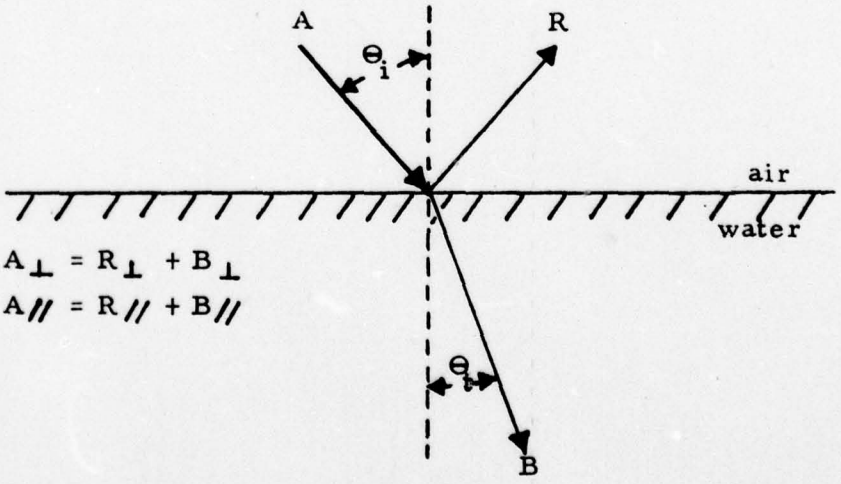

Figure 3-1. Air-Water Interface Geometry in the Plane of Incidence.

The details of the calculation are illustrated in Figure 3-1 which shows the air-water plane of incidence with the incident light of intensity A shown at an angle θ_i with respect to the normal to the air-water interface. The reflected ray R and the refracted ray B at angle θ_t are also shown.

Using the Fresnel refraction equations in the form:[9]

$$R_{//} = \frac{\tan^2 (\Theta_i - \Theta_t)}{\tan^2 (\Theta_i + \Theta_t)} \qquad R_{\perp} = \frac{\sin^2 (\Theta_i - \Theta_t)}{\sin^2 (\Theta_i + \Theta_t)}$$

the differential transmission of polarization through the surface, i.e. $B_{//} - B_{\perp} / B_{\perp} \equiv \Delta B / B_{\perp}$ can be easily derived from the conservation equations $B_{//} = 1 - R_{//}$ and $B_{\perp} = 1 - R_{\perp}$ as follows:

$$B_{//} = A_{//} - R_{//} = 1 - R_{//} = 1 - \frac{\tan^2 (\Theta_i - \Theta_t)}{\tan^2 (\Theta_i + \Theta_t)}$$

$$B_{\perp} = A_{\perp} - R_{\perp} = 1 - R_{\perp} = 1 - \frac{\sin^2 (\Theta_i - \Theta_t)}{\sin^2 (\Theta_i + \Theta_t)}$$

$$\Delta B = B_{//} - B_{\perp} = \frac{\sin^2 (\Theta_i - \Theta_t)}{\sin^2 (\Theta_i + \Theta_t)} - \frac{\tan^2 (\Theta_i - \Theta_t)}{\tan^2 (\Theta_i + \Theta_t)}$$

$$\frac{\Delta B}{B_{\perp}} = \frac{\dfrac{\sin^2 (\theta_i - \theta_t)}{\sin^2 (\theta_i + \theta_t)} - \dfrac{\tan^2 (\theta_i - \theta_t)}{\tan^2 (\theta_i + \theta_t)}}{1 - \dfrac{\sin^2 (\theta_i - \theta_t)}{\sin^2 (\theta_i + \theta_t)}}$$

$$\frac{\Delta B}{B_\perp} = \frac{\sin^2(\theta_i - \theta_t)\left[1 - \frac{\cos^2(\theta_i + \theta_t)}{\cos^2(\theta_i - \theta_t)}\right]}{\sin^2(\theta_i + \theta_t) - \sin^2(\theta_i - \theta_t)}$$

$$\frac{\Delta B}{B_\perp} = \tan^2(\theta_i - \theta_t)\left[\frac{1 - \sin^2(\theta_i - \theta_t) - 1 + \sin^2(\theta_i + \theta_t)}{\sin^2(\theta_i + \theta_t) - \sin^2(\theta_i - \theta_t)}\right]$$

$$\frac{\Delta B}{B_\perp} = \tan^2(\theta_i - \theta_t)$$

The effect of oblique transmission through an air-water interface is thus to produce differential transmission of orthogonal linear polarizations. If the incident light is a pure circular polarization mode, the effect will be to produce elliptical light.

The quantitative nature of the effect is shown in Figure 3-2, which is a plot of the differential polarization produced by oblique transmission through an air-water interface, vs. the incident angle, θ_i. As shown, the effect is "negligible" for small angles and becomes nearly unity at angles approaching 90°.

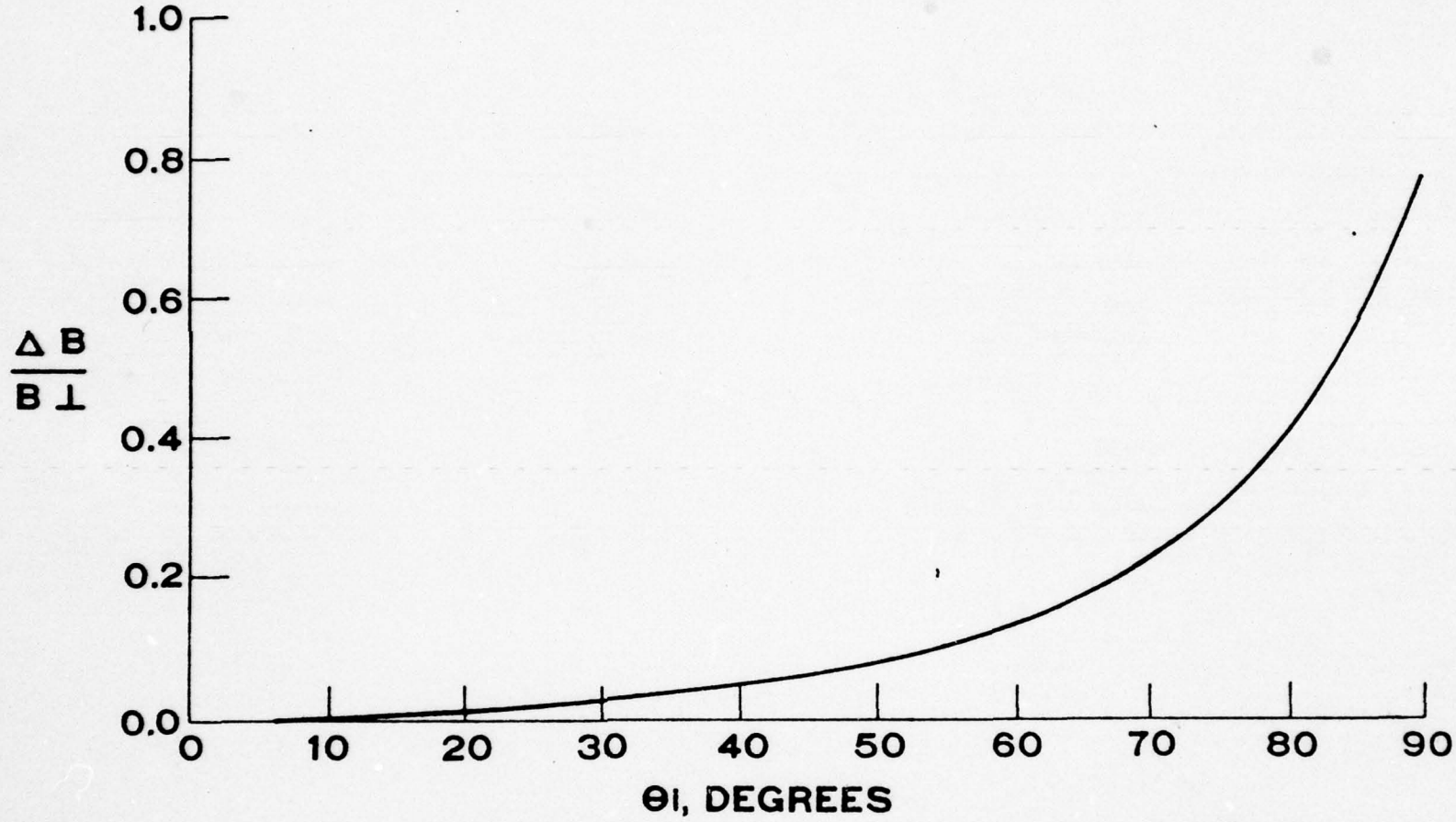

Figure 3-2. Differential Polarization vs. Incident Angle.

In a practical situation, the average differential polarization obtained by integration over typical wave spectra must be considered. Calculations were made using sinusoidal and finite amplitude trochoidal and Stokes waves of varying crest height to wavelength ratio. The mathematical formulation of the trochoidal and Stokes waves was taken from Kinsman[10].

The listing of the above described computer program which was developed as part of the subject contractual effort is exhibited as Appendix B of this report and is given the name SWPUN (Surface Wave Polarization Unbalance). Also exhibited in Appendix B are typical computer printouts showing the results of calculations.

The calculational procedure for the sine wave case is shown below by way of example. The more complex trochoidal and Stokes wave calculations can be derived from the listing in Appendix B.

$$y = A \sin 2\pi \frac{X}{L}$$

At any point on the wave $\tan \Theta_i = dy/dx$ or

$$\Theta_i = \arctan \left(2\pi \frac{A}{L} \cos 2\pi \frac{X}{L} \right).$$

Using in addition, Snell's Law relation $\sin \Theta_i = n \sin \Theta_t$ the value of $\Delta B/B_\perp$ may be computed for any value of A/L over the entire sine wave. An effective $\Delta B/B_\perp$ averaged over the sine wave is thus calculated where

$$\left(\frac{\Delta B}{B} \right)_{\text{effective}} = \frac{1}{100} \sum_{j=1}^{100} \left(\frac{\Delta B}{B} \right)_j$$

for $0 \leq \frac{X}{L} \leq 1$ with $\Delta \left(\frac{X}{L}\right) = 0.01$

Figure 3-3 shows the results of the calculations displayed as a plot of the effective differential polarization transmission $\left(\Delta B/B_\perp \right)_{\text{eff.}}$ as a function of H/L, the peak to trough wave height to length ratio, for sinusoidal, trochoidal

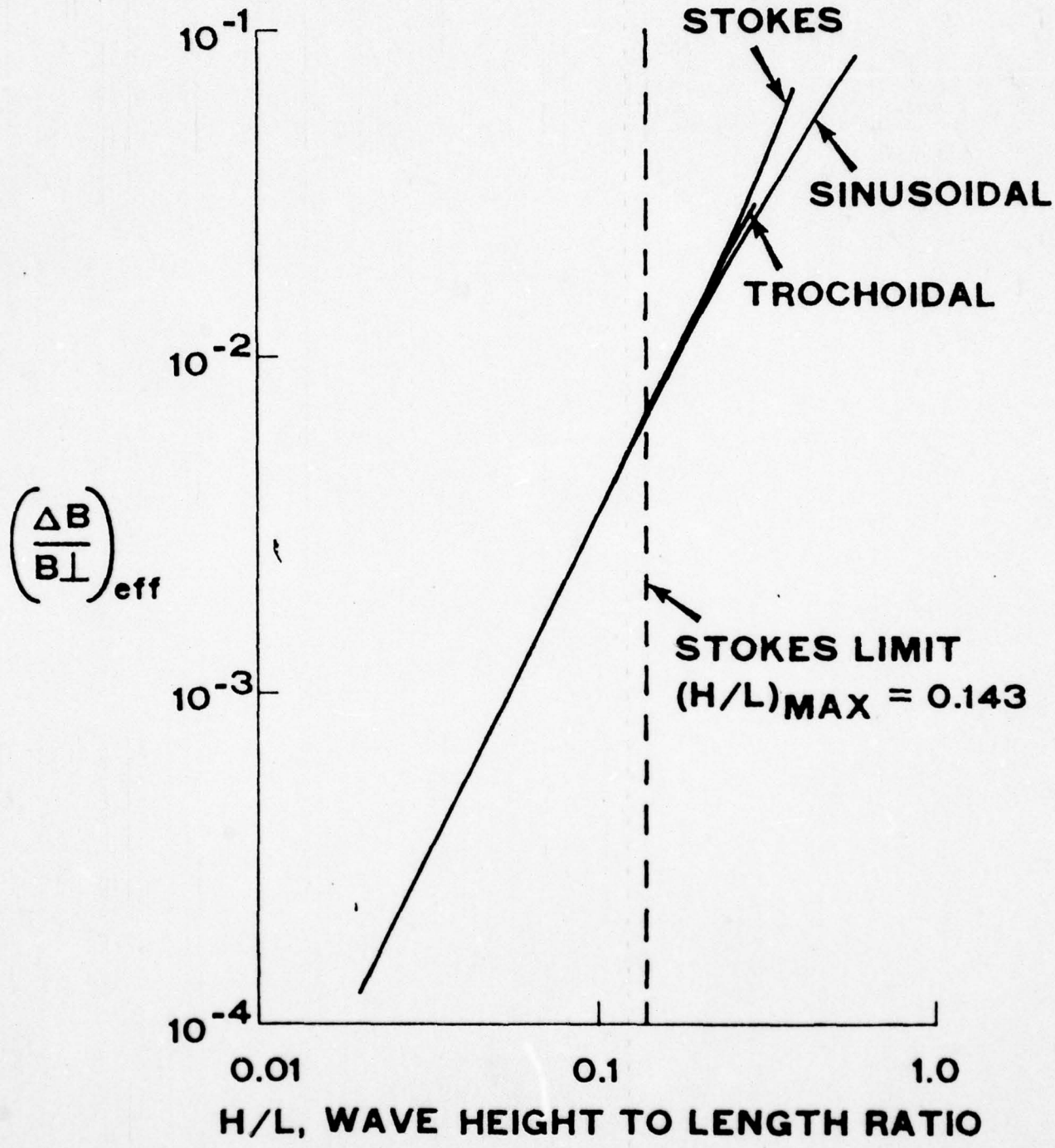

Figure 3-3. Differential Transmission of Orthogonal Linear Polarizations Averaged Over Various Wave Spectra.

and Stokes waves. The results show that for values of H/L less than the Stokes limit H/L of 0.143 the differential polarization is less than 10^{-2}. This means that the effect at worst will produce an error bias in the Raman temperature measurement of about $1^{o}C$ or 4 to 8 parts per thousand of salinity concentration. The calculation also shows that the assumption of wave shape, i.e. sinusoidal, trochoidal or Stokes, is not a significant factor in the integral of $\Delta B/B_{\perp}$ over the entire wave until the Stokes limit is greatly exceeded.

If the waves are small compared to the laser spot size on the water surface, or if the measurement is made by time average of many laser shots randomly distributed on large waves, the above calculations are valid. For single pulse measurements with waves large compared to the laser spot size, the local slope of the wave should be monitored and a correction made to the data. We have made calculations that show this to be possible.

3.1.1.2 Depth Resolution. The depth resolution depends on the laser pulse duration, the receiver bandwidth and the properties of the water transmission medium, especially the refractive properties of the surface, i.e. the air-water interface. Off-the-shelf laser and receiver systems have demonstrated 30 cm depth resolution in bathymetric lidar systems, which are generically similar to a laser Raman range gated temperature/salinity lidar system. Improvements in the direction of shorter laser pulse durations and improved receiver bandwidths and rise times are possible to incorporate into lidar systems. The major depth limitation, at least for an airborne system, appears to be, however, the random refractive effects of the air-water interface at the sea surface.

A computer routine similar to that described in Section 3.1.1.1 was written to describe the depth resolution as a function of sea state. The listings of this routine are exhibited in Appendix C and is given the name SWDCO (Surface Wave Depth Correction). Also exhibited in Appendix C are typical computer printouts showing the results of computer calculations.

The physical geometrical optics basis for the calculation of depth resolution as a function of sea state is shown in Figure 3-4.

Figure 3-4 shows a vertical laser beam entering a water surface that is titled an angle Θ_i with respect to the horizontal. The laser beam is refracted into an angle with respect to the normal Θ_i and attains an actual depth that is less than the virtual depth that would have been attained in the

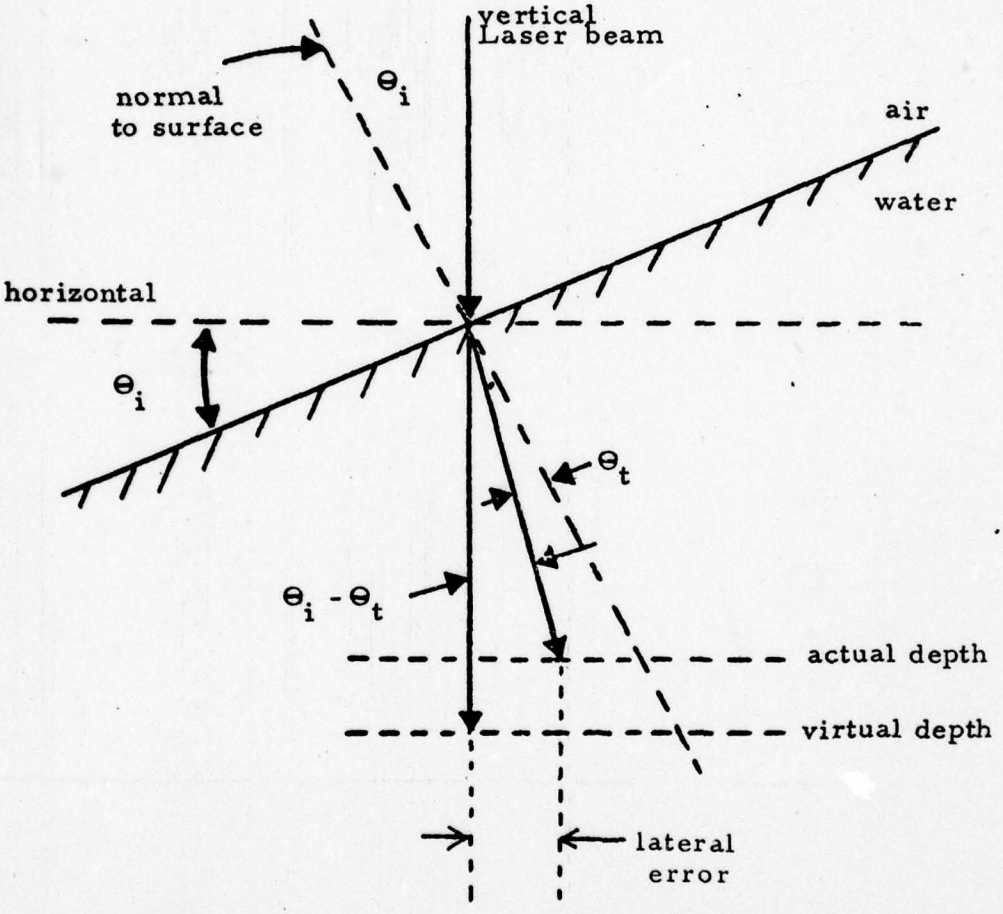

Figure 3-4. Geometrical Optics for Wave Refraction Depth Correction and Lateral Error Correction.

same transit time in the absence of refraction. The fractional difference in depth between the actual and virtual depth is given by the expression $[1 - \cos(\Theta_i - \Theta_t)]$. Computer calculations were carried out, using the code listed in Appendix C for sinusoidal, trochoidal and Stokes waves of varying crest height to wavelength ratio. The results are shown in Figures 3-5 and 3-6.

Figure 3-5 presents plots of the results of the calculations of the fractional error in depth measurement vs. H/L, the peak to trough wave height to length ratio. The calculations were made for three wave shapes; sinusoidal, trochoidal and Stokes. It is apparent from the plots that the error in depth measurement is not significantly influenced by the choice of wave model for values of H/L less than the Stokes limit of 0.143. The values plotted are the fractional error in depth measurement as averaged over a complete wave. Thus, it is seen that the fractional error in depth measurement is less than 0.3% for ocean waves having an H/L near the Stokes limits and nearer 0.1% for the more typical ocean waves with H/L from 0.06 to 0.08.

Figure 3-6 presents three plots of the results of the calculations of the fractional error in depth measurement vs. H/L for the 4th order Stokes wave which closely models real ocean waves.[10] The plot labelled "average" presents the results of averaging the fractional error in depth as calculated at 100 equally spaced positions along the wave. This is the same curve as plotted in Figure 3-5 as the Stokes curve. The curve labelled "maximum" is a plot of the maximum fractional error in depth and the curve labelled "90%" is a plot of the 90th largest value of fractional error in depth as calculated over one wavelength of a wave for each H/L. It is readily observed from these plots that even in the worst case of the laser beam encountering the maximum error condition (i.e. maximum local slope) of the wave, the fractional error in depth measurement is less than 1% for waves having an H/L near the Stokes limit of 0.143. For waves with smaller H/L, more typical of the ocean state, the maximum error in depth measurement is nearer the .1% to .2% range.

3.1.1.3 Lateral Resolution The refractive effects of the air-water interface at the sea surface will influence the lateral resolution of the measurement volume that is attainable as a function of depth. Figure 3-4 shows the lateral error produced by the surface refraction. The value of the lateral error is the product of the depth and $\sin(\Theta_i - \Theta_t)$.

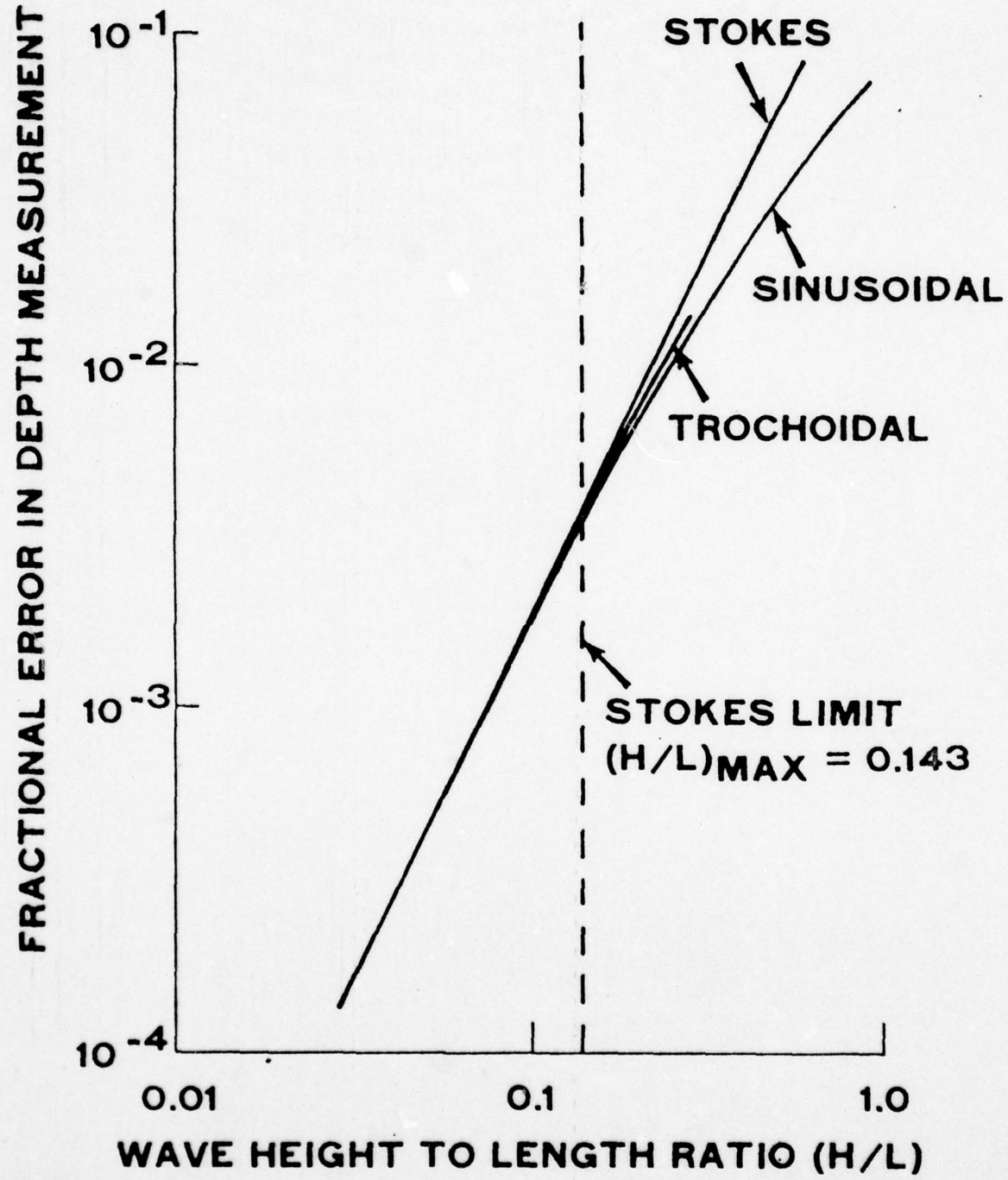

Figure 3-5. Fractional Error In Depth Measurement Due to Refraction as Function of H/L For Stokes, Trochoidal and Sinusoidal Waves.

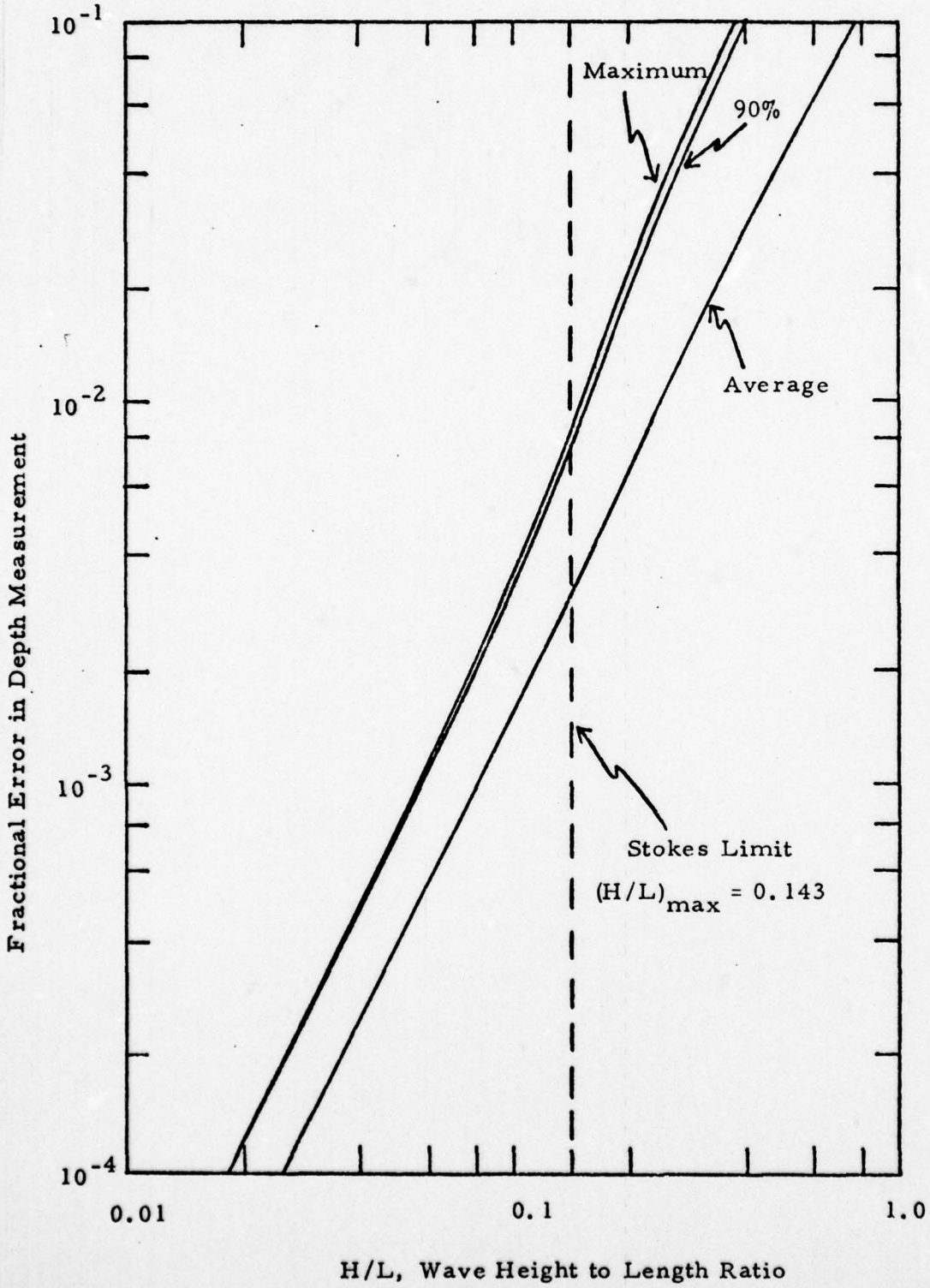

Figure 3-6. Fractional Error in Depth Measurement Due to Refraction as Function of H/L for Stokes waves showing average, 90% and maximum values.

The relative importance of this effect, when averaged over typical wave spectra, can be estimated using the same computer program that was described in 3.1.1.3 above. As listed in Appendix C, on page C-7, the 4th order Stokes wave shape, near the Stokes limit at an H/L of 0.1752 exhibits an average value of $[\,1 - \cos(\Theta_i - \Theta_t)\,]$ of 5.08×10^{-3} which is the average fractional depth error. Solving this expression for $(\Theta_i - \Theta_t)$ one obtains an average effective value for $(\Theta_i - \Theta_t)$ of 5.78 degrees. Substituting this value into $\sin(\Theta_i - \Theta_t)$ an average value of 0.101 is obtained for the fractional lateral error for near breaking waves at the Stokes limit of H/L. This means that at a depth of 100 meters the lateral position of the measurement may be in error by as much as $\pm$ 10 meters for Stokes waves near the limit of breaking. For less violent waves, having smaller values of H/L, the error becomes correspondingly less. For example, again using the data in Appendix C, on page C-8, at a value of H/L = 0.02 the average value of $1 - \cos(\Theta_i - \Theta_t)$ is 3.95×10^{-5} which gives an average value of $\sin(\Theta_i - \Theta_t)$ of 0.0089. This means that for waves with an H/L ratio of 0.02 at a depth of 100 meters the average lateral position error due to surface refractive effects would be 0.89 meters.

3.1.2 Volume Transmission Phenomena The effect of differential attenuation on the application of a "two-color" or band shape analysis of the liquid water Raman spectrum has been treated by previous investigators.[2] The new work on this contract has extended the analysis to include in addition the effects of differential depolarization and the requirements for multiwavelength polarization analysis for the Raman temperature and salinity measurement.

3.1.2.1 Differential Depolarization - Experimental The data obtained by Duntley[11] which is shown in the graph of Figure 3-7 clearly indicates that the decay of the degree of polarization of polarized beam of light as it passes through natural waters is an exponential function of the distance traversed. What is remarkable from the Duntley data is that over 80% of the original polarization remains even after traversing 20 attenuation lengths. Similar order of magnitude results for the value of the differential depolarization coefficient were obtained by other experimental investigators.[2]

In a recent private conversation with Duntley he expressed the opinions that (a) to the extent investigated, all natural waters exhibit the same general exponential deploarization characteristics, (b) very limited experimentation has been done on the depolarization of transmitted light in a variety of natural waters, (c) the fluctuations in the depolarization of transmitted light in natural

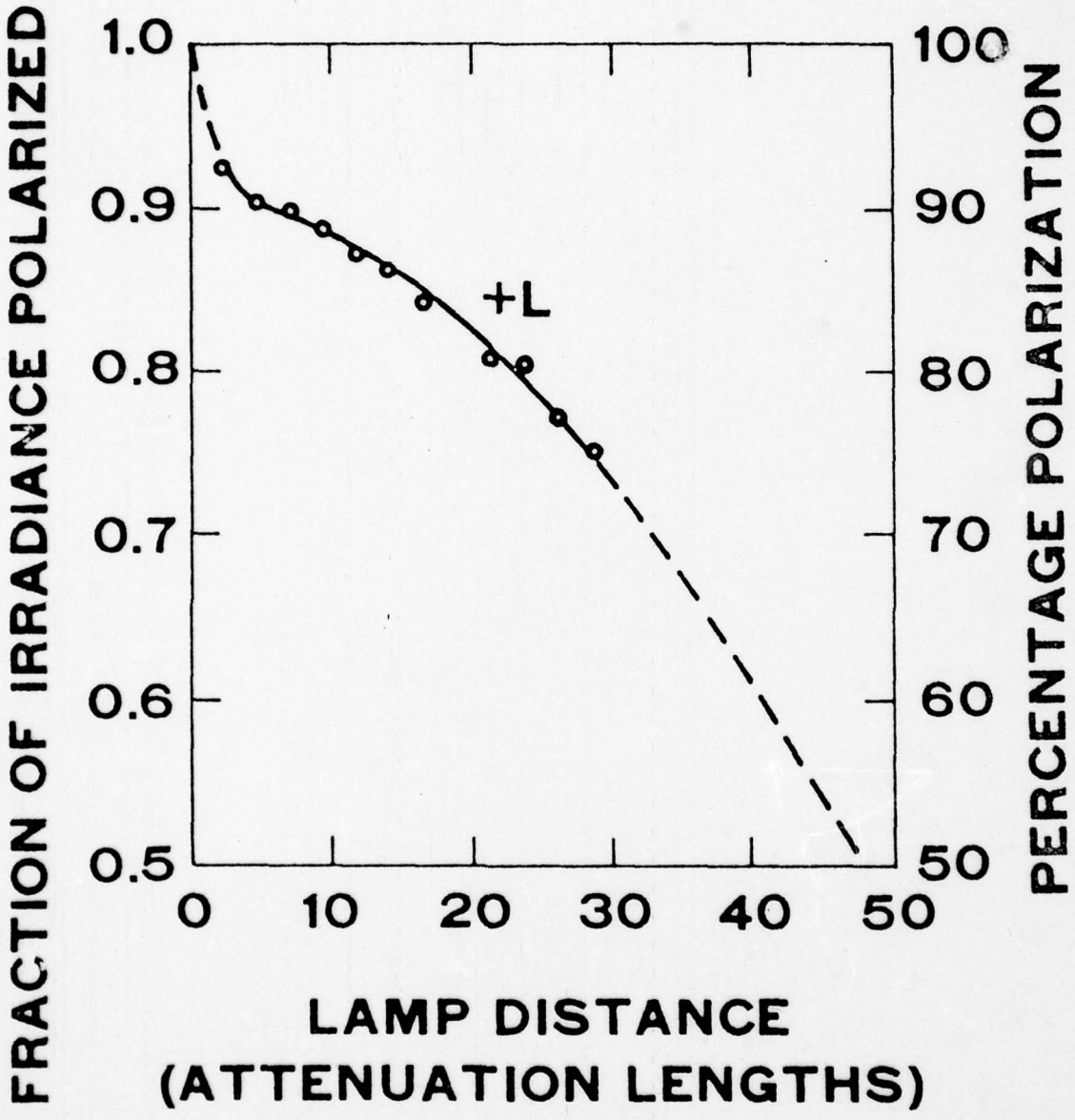

Figure 3-7. Depolarization During Transmission Through Natural Waters Obtained by S. Q. Duntley, Reference 11.

waters is virtually a virgin territory for the experimentalist and (d) the polarization information content of a beam of light is preserved essentially until the last photon has been absorbed, i. e. the attenuation coefficient is very much larger, the order of 100 times larger, than the depolarization coefficient.

The scaling of the depolarization during transmission through natural waters and its effect on a Raman depolarization ratio temperature/ salinity measurement has been estimated. The data of Duntley, shown in Figure 3-7 justify the assumption of an exponential decay law for depolarization as follows:

$$\frac{dIp}{d_x} = \rho_s \, I_p$$

where I_p is the polarized portion of a beam of light, x is the water transmission distance and ρ_s is the depolarization coefficient. The development of the formalism in terms of the observed depolarization as a function of the depolarization via two-way transmission through the water as a noise source in addition to the water Raman scattering is given in Appendix D. The result is:

$$\rho = 1 - \frac{2\left(\frac{1-\rho_R}{1+\rho_R}\right) \exp\left[-\left(\rho_s X_1\right)\right]}{1+\left(\frac{1-\rho}{1+\rho}\right) \exp\left[-\left(\rho_s X_1\right)\right] + \frac{I_{u_o}}{I_{p_o}}}$$

where ρ is the observed ratio of orthogonal polarization components, ρ_R is the Raman depolarization which is temperature sensitive, X_1 is the depth from which the scattering is being observed and I_{u_o} and I_{p_o} are the amounts of upolarized and polarized light in the initial laser beam.

The results of a sample calculation for a typical case are shown in Table 3-1 as a function of KX_1 the depth in attenuation lengths. The parameters used as input were:

$$I_{p_o} = 1$$

$$I_{u_o} = 0$$

$$\rho_R = 0.5$$

$$\exp\left[-\rho_s X_1\right] = \exp\left[-0.01\, KX_1\right]$$

$$\begin{cases} \rho_s = 0.012K & \text{(Reference 2)} \\ \rho_s = 0.008K & \text{(Reference 11)} \end{cases}$$

TABLE 3-1

SAMPLE CALCULATION RESULTS FOR DEPOLARIZATION DURING TRANSMISSION

KX_1	$\exp\left[-\rho_s X_i\right]$	ρ	ΔT (Uncorrected)	ΔT (10%) (Residual)	ΔS (Uncorrected)	ΔS (10%) (Residual)
0	1.000	0.500	0.0°C	0.0°C	0.0 ppt	0.0 ppt
1	.990	0.508	1.6	0.1	7.0	0.7
2	.980	0.515	2.9	0.3	14.5	1.4
3	.970	0.522	4.2	0.4	21.0	2.1
4	.961	0.529	5.5	0.6	27.5	2.8
5	.951	0.537	6.9	0.7	34.5	3.4
6	.942	0.544	8.1	0.8	40.5	4.0

An average value of 0.01 was taken as the proportionality constant between the diffuse attenuation coefficient K and the depolarization coefficient ρ_s, this being an average of the two known literature values of the constant.

The results in Table 3-1 show that if the ρ_s effect were neglected and not corrected for a temperature error ΔT of about $1.6^{\circ}C$ per diffuse attenuation length and a salinity error Δs of about 7 parts per thousand per diffuse attenuation length could occur. The results also show that if the proportionality between ρ_s and K is known to within 10% then after corrections are made a residual uncertainty of $0.1^{\circ}C$ in temperature and 0.7 parts per thousand in salinity would remain for each diffuse attenuation length traversed.

This analysis indicates that based upon (a) the lack of experimental work published or known on the variability of the depolarization of transmitted light in natural waters and (b) the sensitivity of the temperature and salinity measurement to the ρ_s depolarization coefficient that a major thrust of our future research should be to study the extent of the variability of the proportionality between ρ_s and K and, thus, better define the residual temperature and salinity bias that can be expected.

The impact on the experiment design and the experiment test plan is that a software capability to determine K through differential analysis of the Raman signal as a function of depth should be included. Independent experimental measurement of the proportionality constant between ρ_s and K should be investigated for a variety of natural waters.

3.1.2.2 Differential Depolarization - Theoretical. Because of the importance of the differential depolarization effect described in Section 3.1.2.1, some effort was devoted to calculations to attempt to describe from basic Mie scatter calculations the depolarization in the forward direction in natural waters. The motivation was both to "explain" the previous experimental results of relatively weak, i.e. $\rho_s \approx 0.01K$, depolarization in the forward direction and also to guide future efforts in the directions of relevant further calculations and/or experiments. The results of this effort are summarized as follows.

The depolarization of the forward-scattered component of an underwater light beam was investigated. This forward-scattered component dominated the direct attenuation beam after a few scattering lengths and is, therefore, the significant component for remote probing of sub-surface ocean temperatures. Computations, using the Mie formalism were made of the depolarization within a five-degree cone of light, single-scattered by spherical

particles which approximate in sizes and refractive indices those reported for ocean water in the literature[12]. Essentially no depolarization (<<1%) was calculated for single scattering. This result is in accord with previous observations indicating: (a) "negligible" depolarization of the forward-scattered beam of a laser after 18 scattering lengths of lake water[13]; and (b) 20% depolarization of light after travelling 20 scattering lengths of lake water[11]. Such polarization as occurs in natural waters may be the result of scattering from very small particles, non-spherical particles and/or very many scattering events. In either case direct measurements of depolarization in various types of sea-water would probably be more useful than complex and idealized calculations.

Particulates and Forward-Scattered Light in Ocean Water Brown and Gordon[12] have determined the most likely size and refractive index distributions of particulate matter in sea water at a Bahama Islands location. They find the particulate matter can be divided into three classes: (a) large organic particles with a refractive index relative to water of about 1.03 and diameters ranging upwards from 3.75 μ m with a sharply decreasing dependence of number density on particulate diameter, (b) mid-size mineral particles with a relative refractive index of 1.15 and a size distribution sharply decreasing from 1.25 to 3.75 μ m, and (c) small organic particles with relative refractive index of about 1.01 and a size distribution from 0.65 to 1.25 μ m.

Measurements and calculations by these authors indicate that the forward-scattered beam was about 5° wide (half width) with a bright 1° core. The 1° core was determined by the large organic particles while the beam beyond 2° was determined by the mid-size organics. The small organic particles contributed appreciably less than 1% to the forward scattered energy.

The calculations for this work were made for particles with a diameter D_1 of 3.95 μ m and a refractive index m_1 of 1.05 and for particles with a diameter D_2 of 1.32 μ m and a refractive index m_2 of 1.15. These diameters were selected as being representative since the scattering for the large organics and mid-size mineral particles is dominated by the smaller particles in each group because of the sharply decreasing size distributions. Thus the calculation should give an adequate "feeling" of sea-water depolarization for the exploratory purposes of this note.

Theory - Large Particle Scattering A theory has been described by Goody[14] for the scattering of light by large particles with (relative) refractive index

near unity. The theory should be applicable to the large organic particles discussed above. No depolarization effects are observed in this limit. However, since the mid-size particulate matter also contributes to forward-scatter and estimates of small effects are desired, more detailed Mie theory calculations were made as will be discussed in the following.

Mie Theory Computations The theory of scattering of light by spherical particles of arbitrary size and refractive index was developed by Mie and has been discussed by several authors[14]. We define the "plane of observation" as the plane containing the direction of propagation of the incident wave and the direction of observation. We consider the intensity of light, $J_{\perp}(\Theta)$ of plane polarized light whose incident electric vector is perpendicular to the plane of observation and which is scattered an angle (Θ) and plane-polarized light, $J_{\parallel}(\Theta)$ with incident electric vector parallel to the plane of observation. Mie theory gives:

$$J_{\perp} \propto \left| \sum_{n=1}^{\infty} \left[A_n \frac{P_n^1(\cos\Theta)}{\sin\Theta} + B_n \frac{d}{d\Theta} P_n^1(\cos\Theta) \right] \right|^2$$

$$J_{\parallel} \propto \left| \sum_{n=1}^{\infty} \left[A_n \frac{d}{d\Theta} P_n^1(\cos\Theta) + B_n \frac{P_n^1(\cos\Theta)}{\sin\Theta} \right] \right|^2$$

where the A_n's and B_n's are complex functions of products of Bessel functions and their derivatives whose arguments depend upon particle properties, and the $P_n^1(\cos\Theta)$ are associated Legendre functions. Both the sets of A_n's and B_n's and the Legendre functions have been tabulated but by different groups[15][16]. Some must be used in computations using various tables because of different sign conventions for the various quantities.

For circularly-polarized incident light the plane of observation can always be chosen so that $J_{\perp}$ and $J_{\parallel}$ can be considered as the intensities along the axes of the elliptically polarized scattered light. The axis of the ellipse will rotate with the azimuth of the observation angle.

Calculations of $J_{\perp}$ and $J_{\parallel}$ were made for $\Theta = 1^{\circ}$, 3° and 5° for the two particle types ($D = 3.95\ \mu m$, $m_1 = 1.05$, $D_2 = 1.32\ \mu m$, $m_2 = 1.15$) discussed above. No depolarization was obtained to four significant figures

except for the smaller particle size and $\Theta = 5^{o}$ for which a 0.25% depolarization was obtained. (Since random depolarization would be expected to increase something like the square root of the number of scattering events, 10^4 scattering events would be required for a 25% depolarization.)

Elaborate multiple scattering calculations would be required to carry things much further. Also we have neglected the scattering by the smaller organic particles ($D < 1.25\ \mu m$) which have less than a 1% effect for single scatter.

In summary the experimental observations of weak depolarization in the forward beam are to be expected from the character of the Mie single scatter process for the "large" particles which dominate sea-water scatter. Direct experimental measurement of depolarization in various types of sea-water would probably be more useful than further complex and idealized calculations. We intend to carry out such experiments.

3.1.2.3 Differential Attenuation and the Need for Multiwavelength Polarization Detection. The effect of the well known[4] differential attenuation of light through natural waters and its impact on the Raman depolarization detection technique was also investigated as part of the effort of planning an experimental apparatus design. The main conclusion arrived at was that a simultaneous, multiwavelength detection or wavelength scanning detection capability is required if a reasonable depth capability is to be obtained even using the polarization ratio technique. (Previous studies[2] had suggested that although differential attenuation was a problem for "two color" measurements it would not affect a polarization ratio scheme.)

The physical basis for this conclusion is that the Raman depolarization coefficient for liquid water varies across the band, ranging for circular polarization from values of 0.2 to 0.8. If the entire Raman band is detected with a single detector an average ρ_R will result.

The average ρ_R is effectively,

$$\bar{\rho}_R = \frac{\int I(\lambda)\ \rho_R(\lambda)\ d\lambda}{\int I(\lambda)\ d\lambda}$$

where the $\rho_R(\lambda)$ is weighted by the intensity $I(\lambda)$.

Differential attenuation, as for example would be caused by traversing several attenuation lengths of water, would cause a distortion of the Raman band shape i.e. the $I(\lambda)$ factor, and thus introduce an error in the effective $\bar{\rho}_R$ measured. A solution is to use multiple band segments of a bandwidth such that the percentage distortion is acceptable in each band segment. The polarization ratios are thus obtained on a band segment by band segment basis and then combined with suitable weighting functions to yield the temperature and salinity information.

The question addressed in the present new work was the relationship between the bandwidth of the individual Raman band segments, the accuracy required and the differential attenuation. The practical result was that a required spectrometer resolving power could be specified for the experimental apparatus design.

Calculations were carried out using the diffuse attenuation data of Jerlov[4] for natural ocean water which can be fit by a parabolic function such as $K = \beta(\lambda_1 - \lambda_o)^2 + \gamma$ where β and γ are constants which are functions of water quality and type. Using a typical value of β of 4×10^{-6} m^{-1} nm^{-2} results were obtained showing the residual error remaining as the Raman band was piecewise detected by means of multiwavelength analysis.

Based on this analysis, the fractional change in signal between two wavelengths λ_1 and λ_2 caused by differential transmission compared to a uniformly transparent medium is given by the following equations.

$$\frac{I_{ACTUAL}}{I_{UNIFORM}} = 1 - \frac{\exp\left\{-2d\left[\beta(\lambda_2 - \lambda_o)^2 + \gamma\right]\right.}{\exp\left\{-2d\left[\beta(\lambda_1 - \lambda_o)^2 + \gamma\right]\right.}$$

$$\frac{I_{ACTUAL}}{I_{UNIFORM}} = 1 - \exp\left\{-2d\beta\left[(\lambda_2 - \lambda_o)^2 - (\lambda_1 - \lambda_o)^2\right]\right.$$

The plots in Figures 3-8 and 3-9, based on the above equations show the signal error introduced as a function of the bandwidth with depth as a parameter. Figure 3-8 is for $\lambda_1 - \lambda_o = 0$, meaning symmetric alignment of the Raman band with the minimum of the diffuse attenuation curve and Figure 3-9 is for $\lambda_1 - \lambda_o = 10$ nm, i.e. 10 nm displacement of the Raman band from the minimum of the K curves.

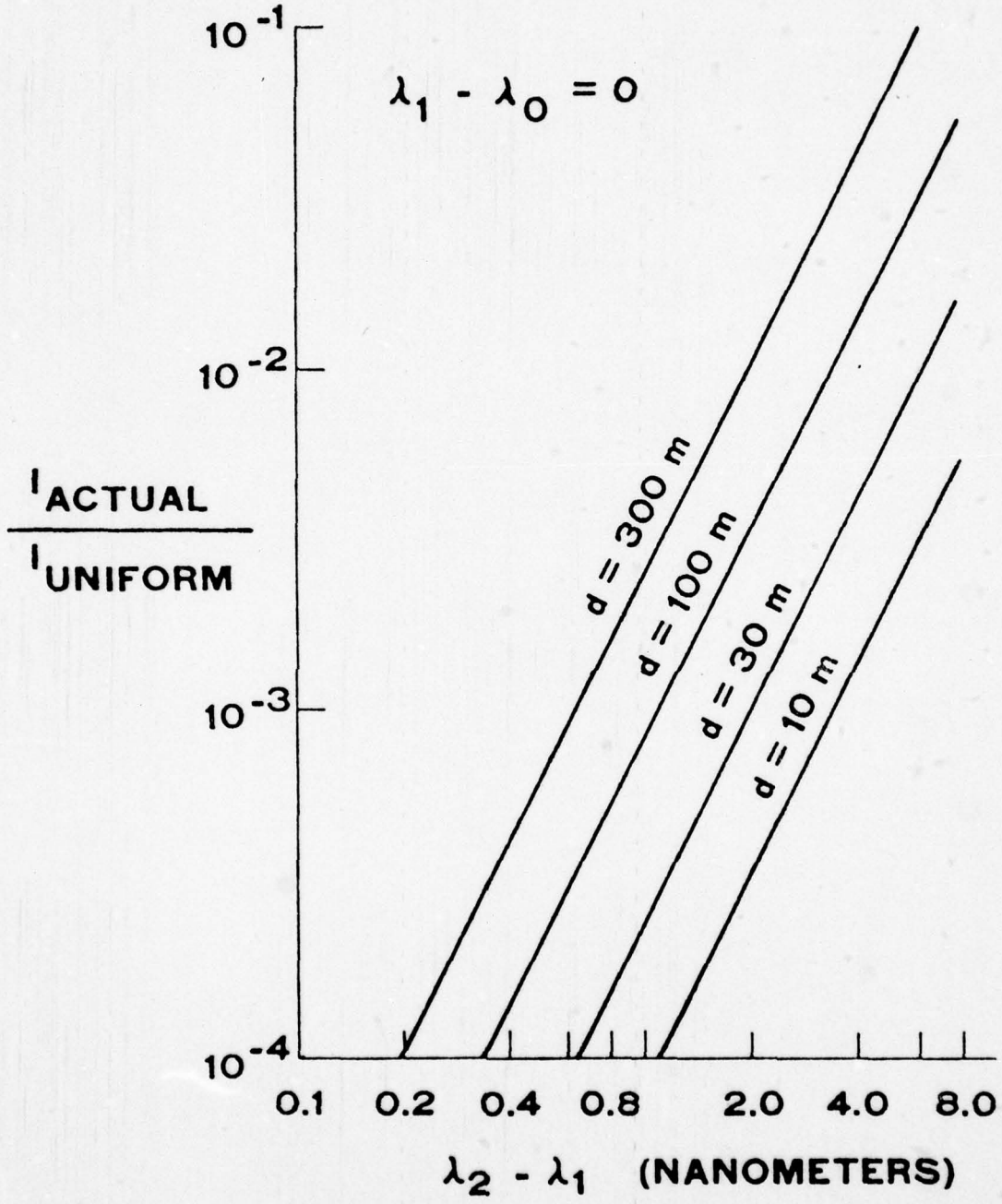

Figure 3-8. Differential Attenuation vs. Wavelength Separation With Depth as a Parameter (K minimum).

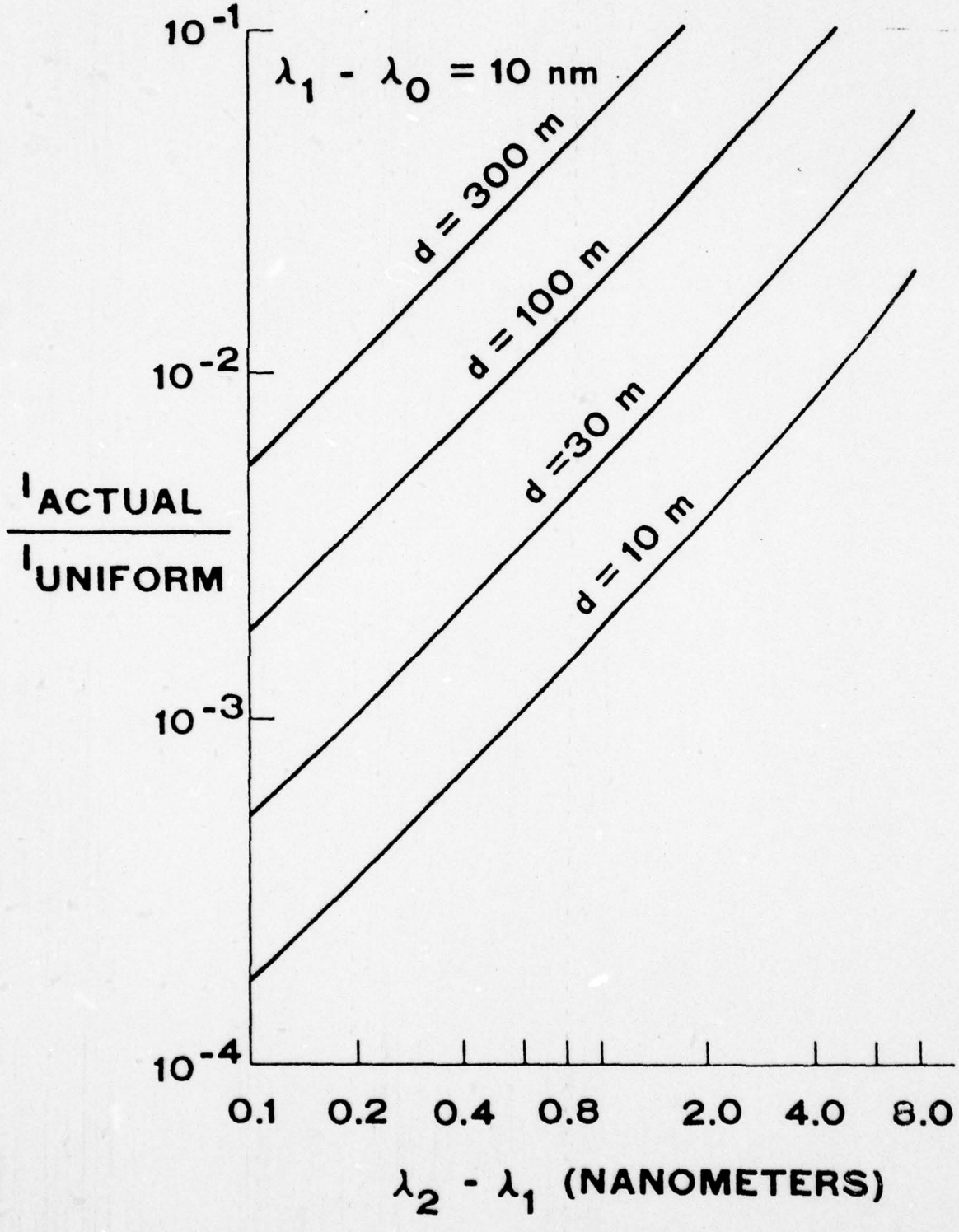

Figure 3-9. Differential Attenuation vs. Wavelength Separation With Depth as a Parameter (100 Å From K minimum).

Based on these calculations it is clear that an experimental wavelength scanning capability with a wavelength resolution the order of a few tenths of nanometers is necessary. It is also obvious from these calculations that there is a requirement for a tunable laser to position the Raman water band at or near the minimum of the diffuse attenuation (K) vs. wavelength curve. Both of these considerations were factored into the experimental apparatus design plan.

3.1.3 Non-Raman Photon Sources. Laser induced fluorescence backgrounds as well as ambient light backgrounds are common sources of interference in remote Raman measurement systems. Such effects can be reduced by using the following standard techniques.

The detection system should be limited to only those wavelengths that are within the Raman band and synchronous time gating techniques should be employed. The use of background subtraction by sampling the ambient background during the laser interpulse period should also be included in the experiment. In addition, subtraction of laser induced fluorescence can be accomplished by measurement of the laser induced spectral background level at wavelengths adjacent to the Raman water band. This capability should also be provided in the experiment apparatus design.

The following discusses the salient features of ambient light and laser induced fluorescence-like phenomena when viewed as non-Raman photon noise sources.

3.1.3.1 Ambient Light Background. Standard references[17] on remote laser Raman applications show that the limting signal to noise ratio that can be achieved in a remote Raman system is the "shot noise" in the laser Raman signal itself. Such a Raman system is assumed in the planned experiments.

The contribution of ambient background illumination to the signal to noise ratio can be shown[18] to increase the time required to make a Raman measurement with a fixed signal to noise ratio as follows:

$$T \quad \left(\frac{S}{N}\right)^2 \frac{1}{P_{AVG}} \left[1 + \frac{2P_{NEP}}{P_{PK}}\right]$$

where T isthe time required to make a measurement, S/N is the signal to noise ratio, P_{AVG} is the average laser power, P_{PK} is the peak laser power and P_{NEP} is the noise equivalent power of the ambient background illumination.

Thus the important parameter is the ratio of the background illumination or the "noise-equivalent-power" to the laser peak power.

The upward irradiance near the sea surface is given by Jerlov[4] as being 7 $mW/cm^2 - \mu m$ at a wavelength of 500 nanometers. Using this number for irradiance and neglecting the effects of sun glints and specular reflection a P_{NEP} to P_{PK} ratio of slightly greater than unity was computed for an airborne platform operating at an altitude of 300 meters and using the Raman system parameters assumed in the calculation of Appendix A.

In a boat borne experiment, because the Raman signal level using the same laser source will be considerably higher, the P_{NEP}/P_{PK} ratio is expected to be small compared to unity. However, because better than 1% measurements are desired a capability should be designed into the experiment to sample the background ambient light level in the time interval between laser pulses. This background measurement should independently sample each of the two polarization channels so that background subtraction may be applied independently to each polarization signal before a polarization ratio is computed. This is important because ambient light from sea water is known to be partially polarized.

3.1.3.2 Laser Induced Fluorescence. The presence of laser induced fluorescence-like background noise has been shown[18] to add another term to the equation which expresses the time required to make a Raman measurement with a fixed signal to noise ratio as follows:

$$T = \left(\frac{S}{N}\right)^2 \left[\frac{1}{P_{AVG}} \quad 2F + 1 + \frac{2P_{NEP}}{P_{PK}}\right]$$

where the additional term F is defined as the laser induced background fluorescence level to Raman signal ratio.

New experiments in natural waters should be designed to directly measure the laser induced fluorescence to Raman ratio F so that estimates of measurement times with constant signal to noise ratio can be made as a function of laser excitation wavelength. This capability is recommended as part of the experiment apparatus design.

It should be noted that preliminary field experiments that were conducted in natural coastal waters by CGC personnel and which are described in Section 3.2.3 of this report showed a fluorescence to Raman ratio the order of 0.03 or less when using a 337 nanometer laser source. Such data should be extended to cover the entire visible spectrum by using a tunable laser source. Such spectral coverage should be obtained from a variety of coastal water types.

3.2 Detailed Experimental Apparatus Design

This section describes the detailed experimental apparatus design that has been developed as a means of carrying out experimental feasibility studies on the use of laser Raman spectroscopy for the remote measurement of subsurface temperature and salinity. Section 3.2.1 describes a laser Raman spectrometer that would be appropriate for conducting the studies; Section 3.2.2 describes the CGC research vessel and the equipment that is currently available; and Section 3.2.3 describes preliminary experimental data that has been obtained from natural waters using the CGC research vessel.

3.2.1 Laser Raman Spectrometer for Field Utilization

The functional block diagram of Figure 3-10 illustrates an experimental laser Raman measurement system that will enable experiments to be conducted so that the important questions concerning interferences and noise sources can be answered.

The Government owned laser that is currently available at CGC for use on this program is a pulsed nitrogen laser capable of producing 100 kilowatt peak power pulses of 10 nanoseconds duration at a pulse repetition rate of 500 pulses per second. The wavelength of the laser is 337 nanometers.

The output from the nitrogen laser is used to pump a dye laser which can be tuned over the entire range of interest in the blue-green visible spectrum, i.e. 450 to 500 nanometers. The output from the dye laser is conditioned by sequential passage through an interference filter to block stray light at the Raman frequencies and through a linear polarizer and a quarter wave plate to produce a pure circularly polarized laser beam. This beam is directed at the water volume to be measured.

The Raman backscattered light is collected by a dual polarization receiver in which right and left circularly polarized light is separately collected and wavelength analyzed. A dual 1-meter spectrometer modified to operate in a parallel mode rather than in a series mode is shown as the wavelength analyzer. This would provide the few tenths of a nanometer resolution that the differential attenuation and polarization ratio detection study showed was necessary and which was described in Section 3.1.2.3.

As shown in the block diagram the dual output from the spectrometer is detected by a pair of photomultipliers, PM_1 and PM_2 in Figure 3-10, the output of which is sent to a pair of coincidence circuits. The other input to the coincidence circuits is a gate, suitably delayed relative to the laser firing, which determines the depth from which the Raman scattering is being detected. This photon counting mode of operation in which either a "0" or a "1" is detected

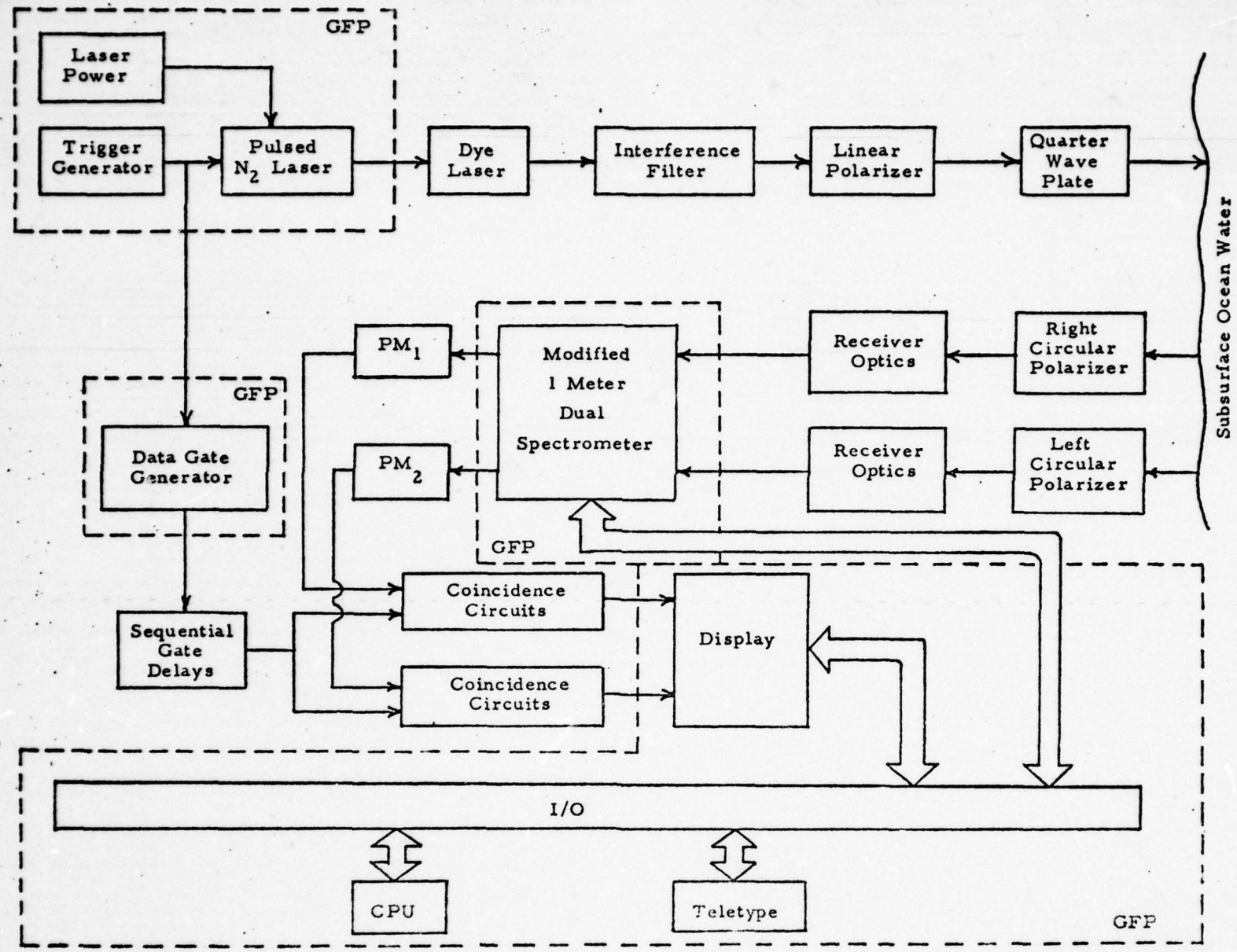

Figure 3-10 Functional Block Diagram of Dual Polarization Raman Spectrometer

for each laser pulse has been shown to be highly accurate and linear method of conducting exploratory laser Raman experiments.

The question of maintaining the "balance" of two photomultipliers is always important. In a "0" or "1" mode of operation the constancy of the photoefficiency of the photocathode surface is the important factor, not the gain of the dynode chain. In addition the two polarization channels can be optically alternated relative to the two photomultipliers to enable cross calibrations on a regular basis.

The direct output from the dual polarization coincidence circuits is displayed to enable maximum experimentalist/operator interaction in real time. A minicomputer processor (CPU) is used to provide both real time control functions as well as data acquisition and recording. The block diagram of Figure 3-10 illustrates the experimental configuration showing the computer with the spectrometer control function and the coincidence circuit data flow passing through the processor input/output interface (I/O).

The computer oriented hardware configuration shown in the block diagram of Figure 3-10 will accommodate several software approaches to maximize the information content of the data that is acquired. Examples of two such operational procedures are:

a) By sweeping many times through the spectrum of interest with relatively short data taking periods at each wavelength, the errors introduced by drift of various system parameters may be minimized. Such a scanning procedure is readily permitted by the computer controlled spectrometer.

b) Scan the spectrum of interest in a manner which yields a constant signal-to-noise ratio for the data. This is accomplished by scanning the spectrum at a rate proportional to the strength of the signal being detected.

3.2.2 Research Vessel Facility*

A basic premise of this program is to substantially advance the techniques of water Raman spectroscopy in situ. As such, all experiments / tasks (paragraph 3.3.1) are to be implemented as a function of variations in natural water qualities. The options include; further laboratory tank tests or operating from a pier or boat.

It is difficult if not impossible, to adequately simulate natural coastal water properties and gradients in tanks. Important optical properties of the water, i.e. depolarization properties, fluorescence characteristics and

*The work described in Section 3.2.2 was supported in part by NASA Wallops Flight Center.

its turbidity depend to a large extent upon living biological organisms, many of which cannot sustain life in tanks. It is important that the activities have access to fresh water intrusion, natural sediment loading and "acquatic" life and temperature gradients to directly address coastal applications.

A survey of pier and bridge locations from nautical charts as well as practical considerations such as the availability of power and coordinating traffic patterns rapidly leads to the conclusion that a completely self contained floating platform is the more cost effective way to access the necessary operational environments.

The requirements and characteristics of a small, economical and easy to operate oceanographic research vessel have been exhaustively investigated with internal support. These files are available in our Wakefield office.

A 35' twin screw, nine ton displacement research vessel, Makai, Figure 3-11 has been fitted out and currently hosts the operational apparatus* configuration shown as Figure 3-12 which was used to obtain the first in situ data discussed under Section 3.2.3.

The current laser Raman system is a bistatic configuration. The laser source is a pulsed nitrogen laser operating at a wavelength of 337.1 nanometers and producing pulses of 100 kilowatts peak power with an effective pulse duration of 10 nanoseconds at a pulse repetition rate of 500 Hertz.

As shown in the block diagram, a bistatic arrangement of the transmitter and receiver optics function to define a volume of subsurface water from which the laser Raman scattering is detected. Operation in such a bistatic mode is adequate for experimental studies in the first few tens of meters of depth. Practical application of the technique should utilize electronic range gating techniques, especially for deeper penetration applications. The photograph of Figure 3-13 shows the equipment in the laboratory undergoing calibration prior to installation aboard the Makai.

The photons collected by the receiver optics are passed through a double 1/4 meter focal length spectrometer having a 0.5 nanometer spectral resolution. The function of the spectrometer is to produce a spectral scan of the liquid water Raman O-H stretching band with sufficient resolution so that the monomer and polymer components can be resolved and a temperature determined.

---

*Much of the Government owned equipment is accountable under NASA Contract NAS6-2751

Figure 3-11. Bistatic Laser Raman Equipment Aboard the Research Vessel Makai.

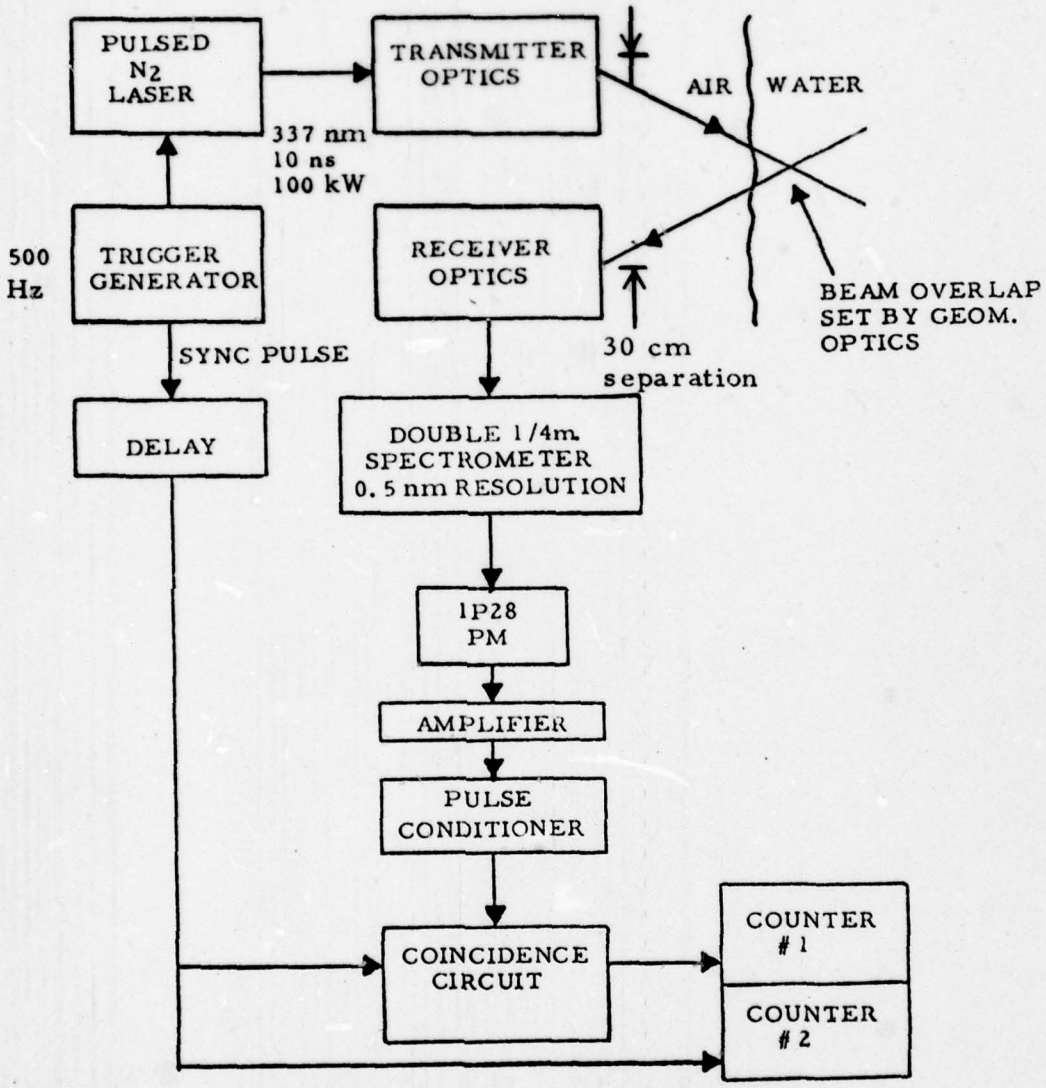

Figure 3-12 Block Diagram of Laser Raman System Currently Operational on Research Vessel Makai.

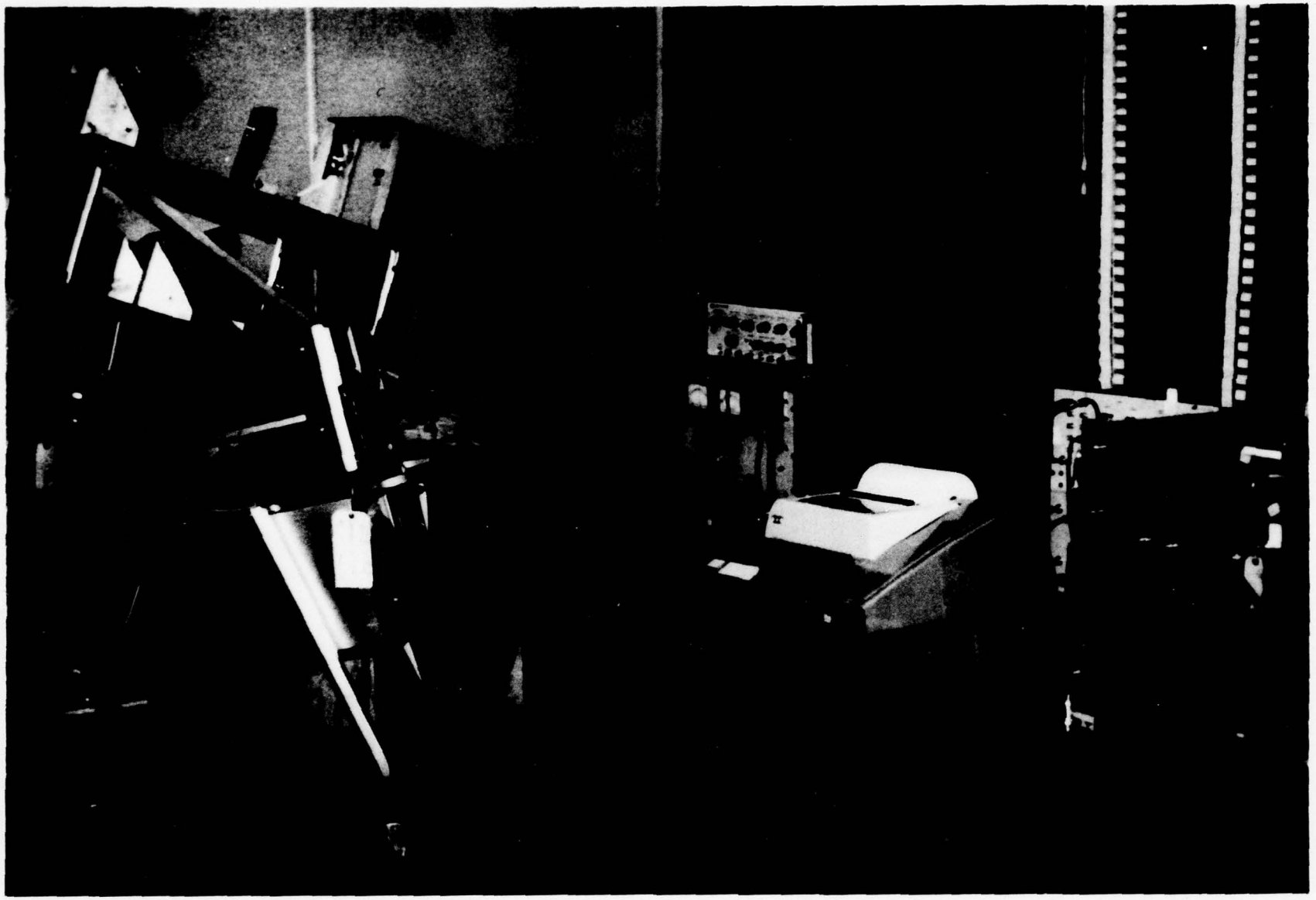

Figure 3-13. **Bistatic Laser Raman Equipment in the Laboratory.**

The Raman photon output from the spectrometer is detected by a RCA 1P28 photomultiplier, amplified by a HP 461A amplifier and conditioned by a HP pulse electronics. The conditioned Raman photon signal and a gate pulse suitably synchronized and delayed with respect to the laser firing were combined in a coincidence circuit the output from which is recorded by counter #1. The number of laser pulses occurring is recorded in counter #2. The ratio of the value recorded by counter #1 to counter #2 is the Raman signal obtained over a given time interval.

The photograph of Figure 3-14 provides a close-up view of the optical transceiver cart configuration selected for implementation. A custom constructed mobile cart houses the laser transmitter and spectrometer receiver in an over and under configuration. Rigid extensions of the shelves are used to support the transmitter/receiver optics and extend the "viewing points" 45cm beyond the transom of the vessel where high quality folding mirrors are used to complete the path.

The compact 120cm(L) x 75cm(W) x 97cm(H) cart is equipped with wheels which facilitate service access and withdrawal into the cockpit for protected storage when not in use.

The laser employed (top shelf) is a GFP Avco C950 nitrogen unit with a CGC modified cooling system in order to lighten payload. The spectrometer (bottom shelf) is a Spex model 1672 Doublemate and 1200 g/mm grating set blazed at 300 nm.

3.2.3 Preliminary Experimental Raman Data Obtained from Natural Waters**

The Raman lidar system that is shown in Figure 3-12 and is now currently on the research vessel Makai has been operated to obtain preliminary laser Raman spectra from in situ natural coastal waters. The data was analyzed to obtain a temperature measurement. It is important to note that this is the first such data known to have been taken in natural coastal waters.

The Raman spectra were obtained from the Annisquam River in Massachusetts near the berth of the research vessel. Spectra were obtained over nearly a full tidal cycle with no apparent change in the character of the data. It was very reassuring that (a) the temperature obtained agreed with prior laboratory calibration and (b) the fluorescence to Raman ratio was very low.

** The work described in Section 3.2.3 was supported in part by NASA Wallops Flight Center.

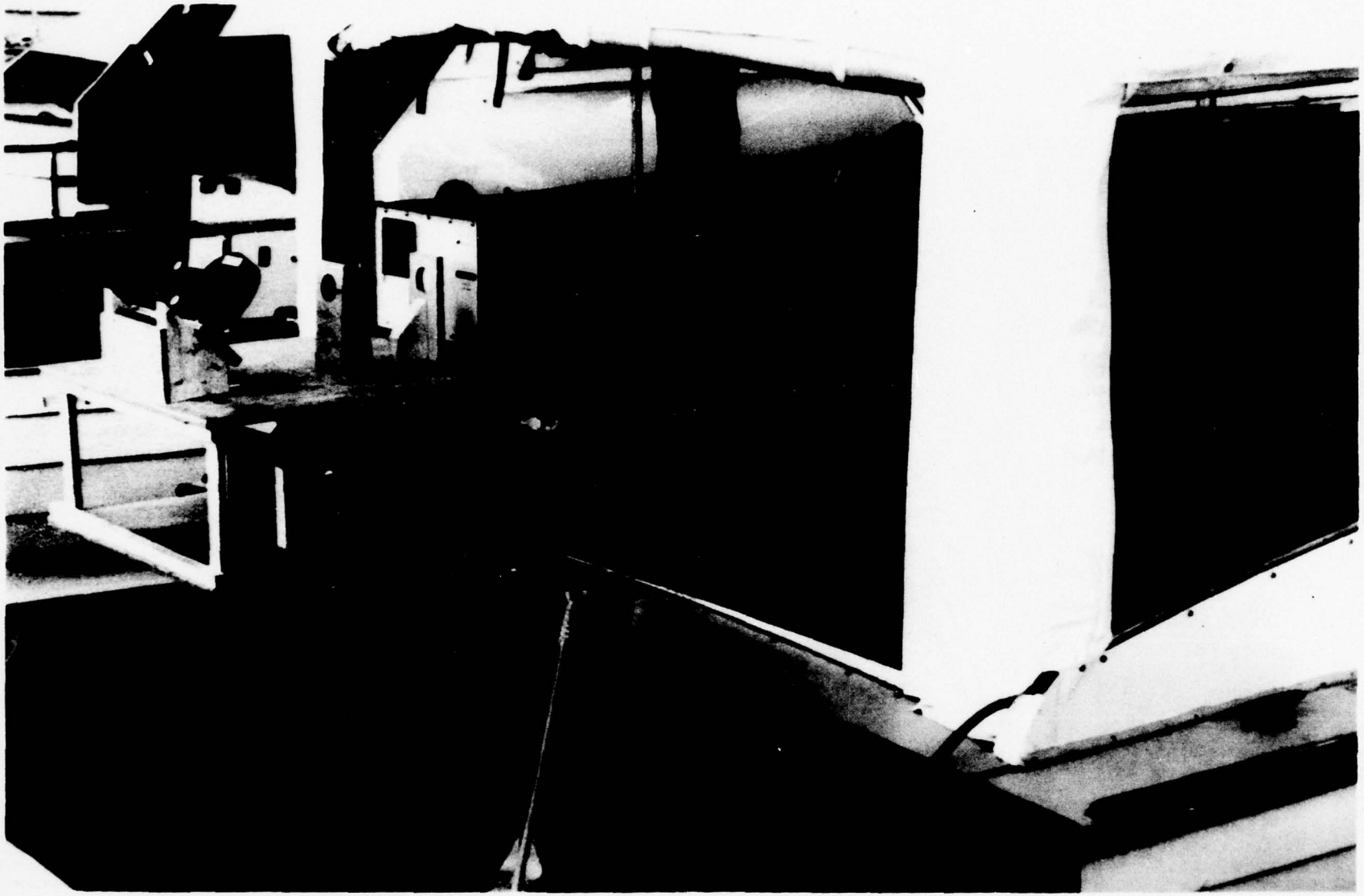

Figure 3-14. Bistatic Laser Raman Equipment Aboard the Research Vessel Makai.

Typical spectral data that were obtained in the Annisquam River are shown in Figure 3-15. This is a plot of the number of Raman photoelectrons collected per 0.5 nanometer spectral interval per 10,000 laser pulses as a function of wavelength. Shown are two sets of data, the dashed curve obtained as an instrument calibration in the laboratory with a water sample at 22°C and the solid curve obtained in the Annisquam River water at 6°C. The temperature is obtained by normalizing the peaks and observing the change in height of the band contour. A temperature scale has been calculated based on laboratory data and placed on Figure 3-15 so that 22°C corresponds to the laboratory calibration data. The Annisquam River temperature of 4°C inferred from the spectra is consistent with the measured value of 6°C to within the statistical precision of the measurement which was $\pm$ 2°C. Large improvements in accuracy will be observed by increasing the photoelectron sample size and also by using standard[19] least square computer curve fitting to enable analysis of the entire Raman band.

A short research note has been written and published in Geophysics Research Letters to describe these initial results. A preprint of the note is included as Appendix E of this report.

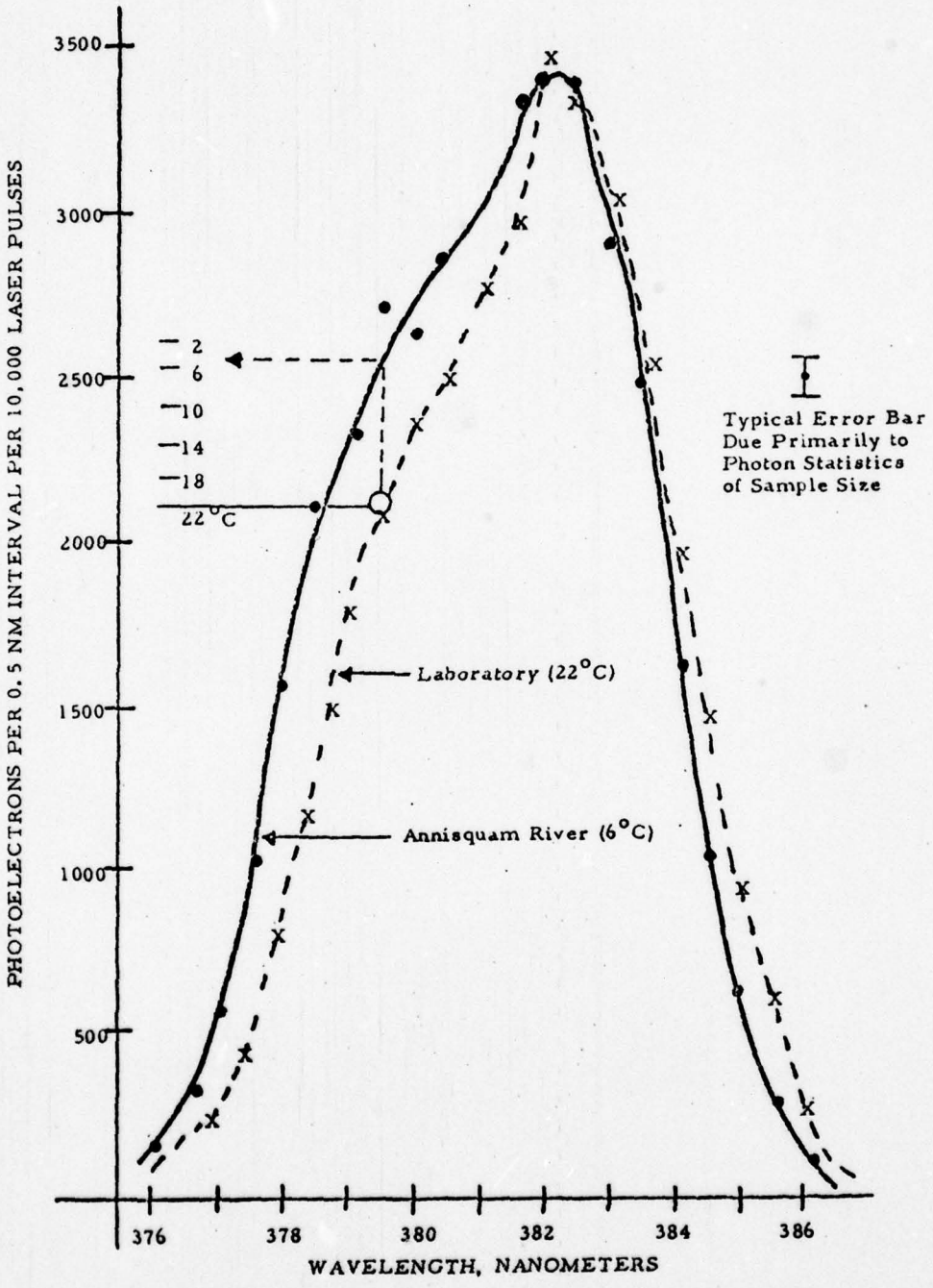

Figure 3-15 Raman Spectral Data for Liquid Water.

3.3 Experimental Field Test Plan

A series of field experiments in a variety of natural coastal water conditions are required to further study and quantitatively determine the extent of natural and equipment related interferences and noise sources (Paragraph 3.1) upon the laser Raman technique to measure subsurface temperature and salinity.

A broad plan for Raman subsurface temperature/salinity research has been considered to carry the program from its present formative stage to a more developed and predictable documented technique. The Schedule and Plan for Raman Temperature/Salinity Research Figure 3-16 illustrates a modestly supported (1- 1 1/2 man years/yr) program which accommodates 10-12 month period of primary experimentation and apparatus improvement.

During the second phase it is anticipated that the refined and developed experimental apparatus will be capable of processing large volumes of data in a real time profiling mode through substantial temperature and salinity gradients. It is desirable to validate and further develop the techniques in the presence of more accurate and sophisticated sea truth instrumentation, preferably as an adjunct to an already established field research or monitoring program. Several candidate locations capable of supporting such a coordinated effort have been considered and they are discussed under Paragraph 3.3.2. Sea Truth Requirements.

The third phase which will provide a broad data base in deep ocean as well as coastal waters might very well take the form of installing the apparatus aboard one or more of the manned vessels operated under the support of the Office of the Oceanographer for research and data base gathering purposes. One such vessel which in our view is particularly well suited to the task is the twin hulled U.S.N.S. HAYES.

Of the specific initial experimental tasks listed below in Paragraph 3.3.1 some must be implemented in series. All experiments are as a function of natural water quality (i.e. diffuse attenuation coefficient (K), fluorescence to Raman ratio (F), salinity, sediment loading, aquatic life, etc.) and depth. Laboratory experiments have been performed by Walrafen,[20] Schwiesow,[21] Chang and Young,[2] and Slusher and Derr.[1] However, it can be readily seen that it is diffucult if not impossible, to simulate natural conditions in laboratory tanks.

SCHEDULE FOR RAMAN TEMPERATURE/SALINITY RESEARCH

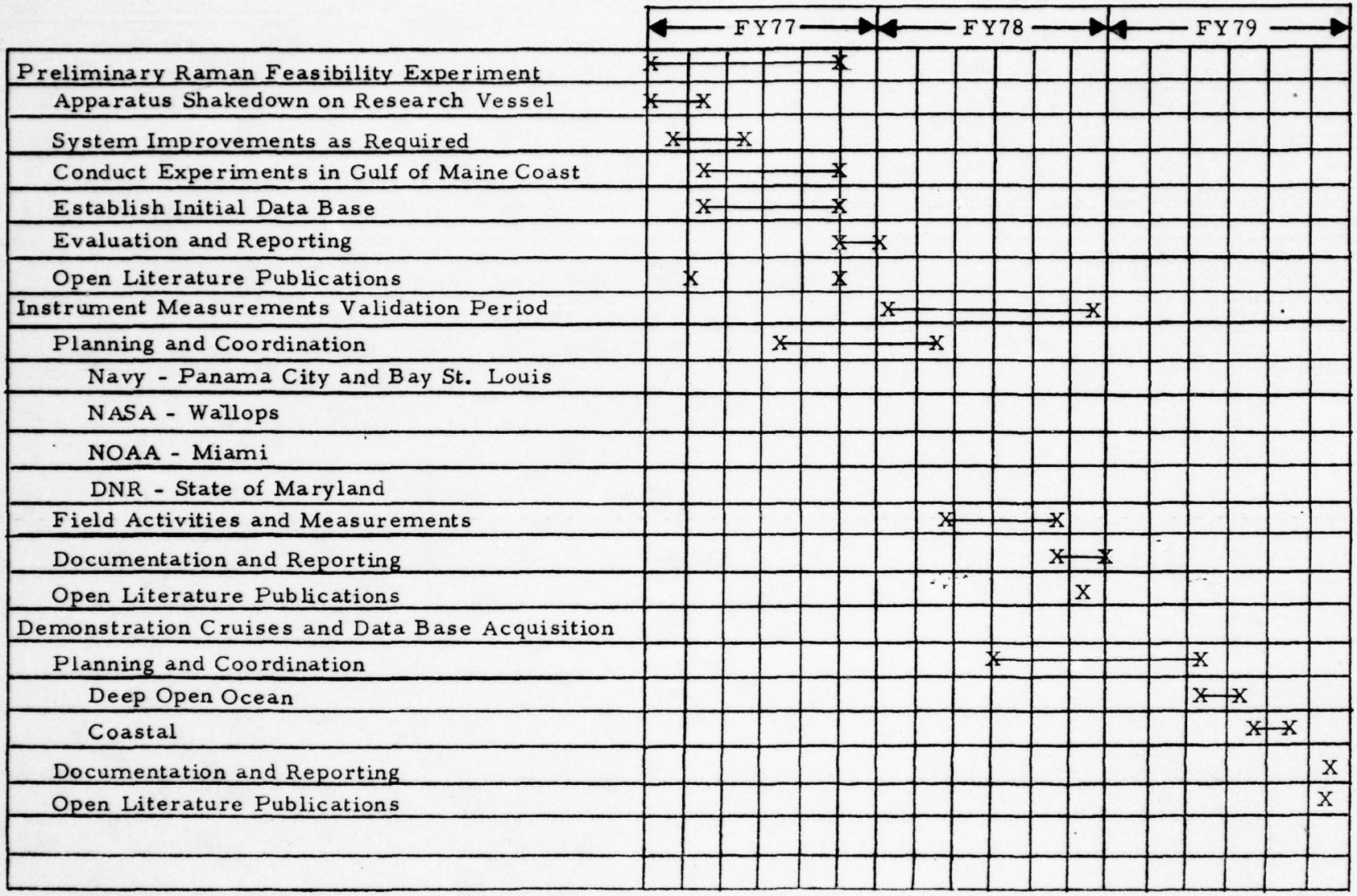

Figure 3-16 Schedule and Plan for Raman Temperature/Salinity Research.

The most cost effective means to access natural water quality conditions is to place an apparatus aboard a boat capable of relocating. The apparatus should be designed so as to be transportable by two persons by truck to boats operating out of different geographical locations. A maximum gross apparatus weight under 900 kg with power consumption under 6KW will provide for accommodation aboard average vessels 9 meters long and greater. A functional block diagram of an existing Government owned apparatus available to support this field test plan appears as Figure 3-12. The preferred configuration which can be readily assembled from additional existing Government inventory and minor purchases is shown as Figure 3-10.

The balance of this section discusses experimental objectives and methods, sea truth requirements, general test site considerations and a well researched and documented initial recommended testing region with supporting nautical charts.

3.3.1 Experimental Objectives and Method

3.3.1.1 Transmission (i.e. K) Derive and catalog a class of attenuation coefficients as a function of various natural coastal water qualities and as a function of depth. Operate a tunable dye laser through the wavelength regions 400 to 500 nanometers. Observe the Raman shifted spectral region between 420 and 580 nanometers. Perform slope analysis. Correlate with alpha meter readings. Evaluate data to specify optimal 1/4 wave plate for advanced experiments.

3.3.1.2 Fluorescence Raman Ratio (F) Survey the Raman to Fluorescence ratio as a function of various natural coastal water quality. Operate tunable dye laser as in 3.3.1.1. Exercise as a function of depth in several varying water quality locations and establish an historical data base.

3.3.1.3 Differential Polarization Analysis Operate the dye laser in selected spectral regions based upon the results of 3.3.1.1 and 3.3.1.2 above. Obtain spectrally resolved polarization ratio data. Evaluate data to verify required spectral resolution. Specify multichannel wavelength detection requirements.

3.3.1.4 Proportionality Between ρ_s and K. Analyze the data obtained in 3.3.1.3 in accordance with the scaling laws described in Appendix D and discussed in 3.1.2.1. Determine the variability in the proportionality between ρ_s and K as a function of the type of water, water quality and the absolute levels of ρ_s and K.

3.3.1.5 Temperature vs. Salinity Separability The spectrally resolved polarization ratio data obtained in 3.3.1.3 will also be analyzed to show the extent to which temperature and salinity may be independently measured.

3.3.2 Sea Truth Requirements

Reliable and accurate sea truth and meteorological data is required. The options to obtain sea truth range from totally R/V self contained instrumentation to heavy dependence upon coordinating experiments ("piggy-backing") with existing hydrographic activities. Figure 3-16 shows the desirable schedule and increasing experiment diversification plan. During the initial Gulf of Maine field effort it is felt that very modest sea truth instrumentation obtainable from Government inventory or local purchase will be adequate.

As discussed earlier in this section, the second phase will be oriented towards a greater dynamic range of performance and data base gathering, suggesting more sophisticated automatic data logging equipment. Towards this end and as part of the planning effort we have been in contact with cognizant personnel at NASA Wallops Flight Center, NOAA Remote Sensing Laboratory, Miami, and Department of Natural Resources - State of Maryland (DNR). All have expressed a strong interest in promoting the state of the art by making available space on their own vessels of opportunity at little or no cost to this program.

NOAA's east coast activities are supported by three research vessels: a 83m state-of-the-art instrumentation equipped vessel capable of open ocean ground truth measurements, a 45m instrumented vessel operating in and about the port of New York and a smaller high speed vessel.

Sea truth observing techniques include: continuous subsurface temperature devices, continuous salinity monitors, optical spectrometers, Sechi disc, expendable bathy thermographs (XBT), drifting and moored buoys, etc.

The DNR-Maryland facility under Dr. Myron Miller is responsible for the State of Maryland Power Plant siting program. A regular function of this office is to monitor/measure thermal plume discharges in three dimensions from power plants. An offer has been extended to place the apparatus aboard a DNR vessel where additional sea truth will be obtained from their highly resolved thermistor chain which is towed through the plume in grid pattern and well documented during three seasons/yr.

Additional candidate sites and coordination planning for Phase 3 is better left for a later point in this program.

3.3.2.1 Sea Truth Measurement Parameters At a minimum records for all phases should be kept to include:

a) date, time, investigator's name

b) location of experiment (latitude and longitude)

c) sea state and surface conditions (dialog and photos)

d) atmospheric temperature, humidity, wind

e) sea surface and subsurface temperatures

f) salinity (Initially surface water samples will be drawn at each location and portions of water will be sent to the laboratory for analysis. The second portion will be tagged by experiment number and preserved. Salinity gradients may be tested through the use of classical Nansen jars.)

In addition to the above the computer will automatically calculate and tabulate K, the diffuse attenuation coefficient, and the background fluorescence level in the wings of the Raman spectra.

3.3.3 Test Site Requirements

Proper selection of experimental test sites is a vital ingredient toward the development and validation of new remote measurement and refinement techniques. Selected sites must offer a wide variety of water quality conditions including a range of attenuation coefficients, representative cross section of coastal and estuary impurities (fluorescence sources), diverse micro organism type count, and a range of salinity conditions. While variations in sea floor types and bottom vegetation is considered to have a minimal effect on a gated Lidar system variation in texture, grain size, density and depth in the presence of tidal current or wave turbulance could produce significant perturbations in turbidity patterns on a time scale which is short relative to an experimental period. The natural vicissitudes of the ocean and weather conditions can be counted upon to offer wide variations in sea surface conditions.

Within reasonable distances of the R/V cruising range it is desirable to access zones of relatively deep clear, shallow clear, deep-turbid, and shallow turbid water which are expected to vary synoptically and in a reasonably predictable pattern.

3.3.3.1 Water Quality

Of the preceding site requirements water quality is the factor of initial major experimental interest.

Turbidity in sea water is due primarily to the presence of tiny particulate matter or plankton entrained in the water. The latter source can be maximized or minimized by selecting winter or summer frames of operation. Increases in turbidity are generally a result of the intrusion of suspended particulate matter into a watermass from an extraneous source (such as runoff from land following percipitation) or the resuspension of fine bottom materials as a result of the action of tidal currents or wave turbulence. In any case, these increases in particulate matter are usually rapid, with pronounced changes in turbidity being measured in hours. Decreases in turbidity, on the other hand, are usually slow to occur, often requiring days or even weeks for a water mass to return to a background level. A downward flux in turbidity in an area of water results from the settling of the entrained particulate matter or from the replacement of the watermass by clearer water. The former process is extremely slow and requires a period of relatively low turbulence. The latter process requires a source watermass and a constant current or drift from the clear watermass into the turbid watermass.

3.3.3.2 Salinity

It has been well documented that salinity concentrations in open ocean vary slowly over hundreds of square miles. In addition open ocean surface layers are usually well mixed often leading to the assumption of salinity as a constant.

Unlike ocean waters, salinity in coastal waters vary dramatically responding to the intrusion of fresh water from rivers, heavy rain runoffs, snow and ice melt runoff along the coast. In the summer during long periods of zero rainfall and above normal temperatures significant increases in salinity may be expected.

Performing experiments in spring through late fall in coastal waters, latitudes 40° and greater offer a range of salinity concentrations from ≈ 9 ppt to in excess of 30 ppt,[22] while navigable access to the head waters of a major drainage basin will offer opportunities to data sample nearly fresh waters.

Initial Test Site

Cape Ann Marina - Experimental apparatus shakedown and initial calibrations begin in the laboratory and are refined in the field establishing a feasibility data base of initial equipment performance in natural waters. The waters surrounding Cape Ann from 41° 10' to 42° 50' latitude and 71° 02' to 71°00', Figure 3-17 provides suitable water quality and sea conditions with convenient access for this early task including the clear water masses in and around Annisquam, fresh water intruding from the Merrimack River and the turbid waters of Boston Harbor. Access to Power Plant thermal plumes are available in Salem and Boston Harbors.

The oceanographic characteristics of this region are well documented and have been the subject of numerous studies supported by UNH Sea Grant - Raytheon Program, NOAA Environmental Research Laboratory and Massachusetts Department of Natural Resources. Much of the characterizations presented here were documented in the Proceedings of Conference on Toxic Dinoflagellate Blooms hosted by Massachusetts Science and Technology Foundation and Massachusetts Institute of Technology Sea Grant Program.[29]

Characteristics of Coastal Stations Located 1-3 Miles (1.6-4.8 kms) from Shore between Cape Ann, Massachusetts and Rye, New Hampshire (Mulligan and deLara, 1974)

Salinity (^{o}/oo)	9.3 - 33.3
Temperature (^{o}C)	1 - 18.1
Depth of Euphotic Zone (m)	5 - 20
Chlorophyll a (mg/m^{3})	0.3 - 15.5

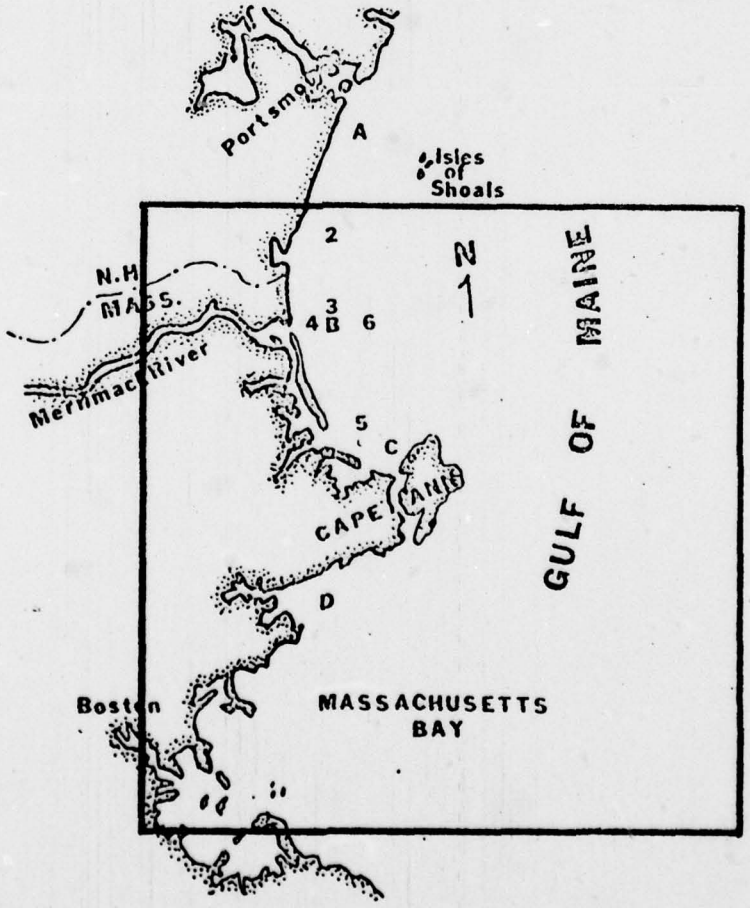

Figure 3-17. Map of Northern Massachusetts and New Hampshire Coastal Region

A. Rye, New Hampshire, B. Newburyport, Massachusetts, C. Annisquam, Massachusetts, D. Salem, Massachusetts, Stations 2-6 occupied 1973-1974.

The coastal region from Rye, New Hampshire to Cape Ann is part of the Gulf of Maine. The coastline of the region consists mostly of low, sandy barrier beaches which protect extensive spartina marshes and estuarine areas. The coastal region contains the Merrimack River, the major river between Cape Cod and Cape Elizabeth (Saco River). The Merrimack River drainage basin comprises eight percent of the entire drainage basin of the Gulf of Maine[23] and dominates the physical, chemical and biological characteristics of the surrounding coastal region.

Average annual rainfall in the region is 43 inches (1.09m)[24] which is distributed rather uniformly over the entire year. River runoff exhibits a definite season l cycle coinciding with the period of major snow melt during the spring (Table 3-2).

TABLE 3-2

Water Discharge Data of Merrimack River Below Concord River at Lowell, Mass. in CFS (cubic ft. per second)

Date	1945/46[1]	1970/71[2]
October	4266	3093
November	6047	4257
December	10041	4969
January	8856	4169
February	7148	5235
March	19200	9843
April	9739	21700
May	11869	16510
June	8536	3511
July	2695	1567
August	4181	2109
September		2074

Average discharge for 48 year period ending 1971 = 7055 CFS

1. FORD, W. L. 1947. Hydrography of the Western Atlantic. No. 3 The distribution of the Merrimack River effluent into Ipswich Bay. Woods Hole Oceanographic Institution Technical Report. 23p.

2. ANON, 1971. Water Resources Data for Massachusetts, New Hampshire, Rhode Island and Vermont. Part I. Surface Water Records. Part 2. Water Quality Records. U.S. Dept. of the Interior. Geol. Survey. 401 pp.

Winds follow the same general patterns as elsewhere in the Gulf of Maine (25)(26) mostly from the west, with considerable seasonal variation: in Fall and Winter, mainly from north to west; in Spring, winds are variable and, during the Summer, winds blow from the sourthwest and southeast quadrants.

Non-tidal currents tend to move the surface coastal waters in the region counter-clockwise, to the southwest along the coast; bottom waters move either to the southwest or toward the shore according to Bigelow[23] Day[27], and Graham[26]. Graham also noted that bottom water which originated in the northern Gulf of Maine moved during the summer through Jeffrey and Scantum Basin and toward the shore near the mouth of the Merrimack River.

Winds can generate surface currents up to 2% of wind velocity, and consequently, non-tidal currents are stronger in the fall and winter because of higher wind velocities from the northern quadrant. Currents are increased during the spring due to increased snow-melt runoff piling up along the shoreline. Winds from the southern quadrant, common in the late spring and summer, reduce and even reverse the slow-moving, counter-clockwise, surface current along the coast. The most prominent feature of the water circulation along the western coast of the Gulf of Maine is upwelling[26].

Mulligan and deLara[22] have recently reviewed the Phytoplankton and hydrographic conditions in the region (Figure 3-17).

Salinities measured from August 1971 to July 1972 ranged from 9.3 to 33.3 0/00. Highest salinities were recorded in January and February. Manohar-Mararaj and Beardsley[28] estimated that the Merrimack River contributed over 90% of the fresh water in Massachusetts Bay. Ice-flows and low salinity surface water from the Merrimack River were observed six miles offshore and could be seen moving southeastward around Cape Ann into Massachusetts Bay (Mulligan, unpublished). Consequently, the surface waters off and to the south of the Merrimack River displayed the lowest salinities. During the springtime, the entire water column off Annisquam had reduced salinites when compared with conditions present at coastal stations to the north.

Water temperatures ranged from 1-18.1°C over this period and were slightly lower in the northern portion of the region throughout the year. The coastal waters to the north of the Merrimack River (to a depth of 20 meters) were generally well mixed. Thermal stratification developed during the warmer months and became well established, especially at the mouth of the Merrimack River and in the waters to the south.

The depth of the euphotic zone varied from 5-20 meters with the lowest transparencies occurring during the spring and fall. Silt contributed by the Merrimack River was largely responsible for the minimal spring transparencies.

Tables 3-3, 3-4, and 3-5, are reprinted in their entirety as taken from U.S. Coastal Pilot #1 NOAA for the convenience of the reader in familarization of the region, climate, mean surface water temperature/ density meterological data.

Figures 3-18 through 3-24 are cuts from Nautical Charts 13274, 13279 and 13281 showing current R/V berthing location, (13281) cite of initial apparatus shakedown data and hydrographic survey information of the region. Significance of the bold insets are as below:

Chart 13281 = R/V berth near Blynman Canal

13279 = R/V berth and Annisquam River

13279 = Gloucester Harbor, Raw sewage outlet

13279 = Deep (56') "clear" water hole off Coffins Beach

13274 = Deep open waters off Castle Neck

13274 - Merrimack River test site.

13281 - Sheltered shakedown area.

TABLE 3-3

CLIMATOLOGICAL TABLE

BOSTON, MASSACHUSETTS (42°22'N., 71°02'W.) Elevation 15 ft. (4.57m)

WEATHER ELEMENTS	JAN.	FEB.	MAR.	APR.	MAY	JUNE	JULY	AUG.	SEPT.	OCT.	NOV.	DEC.	YEAR	YEARS OF RECORD
SEA LEVEL PRESSURE														
Mean (Millibars)	1016.7	1015.2	1014.1	1014.9	1014.5	1013.5	1014.5	1015.7	1017.9	1017.9	1017.2	1017.0	1015.8	30
TEMPERATURE (DEGREES F)														
Mean	29.2	30.4	38.1	48.6	58.6	68.0	73.3	71.3	64.5	55.4	45.7	33.0	51.3	30
Mean Daily Maximum	35.9	37.5	44.6	56.3	67.1	76.6	81.4	79.3	72.2	63.2	51.7	39.3	58.7	30
Mean Daily Minimum	22.5	23.3	31.5	40.8	50.1	59.3	65.1	63.3	56.7	47.5	38.7	26.6	43.8	30
Extreme Highest	72	68	85	91	93	100	100	101	100	90	83	70	101	30
Extreme Lowest	-12	-4	1	17	34	45	53	47	37	30	15	-4	-12	30
RELATIVE HUMIDITY														
Average Percentage	64.9	64.3	63.1	63.5	65.4	66.6	67.8	70.2	70.3	68.4	67.8	64.9	66.4	20
CLOUD COVER														
Average Amount (Tenths)	6.2	6.2	6.4	6.5	6.5	6.2	6.2	5.6	5.5	5.5	6.4	6.2	6.1	39
Equal to or less than 3/10 average amount, Mean Number of Days	9	8	8	7	6	7	7	9	10	11	8	9	99	39
Equal to or more than 8/10 average amount, Mean Number of Days	15	13	15	14	14	13	12	11	11	12	15	15	160	39
PRECIPITATION														
Mean Amount (Inches)	3.69	3.54	4.01	3.49	3.47	3.19	2.74	3.46	3.16	3.02	4.51	4.24	42.52	30
Greatest Amount (Inches)	9.54	7.08	11.00	7.82	13.38	8.63	8.12	17.09	8.31	8.68	8.18	9.74	17.09	23
Least Amount (Inches)	0.89	1.15	1.48	1.24	0.53	0.48	0.52	0.83	0.35	0.96	1.72	1.03	0.35	23
Maximum in 24 hrs. (Inches)	2.07	2.68	4.13	2.31	5.74	2.46	2.42	8.40	5.64	4.26	3.33	4.17	8.40	23
Mean Amount of Snow (Inches)	12.0	12.0	8.7	.8	*	0.0	0.0	0.0	0.0	*	.7	8.5	42.7	20
Maximum Snowfall in 24 hrs. (Inches)	12.8	19.4	17.7	3.1	*	0.0	0.0	0.0	0.0	*	8.0	13.0	19.4	39
Mean Number of Days with Snow (One Inch or More)	3	3	2	*	0	0	0	0	0	0	*	2	11	39
0.01 Inch or More, Mean Number of Days	12	11	11	12	12	11	9	10	9	9	12	12	128	39
WIND														
Mean Wind Speed (Knots) (06-08)l. s. t.	12.0	12.0	12.1	11.6	10.3	9.2	8.6	8.5	9.2	9.9	11.0	11.6		20-21
Mean Wind Speed (Knots) (15-17)l. s. t.	12.7	13.2	14.3	14.4	13.4	12.4	11.8	11.6	11.4	11.7	12.2	12.5		20-21
Direction (Percentage of Obs.): (06-08)l. s. t.														
North	8.0	7.4	6.3	4.2	3.5	4.3	4.0	6.0	7.1	7.8	7.7	7.8		20-21
North Northeast	3.6	3.7	6.4	5.4	5.8	4.6	4.0	6.3	6.8	7.6	4.8	3.0		20-21
Northeast	2.0	2.0	5.0	6.0	6.5	6.2	4.9	6.7	6.5	3.8	2.7	1.2		20-21
East Northeast	2.3	1.9	3.6	6.0	7.7	4.7	3.9	3.7	3.1	3.2	3.0	1.1		20-21
East	1.1	2.4	3.2	4.5	3.9	3.1	2.8	2.9	2.7	3.1	1.4	1.7		20-21
East Southeast	1.4	2.1	3.2	4.1	3.7	2.4	2.1	1.9	.8	1.5	1.7	1.1		20-21
Southeast	1.2	1.7	1.9	2.8	3.1	3.3	2.3	1.3	1.6	1.1	1.8	1.1		20-21
South Southeast	2.1	2.8	2.9	2.5	3.8	3.8	2.9	2.2	2.1	1.8	2.5	1.7		20-21
South	4.0	3.3	3.4	4.2	4.1	5.1	5.0	5.0	4.7	4.4	3.6	4.2		20-21
South Southwest	5.0	4.8	4.2	6.4	6.0	7.5	8.1	8.8	8.8	5.6	6.2	4.6		20-21
Southwest	7.4	5.8	5.8	9.0	9.7	13.5	13.2	11.8	11.1	10.4	10.7	11.1		20-21
West Southwest	8.3	7.7	5.8	8.2	7.0	9.9	8.9	8.6	7.2	7.1	6.9	9.2		20-21
West	10.8	9.3	8.4	8.3	7.7	7.9	10.8	9.9	8.1	8.2	9.8	11.3		20-21
West Northwest	15.9	16.3	12.9	11.3	10.5	9.5	12.7	11.9	10.4	11.6	12.8	16.6		20-21
Northwest	14.7	15.7	14.1	10.9	9.4	8.6	8.3	8.1	10.1	12.1	13.2	14.6		20-21
North Northwest	11.7	12.7	12.3	7.9	7.1	4.9	5.3	5.9	10.1	9.0	9.4	9.1		20-21
Calm	.6	.4	.7	.5	.7	.6	1.0	1.0	.9	1.7	1.7	.4		20-21
Direction (Percentage of Obs.): (15-17)l. s. t.														
North	6.5	4.2	3.0	1.7	2.2	0.9	0.5	1.5	2.0	2.8	4.5	5.4		20-21
North Northeast	3.5	2.7	3.3	2.5	3.0	1.6	1.3	2.0	3.2	3.7	3.1	3.2		20-21
Northeast	3.9	5.2	4.4	3.9	4.7	3.2	1.9	3.0	3.9	6.3	4.3	3.4		20-21
East Northeast	2.2	4.1	6.7	6.0	7.7	5.3	5.2	4.8	6.2	5.1	4.4	3.4		20-21
East	2.3	4.8	8.4	9.4	10.2	10.0	8.6	8.9	8.7	7.8	3.8	2.5		20-21
East Southeast	3.1	6.9	8.4	11.8	13.0	12.8	13.8	14.9	11.2	9.8	5.3	2.3		20-21
Southeast	2.8	4.5	7.3	9.3	7.9	7.4	9.1	11.3	9.1	7.8	5.7	3.0		20-21
South Southeast	1.9	2.9	2.1	3.0	3.3	3.8	3.3	4.9	3.9	3.8	2.9	3.3		20-21
South	2.7	3.1	3.1	5.1	6.4	4.6	5.2	4.4	4.5	4.2	3.8	4.2		20-21
South Southwest	4.9	3.9	5.4	7.5	8.8	10.4	10.9	8.4	9.1	6.5	7.3	5.4		20-21
Southwest	8.4	5.5	6.1	5.9	6.8	13.0	11.4	8.9	10.7	10.1	10.2	9.7		20-21
West Southwest	6.4	6.3	3.7	4.3	4.1	5.1	7.8	7.3	4.5	5.7	5.2	8.9		20-21
West	10.5	9.6	7.7	6.0	5.1	6.4	6.9	5.8	5.2	5.7	9.1	8.8		20-21
West Northwest	15.4	16.3	11.2	10.2	6.9	7.3	6.5	6.2	5.9	7.2	12.6	15.9		20-21
Northwest	18.1	12.5	11.7	8.7	6.0	4.6	4.8	3.8	7.8	7.5	11.0	13.1		20-21
North Northwest	10.0	7.8	7.8	4.8	3.9	3.3	2.5	3.7	4.0	5.8	6.8	7.8		20-21
Calm	.4	.6	.1	.1	.1	.2	.1	.1	.0	.6	.2	.4		20-21
VISIBILITY														
Days with Visibility less than 1/4 mile	2	2	2	2	3	2	2	2	2	2	2	1	23	39

TABLE 3-4

MEAN SURFACE WATER TEMPERATURES (T) AND DENSITIES (D)

Stations	Years	Jan		Feb		Mar		Apr		May		June		July		Aug		Sept		Oct		Nov		Dec		Mean	
		(T) °C	(D) σ_{15}	(T) °C	(D) σ_{15}	(T) °C	(D) σ_{15}	(T) °C	(D) σ_{15}	(T) °C	(D) σ_{15}	(T) °C	(D) σ_{15}	(T) °C	(D) σ_{15}	(T) °C	(D) σ_{15}	(T) °C	(D) σ_{15}	(T) °C	(D) σ_{15}	(T) °C	(D) σ_{15}	(T) °C	(D) σ_{15}	(T) °C	(D) σ_{15}
Eastport, Maine 44°54'N., 66°59'W.	40	3.3	23.8	1.7	23.7	1.7	23.6	2.9	23.3	4.7	23.2	6.8	23.5	9.2	23.8	10.7	24.0	11.0	24.1	10.3	24.2	8.6	24.0	5.9	23.8	6.4	23.8
Bar Harbor, Maine 44°23'N., 68°12'W.	23	1.4	23.7	0.4	23.7	1.7	23.5	4.6	23.2	7.8	23.2	11.3	23.3	13.7	23.5	14.2	23.6	13.1	23.8	11.1	24.0	8.3	23.9	4.3	23.7	7.6	23.6
Portland, Maine 43°40'N., 70°15'W.	37	0.7	22.3	0.1	22.1	1.5	21.3	4.6	20.5	8.8	20.8	12.7	21.6	15.2	22.3	15.6	22.5	14.4	22.5	11.2	22.5	7.3	22.2	3.1	22.0	7.9	21.9
Portsmouth, N.H. 43°05'N., 70°45'W.	26	2.1	21.7	1.3	21.5	2.3	19.7	5.6	18.1	9.2	19.7	12.7	21.4	15.0	22.5	15.8	22.9	14.6	23.0	11.3	23.0	8.2	22.1	4.5	21.2	8.6	21.4
Boston, Mass. 42°21'N., 71°03'W.	48	1.8	21.0	1.2	20.9	3.4	19.1	7.4	18.8	11.9	19.8	16.0	20.9	18.3	21.8	18.8	22.0	17.5	21.8	13.5	22.0	9.1	21.5	4.3	21.3	10.3	20.9

F (Fahrenheit) = 1.8C (Celsius) + 32

Density as used in this table is the specific gravity of the sea water or the ratio between the weight of a sea-water sample and the weight of an equal volume of distilled water at 15°C (59°F). These figures representing density at 15°C (ρ_{15}) are expressed in terms of sigma-t (σ_t) where t = 15°C and σ_{15} = (ρ_{15} – 1) 1000. Thus, for ρ_{15} = 1.0238, σ_{15} = 23.8. Obtain the pamphlet, "Surface Water Temperature and Density, Atlantic Coast, North and South America, C&GS Publication 31-1", for greater detail; for sale by Superintendent of Documents, U.S. Government Printing Office, Washington, D.C. 20402.

TABLE 3-5

METEOROLOGICAL TABLE FOR COASTAL AREA OFF BOSTON

Boundaries: From 42°N. northward to coast, and from 66°W. westward to coast

Weather elements	Jan.	Feb.	Mar.	Apr.	May	June	July	Aug.	Sep.	Oct.	Nov.	Dec.	Annual
Wind ≥ 34 knots (1)	7.7	8.5	5.1	2.8	.7	*	*	*	*	2.2	4.6	9.0	3.5
Wave height ≥ 10 feet (1)	13.5	12.3	8.3	4.4	1.8	.6	*	.8	2.6	7.0	12.3	12.3	6.4
Visibility < 2 naut. mi. (1)	9.6	10.2	10.8	11.8	16.7	25.7	35.7	31.6	16.0	11.4	7.3	11.0	16.5
Precipitation (1)	18.9	20.9	13.9	10.2	8.9	8.0	4.1	5.3	6.1	6.1	11.9	21.3	11.3
Temperature ≥ 85°F (1)	0	0	0	0	0	*	*	*	0	0	0	0	*
Mean Temperature (°F)	32.2	31.5	35.7	41.1	47.2	54.4	60.1	61.6	58.4	53.2	45.4	36.1	48.1
Temperature ≤ 32°F (1)	47.7	51.5	25.0	3.4	0	0	0	0	0	*	2.9	34.5	13.8
Mean relative humidity (%)	81	81	81	82	86	88	90	90	86	82	79	81	84
Sky overcast or obscured (1)	45.5	42.8	38.3	36.0	37.3	35.8	41.5	40.6	31.4	29.0	44.2	49.0	39.3
Mean cloud cover (eighths)	5.7	5.5	4.9	4.6	4.8	4.9	5.1	4.8	4.2	4.2	5.7	6.0	5.0
Mean sea-level pressure (2)	1014	1013	1014	1015	1015	1015	1016	1015	1018	1017	1017	1015	1015
Extreme max. sea-level pressure (2)	1046	1044	1041	1042	1038	1033	1031	1034	1038	1041	1041	1041	1046
Extreme min. sea-level pressure (2)	974	970	971	977	986	989	993	992	988	983	980	971	970
Prevailing wind direction	NW	NW	NW	SW	SW	SW	SW	SW	SW	SW	NW	NW	SW
Thunder and lightning (1)	0	*	*	*	*	*	*	*	*	*	*	*	*

(1) Percentage frequency.
(2) Millibars.
* 0.0-0.5%

These data are based upon observations made by ships in passage. Such ships tend to avoid bad weather when possible, thus biasing the data toward good weather samples.

Figure 3-18. R/V Berth Near Blyman Canal

(Chart 13281)

Figure 3-19. R/V Berth and Annisquam River

(Chart 13279)

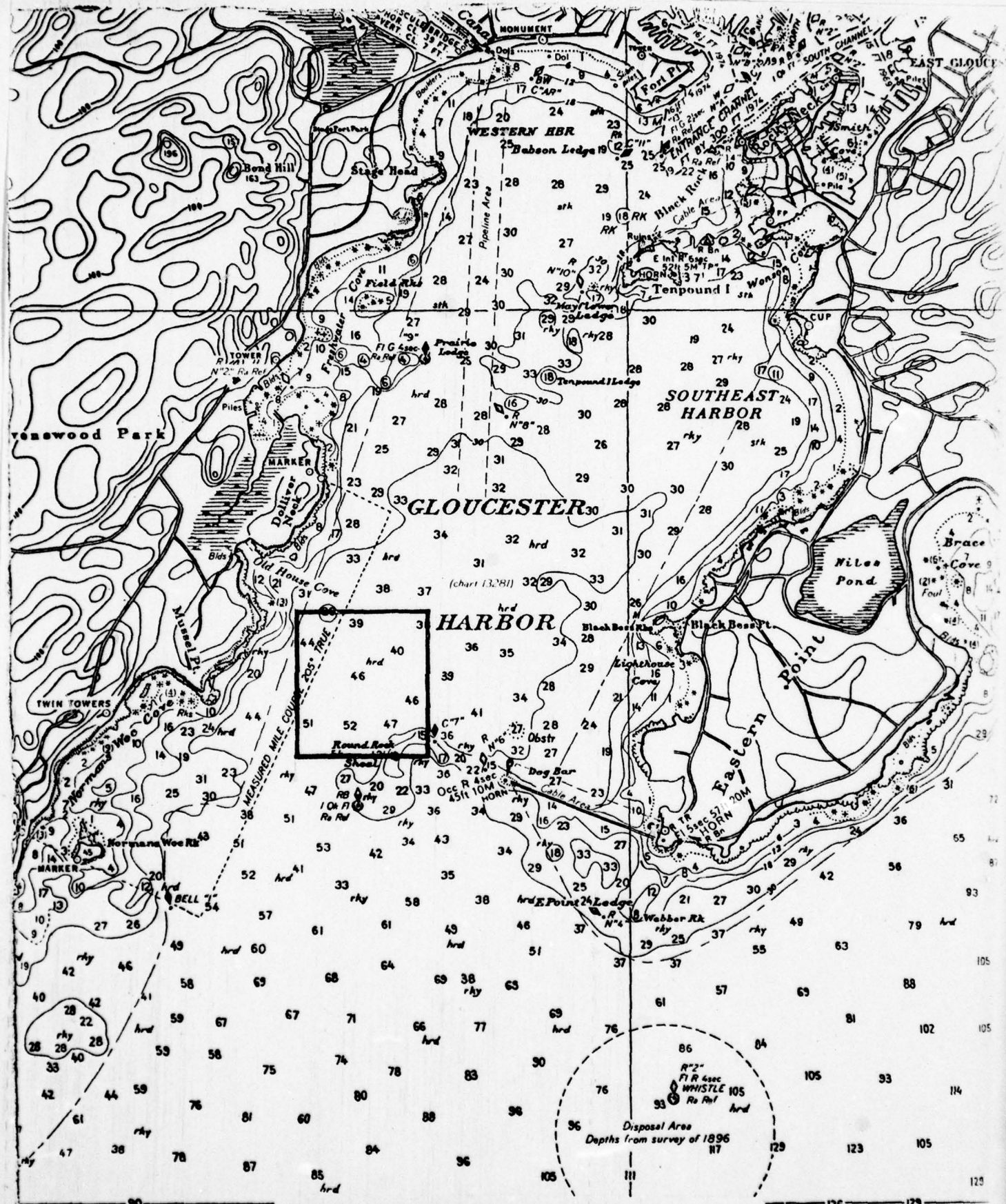

Figure 3-20. Gloucester Harbor, Raw Sewage Outlet.

(Chart 13279)

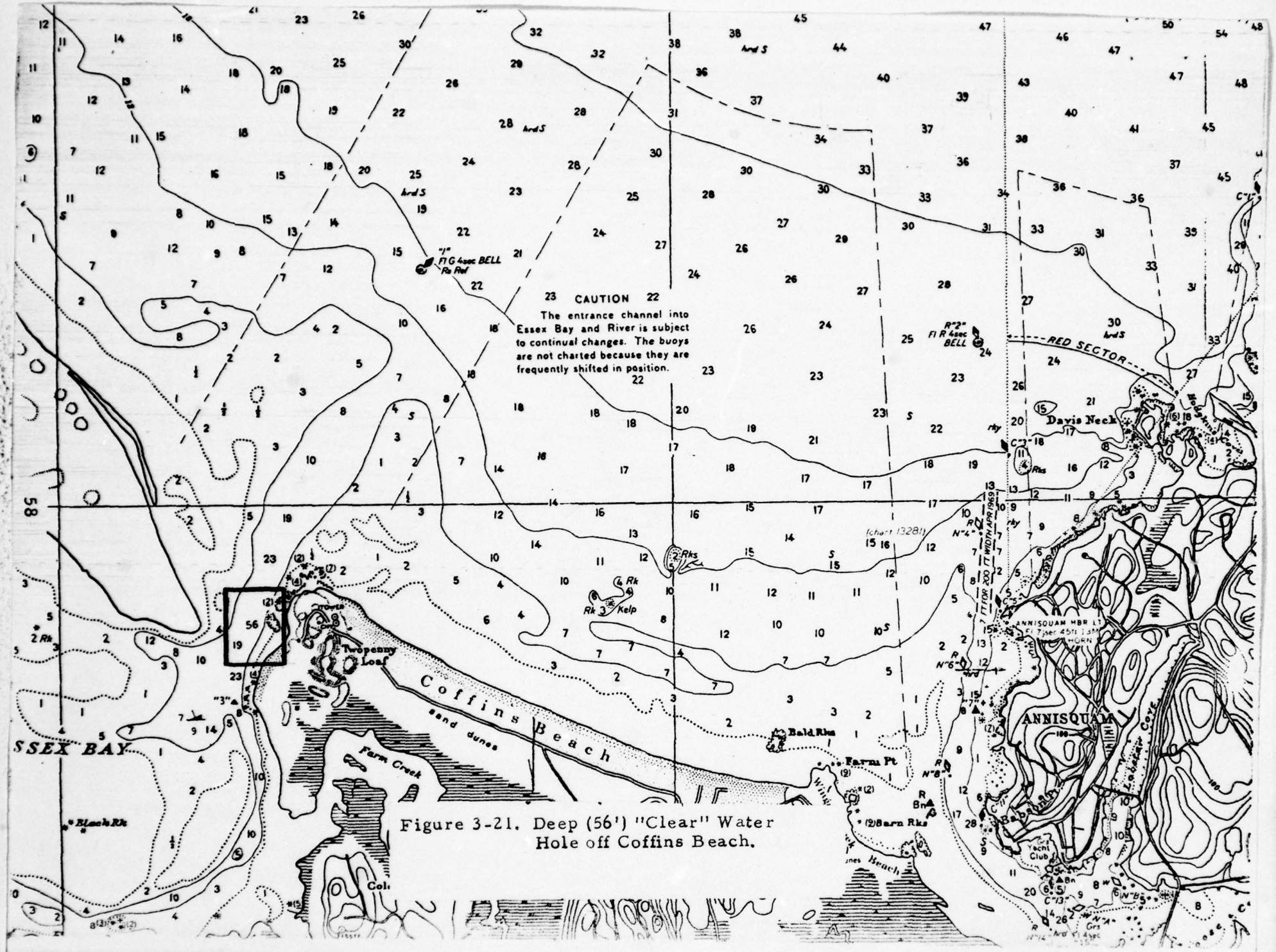

Figure 3-21. Deep (56') "Clear" Water Hole off Coffins Beach.

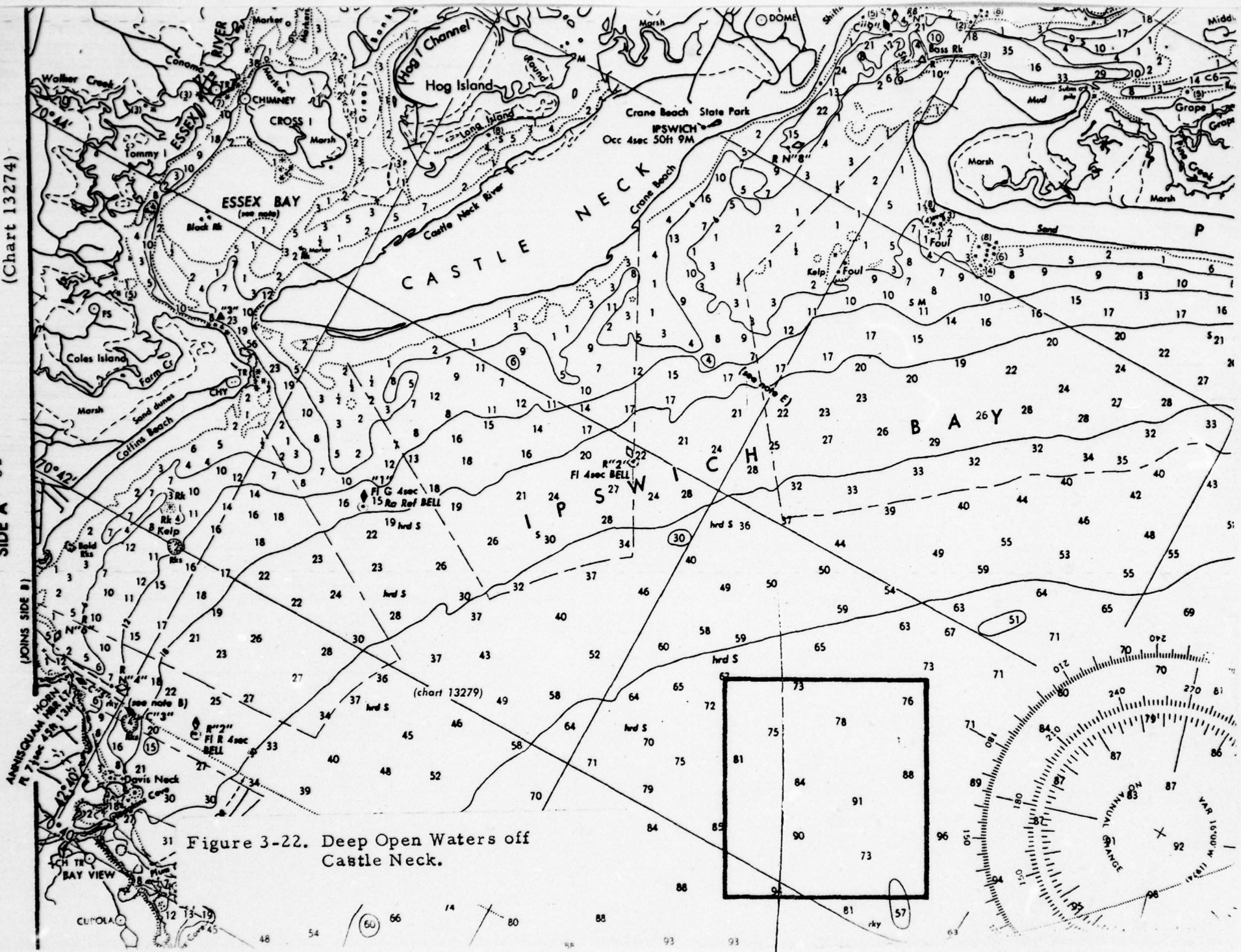

Figure 3-22. Deep Open Waters off Castle Neck.

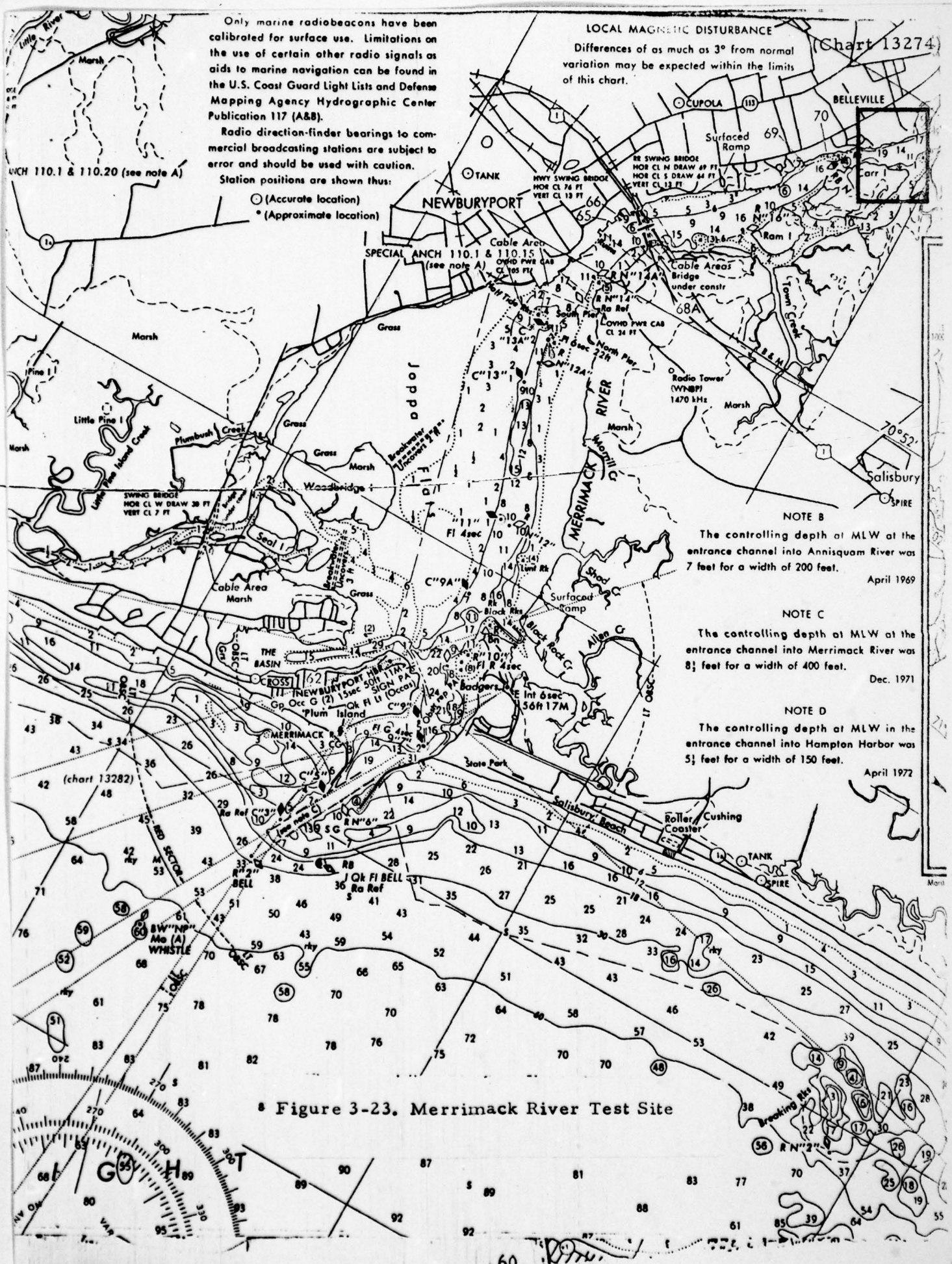

Figure 3-23. Merrimack River Test Site

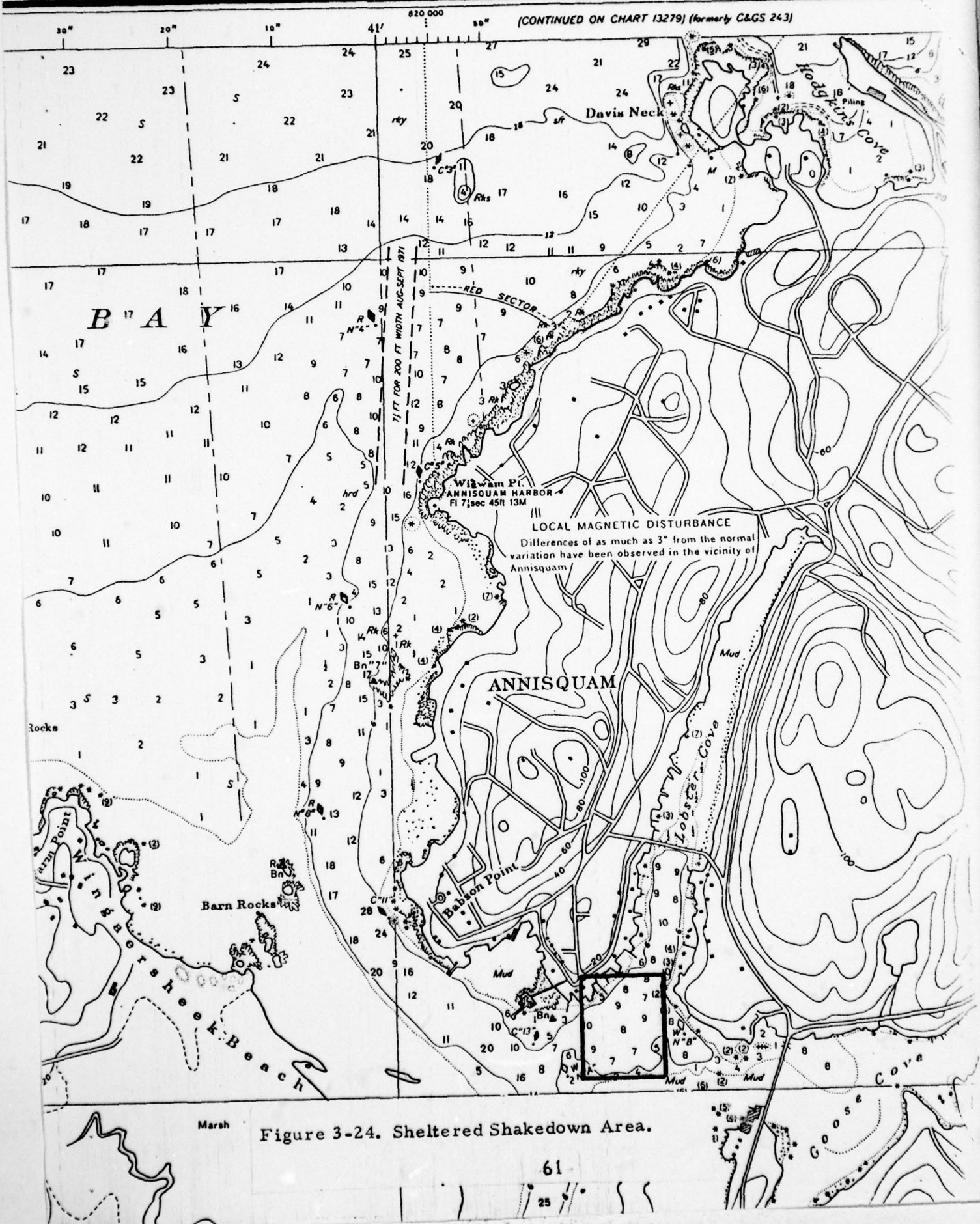

Figure 3-24. Sheltered Shakedown Area.

3.4 Q & A on Fundamental and Planned Experimental Techniques

During the course of the Task I performance period a number of questions were directed to our attention regarding both fundamental and planned experimental techniques from ONR and other interested parties.

This section compiles and directly addresses these questions in dialog format.

Question #1

What effect will surface waves have on the Raman subsurface temperature and salinity measurement if the measurement is made from an airborne platform?

Answer #1

The major surface effects relate to (a) the differential transmission of orthogonal linear polarizations, (b) the loss of depth resolution due to refraction produced by transmission through the air -water interface, and (c) the lateral errors also produced by refraction. The work on the present contract included calculations of the errors produced by polarization unbalance and the results which show less than a 1.0% effect, which is equivalent to a 1.0°C temperature error if uncorrected. This information is shown in Figure 3-3 of this report. The depth resolution effect and the lateral error were also investigated during the present contract and the results are shown in Figures 3-5 and 3-6.

Question #2

Will multiple scattering in natural waters be the limiting factor in the measurement?

Answer #2

It appears that multiple scattering will not be the limiting factor for at least the first 15 to 20 attenuation lengths. This is because (a) the very sharply forward peaked volume scattering function limits the beam spread to the order of 3 to 5° and (b) small angle scattering, i.e. 5° or less, exhibits negligible depolarization. For this assessment, the work on the present contract drew heavily upon the theoretical work of A. Gordon[30] and the experimental results of S. Q. Duntley[11]. In addition, original calculations were performed by CGC personnel during this reporting period to verify that Mie scattering at small forward angles has negligible depolarization and also to calculate the scaling laws that determine the effect of the fluctuation in depolarization on the error analysis of the measurement.

Question #3

To what extent will laser power fluctuations limit the measurement?

Answer #3

It is standard practice in laser Raman measurements to monitor the laser power and normalize the Raman signals to the laser power. In addition, real time computer techniques can be employed to repetitively scan spectral data and coherently add the Raman spectra, with noise sources such as laser power fluctuations being effectively subtracted out. Such techniques were utilized by CGC in the Raman combustion diagnostic system[31] that was installed in the Air Force Aero Propulsion Laboratory and produced Raman data with a precision exceeding 1%. Both techniques will be employed in the Raman subsurface temperature and salinity experiments. It is thus not expected that laser power fluctuations will be a limiting factor in the experiments.

Question #4

In the orthogonal polarization ratio technique experiments can the two photomultipliers be balanced to the extent required?

Answer #4

Photon counting techniques will be used, and in such a "0" or "1" mode of operation the constancy of the photoefficiency of the photocathode surface is the important factor, not the gain of the dynode chain. In addition the polarization channels can be optically alternated relative to the two photomultipliers to enable cross calibrations on a regular basis.

Question #5

How will the Raman subsurface temperature/salinity experiment compensate for ambient daylight background illumination, especially considering the fact that ambient upwelling ocean water irradiance is usually polarized?

Answer #5

Operating in the pulsed laser mode the experiment will provide for sampling of the ambient upwelling ocean water irradiance background during the time interval between laser pulses. With two polarization channels the ambient background in the orthogonal polarizations will be measured and separately applied as a background correction to the Raman measurements.

Question #6

It has been said that because the Raman effect is a "weak" interaction it may not produce sufficient signal for the remote measurement of subsurface ocean water temperature and salinity. Please comment.

Answer #6

Atmospheric scientists who have used the Raman technique to measure atmospheric water vapor profiles are familiar with the fact that the gas phase vibrational Raman cross-section is usually only one part in one thousand or less of the on-frequency Rayleigh backscatter. In liquid phase Raman applications not only is the molecular density several factors of 10 higher than that of gas phase molecular density, but also the per molecule Raman cross-section is considerably higher. For example, the Raman vibrational O-H band backscatter coefficient from distilled water is essentially equal to the on-frequency "Rayleigh" backscatter coefficient. As part of the work on the present contract the current status of the information available on the backscattering coefficients - both Raman and on-frequency-was researched. The results are shown in Table 2-1 of this report.

Question #7

Will salinity gradients interfere with the measurement of temperature? Can salinity also be measured by using the Raman spectrum? How accurate are the measurements?

Answer #7

If the depolarization ratio is spectrally resolved over the liquid water O-H band vibrational Raman band, it is observed that in the lower frequency portion of the band corresponding to the hydrogen bonded "ploymer-like" structures the depolarization ratio is essentially independent of salinity and is only a function of temperature. It is also observed that in the higher frequency portion of the band which corresponds to non-hydrogen bonded or "monomer-like" structures, the depolarization ratio is a function both of salinity and temperature.

Spectral analysis of the Raman depolarization ratio thus enables independent determination of temperature and salinity. The sensitivity of the temperature measurement requires a 1% measurement of the Raman depolarization ratio to obtain a $1^{o}C$ temperature precision. A three part per

thousand (ppt) accuracy in salinity requires 0.8% and 0.4% Raman measurement accuracies in the salinity ranges of 0 to 20 ppt and 20 to 40 ppt respectively. It should be noted that a temperature change of 1°C and a salinity change of 3 ppt each has the same relative effect on sound speed.

Question #8

What else can a high repetition rate pulsed laser Raman lidar system measure, if it is fully developed to measure water temperature and salinity?

Answer #8

The Raman backscatter from the water can also be analyzed to determine transmission as a function of depth. In addition the on-frequency return can be utilized as a bathymeter and as a wave profiler. Also, if employed from an airborne platform the same basic system can measure atmospheric temperature, water vapor, transmission, and wind profiles. The above described multi-mode utilization involves mainly additional software for data interpretation with relatively minor additional hardware costs.

Question #9

What depth resolution is possible?

Answer #9

The depth resolution depends on the laser pulse duration, the receiver band width and the properties of the water transmission medium, especially the refractive properties of the surface, i.e. the air-water interface. Off-the-shelf laser and receiver systems have demonstrated 30 cm resolution in bathymetric lidar systems, which are generically similar to a temperature/salinity lidar system. The effect of the surface was discussed in the Answer to Question #1, and the results obtained from the investigation during this reporting period are shown in Figure 3-5.

Question #10

Can the laser Raman method detect ice and measure its temperature?

Answer #10

Yes. The laser Raman technique has been shown[1] capable of detecting ice and measuring ice temperatures in the range from 0°C to - 50°C. The physical principle is the measurement of Stokes to anti-Stokes line ratios in ice, which are functions of temperature.

Question #11

Can a laser Raman system be built to produce measurements with an accuracy of 1% or better in a real world field environment as contrasted to what might be achieved in a controlled laboratory environment?

Answer #11

Laser Raman systems have been built for remote measurements in field environments and have achieved accuracies under such conditions of 1% or better. Such a system is the laser Raman combustion diagnostic system[21] that was installed and operated by CGC in the Air Force Aero Propulsion Laboratory. The combustion diagnostic system has a "measurement index" (i.e. ratio of laser photons transmitted to Raman photon collected) of $\sim 10^{-14}$ compared to $\sim 10^{-12}$ for a laser Raman water temperature/salinity measurement system. On the basis of "measurement index" a water temperature/salinity field system is a more conservative undertaking than what has already been demonstrated and operated under field conditions.

4.0 CONCLUSIONS AND RECOMMENDATIONS

This section summarizes the various major conclusions and recommendations that were developed during the course of the new work performed on the subject contract. The following items are arranged in the approximate order in which they are discussed in the Technical Summary Report.

Liquid Water Raman Cross-Section. A new value for the Raman cross-section for liquid water appeared in the recent literature[1] that is a factor of 5 greater than that previously reported. The implications of this higher value should be factored into future system design considerations.

Ice Measurements. It has also been reported in the recent literature[1] that the temperature of ice can be measured with Raman scattering. A multi-purpose Raman instrument is conceivable which remotely measures ice temperature in addition to liquid water temperature and salinity.

Surface Wave Refraction Effects. It was concluded that since surface wave refraction effects are of a relatively minor importance to both polarization measurements and to the depth and lateral resolution that is attainable, no attempt should be made in the initial experiments to improve the accuracy of the measurements by correlation on a laser pulse to pulse basis of the corresponding wave angles. Even for worst case Stokes limit waves of H/L = 0.143 the uncorrected errors are 0.6°C temperature, 2.8 parts per thousand salinity and 0.3% in depth resolution.

Depolarization by Transmission in Natural Waters. An important conclusion is that the polarization content of a beam of light is preserved essentially until the last photon has been absorbed, i.e. the attenuation coefficient is very much larger, the order of 100 times larger, than the depolarization coefficient.[11] Experiments should be carried out and are being planned to study the extent of the natural variability of the proportionality between ρ_s and K. This information will define the residual temperature and salinity

uncertainty that can be expected from a Raman measurement. Estimates are that with a 10% uncertainty in the value of the proportionality constant between ρ_s and K an uncertainty of 0.1°C in temperature and 0.7 parts per thousand in salinity will result. Experiments should concentrate on the variability and the uncertainty in the ratio of ρ_s to K for various types of natural water.

Depolarization by Transmission-Theory. Basic Mie scatter calculations confirmed the relatively weak, i.e. $\rho_s \approx 0.01$ K depolarization that had been experimentally observed in the forward direction.[11] The conclusion from the work is that direct experimental measurements of depolarization in various types of sea water would be more useful than further complex and idealized calculations.

Differential Attenuation and the Need for Multiwavelength Polarization Detection. A simultaneous multiwavelength detection or wavelength scanning detection capability is required if a reasonable depth capability is to be obtained even using a polarization ratio method. An experimental wavelength scanning capability with a wavelength resolution of a few tenths of nanometers is necessary.

Also, there is a requirement for a tunable laser source to position the Raman water band at or near the minimum of the diffuse attenuation (K) vs. wavelength curve. Both considerations were factored into the experimental plan.

Non-Raman Photon Noise Sources. The ambient background illumination should be separately sampled between laser pulses in both polarizations. Also, experiments will be designed under the proposed plan to measure the laser induced fluorescence to Raman ratio as a function of of laser excitation wavelength for a variety of coastal waters.

Experimental Apparatus Design. The conclusion is that suitable laser Raman equipment is now available at CGC for conducting meaningful experimental studies. An especially important aspect of the experimental apparatus design is the availability of an operational research vessel, the Makai, which is currently outfitted to conduct laser Raman experiments in coastal waters.

Preliminary Experimental Raman Data Obtained From Natural Waters. Temperature measurements from Raman spectra were obtained from natural waters aboard the Makai which agreed with laboratory calibrations. The fluorescence to Raman ratio in the waters selected for experiments was very low.

Experimental Field Test Plan. The coastal areas in the Gulf of Maine region offer a sufficient variety of well documented coastal waters so that meaningful experiments can be carried out in this region.

REFERENCES

1. Slusher, R.B. and Derr, V.E., "Temperature Dependence and Cross-Sections of Some Stokes and Anti-Stokes Raman Lines in Ice", Applied Optics, 14, 2116 (1975).

2. Chang, C.H. and Young, L.A., "Seawater Temperature Measurement from Raman Spectra", Final Technical Report, Contract N62269-73-C-0073, Sponsored by Advanced Research Projects Agency, ARPA Order No. 2194.

3. J. E. Tyler, "Scattering Properties of Distilled and Natural Waters", Limol. Oceanog. 6, 451 (1961).

4. N. G. Jerlov, "Optical Measurements in the Eatern North Atlantic," "Goteborg Kungl. Vetenskapsoch Vitterhets-Samhalles Handinger, Sjatte, Foljden, Ser B, 8, 11 (1961). (As described by Morrison. See Reference 5 below.) See also N. Jerlov, Optical Oceanography, Elsevier, Amsterdam, (1968).

5. R.E. Morrison, "Experimental Studies on the Optical Properties of Sea Water", J. Geophys. Res. 75, 612 (1970).

6. A.F. Spilhaus, "Observations of Light Scattering in Sea Water", Limnol. Oceanog. 13, 418-422 (1968).

7. S.Q. Duntley, "Light in the Sea", J. Opt. Soc. Am. 53, 214-233 (1963).

8. J.G. Hirschberg, et. al., "Laser Application to Measure Vertical Sea Temperature and Turbidity -Design Phase" Technical Report NASA Contract NAS10-8795, March, 1976.

9. E. Hecht and A. Zajac, Optics, (Addison - Wesley, Reading, Massachusetts, 1974, page 245.)

10. B. Kinsman, Wind Waves, (Prentice-Hall, Inc., Englewood Cliffs, New Jersey, 1965, page 241.)

11. Duntley, S.Q., "Underwater Lighting by Submerged Lasers and Incandescent Sources", Scripps Report, SIO-71-1, June 1971.

12. Brown, D.B. and H.R. Gordon, "Size - Refractive Index Distribution of Clear Coastal Water Particulates from Light Scattering", Applied Optics 13, 2874(1974).

13. Gilbert, G.D., et. al., "Underwater Experiments in Polarization" in Underwater Photo-Optics, SPIE, 1966.

14. Goody, R.M., "Atmospheric Radiation", Oxford Press, 1965.

15. Pangonis, W.J., et. al., "Tables of Light Scattering Functions", Wayne State University Press, Detroit, 1957.

16. Lowan, A.N., "Tables of Associated Legendre Functions", Columbia University Press, 1945.

REFERENCES
(Continued)

17. M. Lapp and C.M. Penny, Laser Raman Gas Diagnostics, Plenum Press, 1974, pp 3-10.

18. Leonard, D.A., "Field Tests of a Laser Raman Measurement System for Aircraft Engine Exhaust Emissions", Final Technical Report, Contract F33615-71-C-1875, Sponsored by Air Force Aero-Propulsion Laboratory, Technical Report AFAPL-TR-74-100 (1974).

19. Lapp. M., "Flame Temperatures from Vibrational Raman Scattering", published in the Proceedings of the Project SQUID Raman Workshop on the Measurement of Gas Properties held in Schenectady, New York, May 10-11, 1973, published by Plenum Press, N.Y. 1974.

20. Walrafen, G. E., J. Chem. Phys., 55, 768 (1961).

21. Schwiesow, R. L., "Raman Scattering Studies of Pollutant Systems", AIAA Paper 7-1086, November 1971.

22. Mulligan, H. and F. DeLara, 1974. Phytoplankton in the Gulf of Maine, In, The Research Institute of the Gulf of Maine Bureau of Land Management Review, Portland, Maine 200 pp.

23. Bigelow, H.B. 1927. Physical Oceanography of the Gulf of Maine, Bull. Bur. Fish. 40,Part 2, 511-1027.

24. Anonymous. 1971b. Water resources data for Massachusetts, New Hampshire, Rhode Island, Vermont, Part 1. Surface water records part 2. Water quality records. U.S. Dept.of the Interior Geol. Survey. 401 pp.

25. Ford, W.L. 1947. Hydrography of the western Atlantic, No. 3, The distribution of the Merrimack River effluent into Ipswich Bay, Woods Hole Oceanographic Institution Technical Report 23 pp.

26. Graham, J.J. 1970. Coastal currents of the western Gulf of Maine, International Commission for the Northwest Atlantic Fisheries 7:19-31.

27. Day, G.C. 1958. Surface circulation in the Gulf of Maine as deduced from drift bottles, Fish. Bull. 141 U.S. Fish and Wildlife Service pp. 443-472.

28. Manohar-Mararaj, V and R.C. Beardsley, Part 1; Karpen J., Part II, 1974. Mass. Inst. of Technology Technical Report 74-9 NTIS: COM-74-10407, 109 pp.

REFERENCES

(Continued)

29. Proceedings of the First International Conference on Toxic Dinaflagellate Blooms, Boston, Massachusetts, November 4, 5, 6, 1974 (MIT Sea Grant Report No. MITSG 75-8).

30. A. Gordon, "Practical Approaches to Underwater Multiple - Scattering Problems", SPIE Vol. 64 (1975), Ocean Optics, 85-93.

31. Leonard, D. A. and Caputo, B., "Development of a Raman System as a Combustion Diagnostic Tool", Final Technical Report, Contract F33615-75-C-2023, Sponsored by Air Force Propulsion Laboratory, Technical Report AFAPL-TR-75-99 (1975).

APPENDIX A

PHYSICAL AND MATHEMATICAL JUSTIFICATION

1.0 INTRODUCTION

This appendix describes the physical basis and the mathematical justification for the airborne subsurface temperature area profiles.

2.0 BACKGROUND

Liquid water is one of the most common substances on the earth, it is necessary for life and is of wide practical utility. Because of its basic importance to man, water has been the subject of considerable scientific inquiry and its spectroscopy is, in general, well understood.

The H_2O molecule is highly polar and possesses a large dipole moment. This fact together with its atomic composition allows the H_2O molecule in the liquid state to interact with other nearby H_2O species and form hydrogen bonds. An individual H_2O molecule may participate in a maximum of four hydrogen bonds - one for each H-atom and two for the O-atom.

The fact that liquid water contains hydrogen bonding is apparent from its infrared and Raman spectroscopy. The fundamental vibration frequencies due to the O-H bond occur at 3652 cm^{-1} (symmetric stretch) and 3750 cm^{-1} (asymmetric stretch). The O...H hydrogen bond that occurs in the liquid state perturbs the fundamental frequency, so that the infrared and Raman spectra due to O-H in liquid water show spectral broadening and shifts to lower frequencies in the 3400 to 3500 cm^{-1} range. Since the hydrogen bond is relatively weak, having an energy of only a few kcal/mole, the extent of hydrogen bonding in liquid water is very sensitive to temperature. By monitoring the Raman spectrum of water in the O-H stretch region, this variation in structure due to the mobility of the hydrogen bonds may be observed and provides a means for measuring the temperature.

Walrafen (References A1, A2, A3) was one of the first to observe the fact that the Raman spectrum of liquid water in the O-H stretch region shifted toward longer wavelengths with increasing temperature. It was also observed that a much smaller red shift occurs as ionic species, e.g. Cl-ions, are added to the water. Both of these phenomena, as well as additional spectroscopic information and other data have been used to support the hypothesis that liquid water contains H_2O clusters held together by substantial hydrogen bonding in rapid equilibrium with monomeric H_2O molecules. As the water temperature increases, this equilibrium shifts to a larger fraction of unbonded units. Analogously, as the ionic concentration is increased, the hydrogen bonded structures would be decreased since more H_2O molecules would be needed to cluster around the ionic species.

3.0 TWO COLOR METHOD

This model is shown in a heuristic manner in Fig. A-1. Liquid water is considered as being composed of two species, polymers which are hydrogen bonded and monomers which are not, both in rapid equilibrium with each other. Each species has its individual Raman spectrum proportional to its concentration as shown in

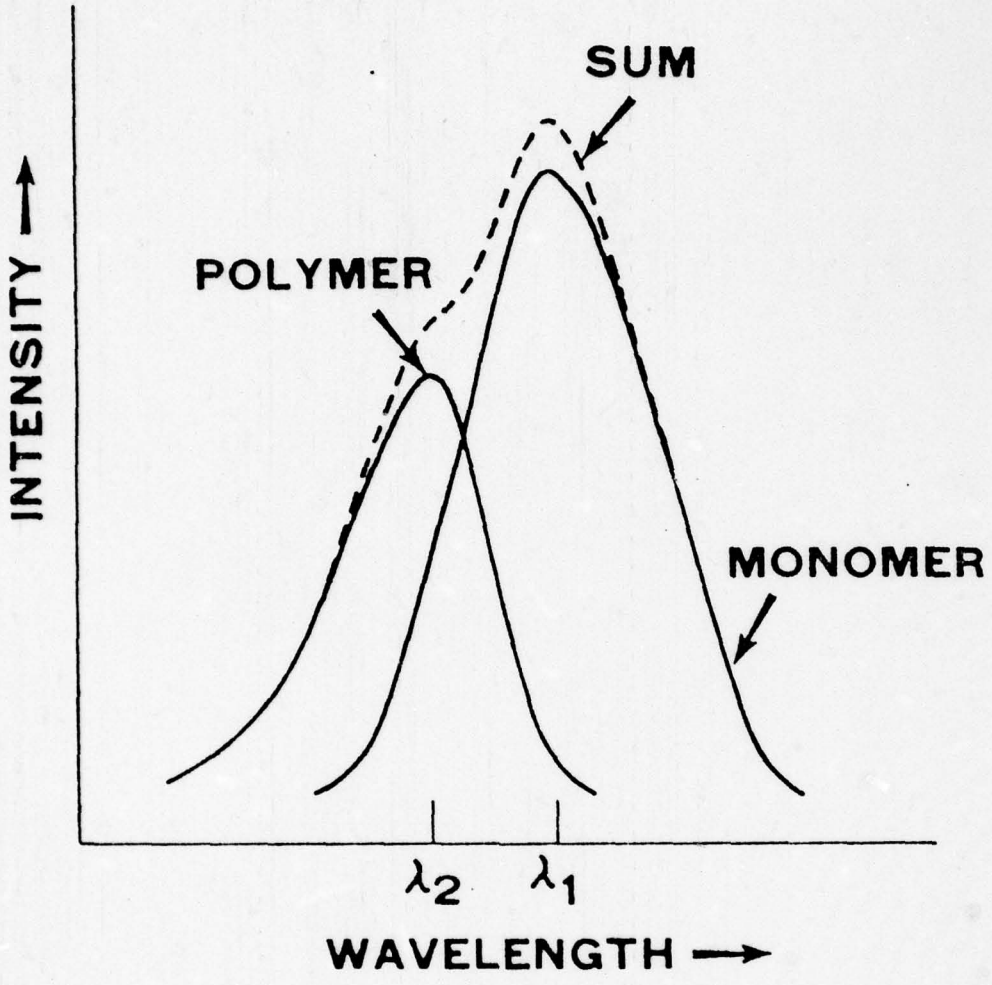

$$\text{POLYMER} \underset{}{\overset{K(T)}{\rightleftharpoons}} \text{MONOMER}$$

$$I(\lambda_1)/I(\lambda_2) \propto (\text{MONOMER})/(\text{POLYMER}) = f(T)$$

Figure A-1. Raman Spectrum and Structure of Liquid Water.

the schematic; the total observed Raman spectrum being composed of the sum. Simultaneous measurement of the Raman spectra at the two wavelengths λ_1 and λ_2 provides a measure of the concentration ratio, and through the equilibrium constant, the temperature. Such a two-species mixture model of liquid water has previously been successfully used in interpreting sound absorption measurements (Reference A4), and infrared (References A5 and A6) and Raman (References A2 and A7) spectroscopic studies.

Chang and Young (Reference A8) experimentally demonstrated the feasibility of the two color technique in a series of laboratory measurements. They used a N_2 pumped dye laser to obtain a laser source with a wavelength between 4200 and 4600 Å. In an extensive series of experiments Chang and Young studied the sensitivity of the temperature measurement to the location of the two detected colors and to changes in water salinity.

Some of the major conclusions of this feasibility study were: (1) over a wide range of temperature (0-50°C) the technique was linear with temperature, (2) two colors could be found which maximized the temperature sensitivity and minimized the salinity effect, (3) a measurement sensitivity of 1% per C° was demonstrated and (4) a two color field system for water temperature measurement was found to be feasible. The differential attenuation of the Raman band at depths corresponding to several attenuation lengths was identified as requiring an independent measurement of transmission as a function of wavelength as a calibration requirement in the two color method.

4.0 DEPOLARIZATION METHOD

As mentioned previously, liquid water may be considered as a mixture of species which are completely hydrogen bonded and those which are not. The former possess symmetric structure and vibrations and would be expected to preferentially scatter polarized radiation. Hence, in the same way that liquid water structure is reflected in the shape of the Raman spectrum, similar information is contained in the polarization of the scattered radiation.

Porto (Reference A9) has shown that the total Raman intensity, I, as a function of scattering angle, θ, is given by the expression

$$I(\theta) = \frac{k\, I_o}{45} \left[45\ a^2 + 7\ \beta^2\right]$$

where I_o is the intensity of the incident radiation and a and β are the isotropic and unisotropic part of the differential polarizability tensor. a and β are related to the molecular polarizability and are temperature dependent. For observation of backscattered radiation, $\theta = 0$. For linear polarized incident radiation, a depolarization ratio ρ_ℓ can be defined

$$\rho_\ell = \frac{I_\perp}{I_\parallel} = \frac{3\ \beta^2}{45\ a^2 + 4\ \beta^2}$$

where $I_{\perp}$ and $I_{\parallel}$ are the parallel and perpendicular polarized polarization intensities. As has been shown by Murphy and Bernstein (Reference A7) the bulk of the Raman return for water is composed of $I_{\parallel}$. Hence ρ_l is a small number and the accuracy of such a measurement is inherently low.

However, circularly polarized light can be used for Raman scattering, and in an analogous manner to the plane polarized radiation, the scattered return will contain components of both circular polarizations. A reversal coefficient or circular depolarization ratio, ρ_c, can be defined and related to the linear depolarization ratio (Reference A13):

$$\rho_c = \frac{I_l}{I_r} = \frac{2\rho_l}{1-\rho_l} ,$$

when I_l and I_r are the left and right circularly polarized return respectively. Since $\rho_l \leq 3/4$, $\rho_c \leq 6$ and is a more accurate measurement of water temperature than ρ_l.

Chang and Young (Reference A8) were able to determine the circular depolarization ratio of liquid water as a function of temperature. They found that the ratio was approximately linear over a temperature range of about 10-45°C and determined an average sensitivity of about 1%/C° which is comparable to the maximum sensitivity observed for the two color method. In addition, they found that the circular depolarization ratio varied with salinity, but were able to find wavelength regions where the salinity effect was minimal and could be neglected for all but the most accurate measurements.

The performance of the temperature measurement system utilizing the depolarization ratio will be degraded by any uncalibrated effect which depolarizes either the laser beam or the Raman scattered beams. Particulates in the ocean will cause some depolarization by single and multiple off axis scattering. Single scattered light scattered at very small angles, e.g. 10^{-3} radians, will be collected by the receiver. Scattered light at larger angles can be collected when multiple scattering occurs. The off axis scattered light from a particle in general will be elliptically polarized. Because the nature of the scattering in the ocean cannot be universally characterized, the temperature sensitivity of the system will be degraded. Chang and Young performed experiments to determine the degradation of system performance. Their estimate was that small angle scattering would introduce an absolute temperature uncertainty of 0.3°C per attenuation length. This uncertainty is independent of laser power or integration time.

5.0 NUMERICAL CALCULATION

The number of Raman photoelectrons collected per second by an optical detector in a pulsed laser backscattering system can be expressed by the following equation:

$$N_{PE} = N_{LASER}\ N_{SCAT}\ \sigma_{RAMAN}\ \Delta R\Omega\ \epsilon_{pe}\ \epsilon_{op}\ T_{\lambda_1}\ T_{\lambda_2}$$

where:

N_{PE}	=	number of Raman photoelectrons detected
N_{LASER}	=	number of laser photons per second
N_{SCAT}	=	density of molecular scatters of a given species
σ_{RAMAN}	=	Raman scattering cross-section per particle per steradian
ΔR	=	range resolution
Ω	=	detection solid angle
ϵ_{pe}	=	photocathode photoelectric efficiency
ϵ_{op}	=	optical system efficiency
$T_{\lambda_1}\ T_{\lambda_2}$	=	two-way transmission, T_{λ_1} at laser wavelength T_{λ_2} at Raman wavelength

It can be seen from the above that if the transmitter and receiver system parameters are known and if the Raman scatterer has a known cross-section and density, such as liquid water, then a measure of the Raman scattering from a single range cell can be used to determine the two-way transmission to that range cell. The system thus acts as a single-ended transmissometer. The Raman technique for transmission measurements in the atmosphere has already been demonstrated by Leonard and Caputo (Reference A10).

A calculation was carried out for the baseline Raman system using the above range equation with system parameters that assume state-of-the-art well engineered components. The parameters assumed are listed in Table A-1 with a brief rationale for the particular choice.

The product of the system parameters shown in Table A-1 yields a total Raman signal return of 3.5×10^5 photoelectrons per second with the assumption of unity two-way transmission loss. As has been previously shown, (Reference A11) in a well engineered Raman system using a pulsed laser, the limiting noise can be reduced to the "shot noise" in the laser induced signal itself. Therefore, the S/N ratio can be given by the square root of the total number of photoelectrons collected in a given measurement interval. If the signal in the above calculation is assumed to be equally divided between the two polarizations a basic S/N of (1.75×10^5) 1/2 or 418 would be available. Based on a measurement sensitivity of 1% per C^o (Reference A8). This would mean that a temperature precision of $(1/418) \times 100 \approx 0.3\ C^o$ would have been achieved.

The ability to achieve depth penetration depends critically on the attenuation coefficient of the particular water and is highly variable among open ocean,

continental shelf and coastal waters. Table A-2 lists the various types of ocean waters with values of attenuation coefficients, optimum transmission window ranges and the rate of laser beam power loss in dB per meter.

TABLE A-1

BASELINE SYSTEM PARAMETERS

System Parameter	Value Assumed	Rationale
N_{Laser}	2.3×10^{17} $\frac{\text{photons}}{\text{sec}}$	This value corresponds to 0.1 watt of average power at 4600 Å. Commercially available N_2-pumped dye lasers have this capability.
N_{Scat} σ_{Raman}	3×10^{-5} ster^{-1} m^{-1}	This is the latest published value for the experimentally measured total Raman liquid water backscatter coefficient. (Reference A8)
ΔR	1 meter	Corresponds to minimum depth resolution set by pulse duration of laser.
Ω	10^{-6} ster	This collection solid angle corresponds to a 30 cm effective diameter collector on a platform 300 meters above the scattering volume.
ϵ_{op} ϵ_{pe}	5×10^{-2}	Typical overall optical and photoelectric quantum efficiency.

TABLE A-2

UNDERWATER WINDOWS FOR VARIOUS OCEAN WATERS*

WATER TYPE			TRANSMISSION WINDOW		
TYPE	LOCATION		K (m^{-1})	Loss (dB/m)	(nm)
Clearest Ocean	Open Ocean; Tropical and Subtropical	Below Thermocline	0.02	0.087	430-470
		Above Thermocline	0.03	0.130	440-480
Warm Ocean			0.04	0.170	470-490
Cool Ocean	Open Ocean; Temperate Subartic and Artic		0.07	0.300	475-495
Shelf	Continental Shelf	Surface to Bottom	0.10	0.430	490-510
Coastal	Coastal; Relatively Shallow Water	Surface to Bottom	0.16	0.695	510-550
Very Turbid	Inshore Coastal; Harbor and Bay Water	Surface to Bottom	0.40	1.737	550-570

*See Reference A12.

APPENDIX A - REFERENCES

A1 Walrafen, G.E., J. Chem. Phys., 55, 768 (1961)

A2 Walrafen, G.E., J. Chem. Physics, 47, 114 (1967)

A3 Walrafen, G.E., J. Chem. Physics 48, 244 (1968)

A4 Lieberman, J., Acoustic Soc. Amer. 28, 1253 (1956)

A5 Thomson, et. al., Nature 211, 1086 (1966)

A6 Worley, J.D. and Klotz, I.M., J. Chem. Physics 45, 2868 (1966)

A7 Murphy, W.F. and Bernstein, H.J., J. Phys. Chem. 76, 1147 (1972)

A8 Chang, C.H., and Young, L.A., "Seawater Temperature Measurement from Raman Spectra", Final Technical Report Contract N62269-73-C0073, Sponsored by Advanced Research Projects Agency, ARPA Order No. 2194

A9 Porto, S.P.S., J. Opt. Soc. Amer. 56, 1585 (1966)

A10 Leonard, D.A. and Caputo, B., "A Single-Ended Atmospheric Transmissometer", Optical Engineering 13, 10 (1974)

A11 Leonard, D.A., "Combustion Gas Measurements Using Raman Scattering", AIAA Paper No. 76-111, Presented at the AIAA 14th Aerospace Sciences Meeting, January 26-30, 1976, Washington, D.C. See also Leonard, D.A. and Caputo, B., "Development of a Raman System as a Combustion Diagnostic Tool", Final Technical Report, Contract F33615-75-C-2023, Air Force Aero Propulsion Laboratory, October 1975.

A12 Ferguson, G.D. (Naval Air Development Center, Warminster, PA). "Blue-Green Lasers for Underwater Applications", Presented at the SPIE 19th Annual International Technical Symposium, San Diego, August 18-22, 1975

A13 Placzek, G., in Handbuch der Radiologie edited by E. Marx, Akademische Verlagsgesellschaft, Leipzig (1934), Vol. VI, 2, p. 205, English translation UCRL-TRANS-526L (1959).

```
. FORTRAN IV G LEVEL  21

C
C       PROGRAM SWPUN     (SURFACE WAVE POLARIZATION UNBALANCE)
C
C     CALCULATION TO DETERMINE THE EFFECT OF OCEAN SURFACE WAVE SHAPE
C     ON TRANSMITTED POLARIZATION UNBALANCE, DB/BP.
C
C     FIVE WAVE SHAPES ARE CONSIDERED
C         1. SINUSOIDIAL
C         2. 3RD ORDER STOKES/GERSTNER
C         3. 4TH ORDER STOKES
C         4. 4TH ORDER GERSTNER
C         5. TROCHOIDAL
C
C     PROGRAMMED BY    - COMPUTER GENETICS CORPORATION
C                        4 LAKESIDE OFFICE PARK
C                        WAKEFIELD, MASS.          01880
C                        TELEPHONE  (617) 246-2838
C
C     PROGRAMMER       - RICHARD L. JOHNSON
C
C     DATE PROGRAMMED  - AUGUST 19, 1976
C
C     DEVELOPED FOR    - DONALD A. LEONARD
C
C     REFERENCE        - WIND WAVES BY BLAIR KINSMAN
C                        PRENTICE-HALL, INC.    1965
C
C     INPUT     AOL    - WAVE SPECIFICATION.
C                        RATIO OF WAVE AMPLITUDE TO WAVELENGTH.
C
C     OUTPUT    A/L    - WAVE SPECIFICATION.
C                        RATIO OF WAVE AMPLITUDE TO WAVELENGTH.
C               XOL    - POSITION ALONG WAVE AS A FRACTION OF WAVELENGTH.
C               Y      - WAVE AMPLITUDE AT XOL.
C               DYDX   - LOCAL SLOPE OF WAVE AT XOL.
C               H/L    - RATIO OF WAVE HEIGHT TO WAVELENGTH.
C               DBBP   - VALUE OF TRANSMITTED POLARIZATION UNBALANCE
C                        AS AVERAGED OVER A WAVE.
C
0001            IMPLICIT REAL*8(A-H,O-$),INTEGER(I-N)
0002            REAL*8 N
0003            DIMENSION AOL(50),SUM(5),Y(100,5),DYDX(5),HOL(5,50),DBEFF(5,50)
0004          1 FORMAT (F6.4)
0005         10 FORMAT (1H1/15X,'SINUSOIDAL       3RD ORDER STOKES/GERST   4TH ORDE
              1R STOKES      4TH ORDER GERSTNER          TROCHOIDAL'/
              23X,'A/L          H/L       DB/BP          H/L       DB/BP          H/L
              3 DB/BP          H/L       DB/BP          H/L       DB/BP'//
              4(1X,0PF6.4,F10.4,1PD12.3,0PF10.4,1PD12.3,0PF10.4,1PD12.3,
```

```
* FORTRAN IV G LEVEL  21

                5 0PF10.4,1PD12.3,0PF10.4,1PD12.3))
0006          11 FORMAT (1H1/1X,'A/L=',F6.4,4X,'SINUSOIDAL      3RD ORDER STOKES/GE
                1RST   4TH ORDER STOKES      4TH ORDER GERSTNER        TROCHOIDAL'/
                23X,'XOL          Y          DYDX          Y          DYDX          Y
                3   DYDX          Y          DYDX          Y          DYDX'//)
0007          12 FORMAT (1X,F6.4,5(F10.4,F12.4))
C
C         DEFINE CONSTANTS
C
0008            N=1.333
0009            A=1.0
0010            EPS=0.001
0011            TWOPI=2.0*3.1415927
0012            FOURPI=TWOPI+TWOPI
0013            SIXPI=TWOPI+FOURPI
0014            ATEPI=TWOPI+SIXPI
0015            TWOPI2=TWOPI*TWOPI
0016            TWOPI3=TWOPI*TWOPI2
0017            TWOPI4=TWOPI*TWOPI3
0018            RTOD=360.0/TWOPI
0019            K=0
C
C         INPUT A/L FOR NEXT CASE
C
0020          99 READ 1,AOL
0021            IF (AOL.LT.0.0) GO TO 104
0022            IF (K.EQ.50) GO TO 104
0023            K=K+1
0024            TAOL(K)=AOL
0025            AOL2=AOL*AOL
0026            AOL3=AOL2*AOL
0027            AOL4=AOL3*AOL
0028            RL=A/AOL
C
C         LABEL OUTPUT AND ZERO SUMMATION TABLES
C
0029            PRINT 11,AOL
0030            DO 100 I=1,5
0031            SUM(I)=0.0
0032        100 CONTINUE
C
C         CALCULATE AMPLITUDE AND SLOPE AT 100 POINTS ALONG EACH OF
C         FIVE OCEAN WAVE SHAPES.
C
0033            XOL=0.0
0034            DXOL=0.01
0035            TP=0.0
0036            DO 2 I=1,100
```

```
FORTRAN IV G LEVEL  21

C
C          SINUSOIDAL WAVE
C
0037                Y(I,1)=A*DCOS(TWOPI*XOL)
0038                DYDX(1)=-TWOPI*AOL*DSIN(TWOPI*XOL)
C
C          3RD ORDER STOKES/GERSTNER WAVE
C
0039                Y(I,2)=A*DCOS(TWOPI*XOL)+0.5*TWOPI*A*AOL*DCOS(FOURPI*XOL)
                   1       +(3.0/8.0)*TWOPI2*A*AOL2*DCOS(SIXPI*XOL)
0040                DYDX(2)=-TWOPI*AOL*DSIN(TWOPI*XOL)
                   1          -TWOPI2*AOL2*DSIN(FOURPI*XOL)
                   2          -(9.0/8.0)*TWOPI3*AOL3*DSIN(SIXPI*XOL)
C
C          4TH ORDER STOKES WAVE
C
0041                Y(I,3)=A*DCOS(TWOPI*XOL)
                   1      +(0.5*TWOPI*A*AOL+(17.0/24.0)*TWOPI3*A*AOL3)*DCOS(FOURPI*XOL)
                   2      +(3.0/8.0)*TWOPI2*A*AOL2*DCOS(SIXPI*XOL)
                   3      +(1.0/3.0)*TWOPI3*A*AOL3*DCOS(ATEPI*XOL)
0042                DYDX(3)=-TWOPI*AOL*DSIN(TWOPI*XOL)
                   1          -(TWOPI2*AOL2+(17.0/12.0)*TWOPI3*AOL4)*DSIN(FOURPI*XOL)
                   2          -(9.0/8.0)*TWOPI3*AOL3*DSIN(SIXPI*XOL)
                   3          -(4.0/3.0)*TWOPI4*AOL4*DSIN(ATEPI*XOL)
C
C          4TH ORDER GERSTNER WAVE
C
0043                Y(I,4)=A*DCOS(TWOPI*XOL)
                   1      +(0.5*TWOPI*A*AOL+(1.0/24.0)*TWOPI3*A*AOL3)*DCOS(FOURPI*XOL)
                   2      +(3.0/8.0)*TWOPI2*A*AOL2*DCOS(SIXPI*XOL)
                   3      +(1.0/3.0)*TWOPI3*A*AOL3*DCOS(ATEPI*XOL)
0044                DYDX(4)=-TWOPI*AOL*DSIN(TWOPI*XOL)
                   1          -(TWOPI2*AOL2+(1.0/12.0)*TWOPI3*AOL4)*DSIN(FOURPI*XOL)
                   2          -(9.0/8.0)*TWOPI3*AOL3*DSIN(SIXPI*XOL)
                   3          -(4.0/3.0)*TWOPI4*AOL4*DSIN(ATEPI*XOL)
C
C          TROCHOIDAL WAVE
C
0045                DT=TWOPI/1000.0
0046                T=TP
0047              101 T=T+DT
0048                V=T/TWOPI-AOL*DSIN(T)
0049                IF (V.LT.(XOL-EPS)) GO TO 101
0050                IF (V.GE.(XOL-EPS).AND.V.LE.(XOL+EPS)) GO TO 102
0051                T=T-DT
0052                DT=0.5*DT
0053                GO TO 101
0054              102 DT=TWOPI/1000.0
```

```
FORTRAN IV G LEVEL  21

0055                    TP=T
0056                    Y(I,51)=A*DCOS(TP)
0057                    T1=TP-0.5*DT
0058                    X1=RL*(T1/TWOPI-AOL*DSIN(T1))
0059                    Y1=A*DCOS(T1)
0060                    T2=TP+0.5*DT
0061                    X2=RL*(T2/TWOPI-AOL*DSIN(T2))
0062                    Y2=A*DCOS(T2)
0063                    DYDX(5)=(Y2-Y1)/(X2-X1)
                C
                C          CALCULATE THE TRANSMITTED POLARIZATION UNBALANCE, DBOBP, FOR
                C          THIS 'X' POSITION ON EACH OF THE FIVE WAVE SHAPES.
                C
0064                    DO 3 J=1,5
0065                    TI=DATAN(DYDX(J))
0066                    TT=DARSIN(DSIN(TI)/N)
0067                    DBOBP=(DTAN(TI-TT))**2
0068                    SUM(J)=SUM(J)+DBOBP
0069                  3 CONTINUE
0070                    IF (((I/2)*2.NE.I) PRINT 12,XOL,(Y(I,J),DYDX(J),J=1,5)
0071                    XOL=XOL+DXOL
0072                  2 CONTINUE
                C
                C          CALCULATE THE H/L AND AVERAGE TRANSMITTED POLARIZATION
                C          UNBALANCE, DBEFF, FOR EACH OF THE FIVE WAVE SHAPES.
                C
0073                    DO 103 J=1,5
0074                    HOL(J,K)=(Y(1,J)-Y(51,J))/RL
0075                    DBEFF(J,K)=SUM(J)/100.0
0076                103 CONTINUE
0077                    GO TO 99
                C
                C          PRINT SUMMARY OUTPUT OF A/L, H/L AND DBEFF FOR THE FIVE
                C          OCEAN WAVE SHAPES CONSIDERED.
                C
0078                104 PRINT 10,(TAOL(I),(HOL(J,I),DBEFF(J,I),J=1,5),I=1,K)
0079                    CALL EXIT
0080                    END
```

A/L	SINUSOIDAL H/L	SINUSOIDAL DB/BP	3RD ORDER STOKES/GERST H/L	3RD ORDER STOKES/GERST DB/BP	4TH ORDER STOKES H/L	4TH ORDER STOKES DB/BP	4TH ORDER GERSTNER H/L	4TH ORDER GERSTNER DB/BP	TROCHOIDAL H/L	TROCHOIDAL DB/BP
0.0010	0.0020	1.232D-06	0.0020	1.232D-06	0.0020	1.232D-06	0.0020	1.232D-06	0.0020	1.232D-06
0.0015	0.0030	2.772D-06	0.0030	2.772D-06	0.0030	2.772D-06	0.0030	2.772D-06	0.0030	2.772D-06
0.0020	0.0040	4.927D-06	0.0040	4.928D-06	0.0040	4.928D-06	0.0040	4.928D-06	0.0040	4.927D-06
0.0030	0.0060	1.109D-05	0.0060	1.109D-05	0.0060	1.109D-05	0.0060	1.109D-05	0.0060	1.109D-05
0.0040	0.0080	1.971D-05	0.0080	1.972D-05	0.0080	1.972D-05	0.0080	1.972D-05	0.0080	1.971D-05
0.0050	0.0100	3.079D-05	0.0100	3.082D-05	0.0100	3.082D-05	0.0100	3.082D-05	0.0100	3.080D-05
0.0060	0.0120	4.434D-05	0.0120	4.440D-05	0.0120	4.440D-05	0.0120	4.440D-05	0.0120	4.435D-05
0.0080	0.0160	7.881D-05	0.0160	7.901D-05	0.0160	7.901D-05	0.0160	7.901D-05	0.0160	7.887D-05
0.0100	0.0200	1.231D-04	0.0200	1.236D-04	0.0200	1.236D-04	0.0200	1.236D-04	0.0200	1.232D-04
0.0150	0.0300	2.768D-04	0.0301	2.793D-04	0.0301	2.793D-04	0.0301	2.793D-04	0.0300	2.775D-04
0.0200	0.0400	4.916D-04	0.0402	4.995D-04	0.0402	4.996D-04	0.0402	4.995D-04	0.0400	4.935D-04
0.0300	0.0600	1.103D-03	0.0608	1.144D-03	0.0608	1.145D-03	0.0608	1.144D-03	0.0600	1.113D-03
0.0400	0.0800	1.954D-03	0.0819	2.085D-03	0.0819	2.089D-03	0.0819	2.086D-03	0.0800	1.985D-03
0.0500	0.1000	3.038D-03	0.1037	3.365D-03	0.1037	3.385D-03	0.1037	3.372D-03	0.1000	3.114D-03
0.0600	0.1200	4.349D-03	0.1264	5.044D-03	0.1264	5.107D-03	0.1264	5.072D-03	0.1200	4.505D-03
0.0700	0.1400	5.878D-03	0.1502	7.194D-03	0.1502	7.368D-03	0.1502	7.283D-03	0.1400	6.171D-03
0.0710	0.1420	6.043D-03	0.1526	7.439D-03	0.1526	7.629D-03	0.1526	7.536D-03	0.1420	6.353D-03
0.0715	0.1430	6.126D-03	0.1538	7.563D-03	0.1538	7.762D-03	0.1538	7.666D-03	0.1430	6.437D-03
0.0725	0.1450	6.294D-03	0.1563	7.816D-03	0.1563	8.034D-03	0.1563	7.929D-03	0.1450	6.623D-03
0.0750	0.1500	6.722D-03	0.1625	8.473D-03	0.1625	8.744D-03	0.1625	8.618D-03	0.1500	7.101D-03
0.0800	0.1600	7.618D-03	0.1752	9.903D-03	0.1752	1.031D-02	0.1752	1.013D-02	0.1600	8.110D-03
0.0900	0.1800	9.557D-03	0.2016	1.326D-02	0.2016	1.412D-02	0.2016	1.378D-02	0.1800	1.034D-02
0.1000	0.2000	1.169D-02	0.2296	1.737D-02	0.2295	1.897D-02	0.2296	1.838D-02	0.2000	1.286D-02
0.1500	0.3000	2.479D-02	0.3999	5.160D-02	0.3999	6.427D-02	0.3999	6.177D-02	0.3000	2.804D-02
0.2000	0.4000	4.093D-02	0.6369	1.171D-01	0.6369	1.736D-01	0.6369	1.724D-01	0.4000	2.493D-02
0.3000	0.6000	7.773D-02	1.3994	3.263D-01	1.3994	4.802D-01	1.3994	4.833D-01	0.6000	1.612D-02
0.4000	0.8000	1.156D-01	2.6950	4.942D-01	2.6950	6.412D-01	2.6950	6.341D-01	0.1878	1.175D-02
0.5000	1.0000	1.515D-01	4.7011	5.935D-01	4.7011	6.935D-01	4.7011	6.891D-01	0.1623	8.728D-03
0.6000	1.2000	1.846D-01	7.5955	6.461D-01	7.5955	7.233D-01	7.5955	7.208D-01	0.1425	6.752D-03
0.8000	1.6000	2.418D-01	16.7597	7.019D-01	16.7597	7.513D-01	16.7597	7.495D-01	0.1153	4.416D-03
1.0000	2.0000	2.887D-01	31.6088	7.291D-01	31.6088	7.570D-01	31.6088	7.548D-01	0.0965	3.122D-03

PROGRAM SWPUN SUMMARY PRINTOUT

```
* FORTRAN IV G LEVEL  21

C
C       PROGRAM SWDCO      (SURFACE WAVE DEPTH CORRECTION)
C
C     CALCULATION TO DETERMINE THE EFFECT OF OCEAN SURFACE WAVE SHAPE
C     ON DEPTH.  THE DEPTH CORRECTION, DCOR, IS CALCULATED.
C
C     THREE WAVE SHAPES ARE CONSIDERED
C          1. SINUSOIDAL
C          2. 4TH ORDER STOKES
C          3. TROCHOIDAL
C
C     PROGRAMMED BY     - COMPUTER GENETICS CORPORATION
C                         4 LAKESIDE OFFICE PARK
C                         WAKEFIELD, MASS.          01880
C                         TELEPHONE  (617) 246-2838
C
C     PROGRAMMER        - RICHARD L. JOHNSON
C
C     DATE PROGRAMMED   - AUGUST 25, 1976
C
C     DEVELOPED FOR     - DONALD A. LEONARD
C
C     REFERENCE         - WIND WAVES BY BLAIR KINSMAN
C                         PRENTICE-HALL, INC.     1965
C
C     INPUT     AOL     - WAVE SPECIFICATION.
C                         RATIO OF WAVE AMPLITUDE TO WAVELENGTH.
C
C     OUTPUT    A/L     - WAVE SPECIFICATION.
C                         RATIO OF WAVE AMPLITUDE TO WAVELENGTH.
C               XOL     - POSITION ALONG WAVE AS A FRACTION OF WAVELENGTH.
C               Y       - WAVE AMPLITUDE AT XOL.
C               DYDX    - LOCAL SLOPE OF WAVE AT XOL.
C               DCOR    - LOCAL DEPTH CORRECTION AT XOL DUE TO LOCAL SLOPE.
C               H/L     - RATIO OF WAVE HEIGHT TO WAVELENGTH.
C          MINIMUM      - SMALLEST DEPTH CORRECTION ALONG THE WAVE.
C       10 PERCENT      - 10TH LARGEST DEPTH CORRECTION OF 100 VALUES
C                         CALCULATED ALONG THE WAVE.
C          AVERAGE      - AVERAGE DEPTH CORRECTION OVER THE WAVE.
C       90 PERCENT      - 90TH LARGEST DEPTH CORRECTION OF 100 VALUES
C                         CALCULATED ALONG THE WAVE.
C          MAXIMUM      - LARGEST DEPTH CORRECTION ALONG THE WAVE.
C
0001          IMPLICIT REAL*8(A-H,O-$),INTEGER(I-N)
0002          REAL*8 N
0003          DIMENSION TAOL(50),SUM(3),Y(100,3),DYDX(3),HOL(3,50),ADCOR(3,50)
0004          DIMENSION DCOR(100,3),CDCOR(100,3),SDCOR(100)
0005          DIMENSION DCORMN(3,50),DCOR10(3,50),DCOR90(3,50),DCORMX(3,50)
```

```
FORTRAN IV G LEVEL  21

0006                1 FORMAT (F6.4)
0007               10 FORMAT (1H1/12X,'DEPTH CORRECTION SUMMARY SHEET FOR A SINUSOIDAL O
                     1CEAN WAVE'///5X,'A/L        H/L        MINIMUM    10 PERCENT     AVERAG
                     2E    90 PERCENT     MAXIMUM'//(3X,0PF6.4,0PF10.4,2X,1P5D12.3))
0008               11 FORMAT (1H1/1X,'A/L=',F6.4,'                SINUSOIDAL
                     2   4TH ORDER STOKES                          TROCHOIDAL'/
                     3  3X,'XOL          Y          DYDX          DCOR          Y          DYDX
                     4       DCOR          Y          DYDX          DCOR'//)
0009               12 FORMAT (1X,0PF6.4,3(0PF12.4,0PF10.4,1PD12.3))
0010               13 FORMAT (1H1/9X,'DEPTH CORRECTION SUMMARY SHEET FOR A 4TH ORDER STO
                     1KES OCEAN WAVE'///5X,'A/L        H/L        MINIMUM    10 PERCENT     A
                     2VERAGE    90 PERCENT     MAXIMUM'//(3X,0PF6.4,0PF10.4,2X,1P5D12.3))
0011               14 FORMAT (1H1/12X,'DEPTH CORRECTION SUMMARY SHEET FOR A TROCHOIDAL O
                     1CEAN WAVE'///5X,'A/L        H/L        MINIMUM    10 PERCENT     AVERAG
                     2E    90 PERCENT     MAXIMUM'//(3X,0PF6.4,0PF10.4,2X,1P5D12.3))
                   C
                   C        DEFINE CONSTANTS
                   C
0012                      N=1.333
0013                      A=1.0
0014                      EPS=0.001
0015                      TWOPI=2.0*3.1415927
0016                      FOURPI=TWOPI+TWOPI
0017                      SIXPI=TWOPI+FOURPI
0018                      ATEPI=TWOPI+SIXPI
0019                      TWOPI2=TWOPI*TWOPI
0020                      TWOPI3=TWOPI*TWOPI2
0021                      TWOPI4=TWOPI*TWOPI3
0022                      RTOD=360.0/TWOPI
0023                      K=0
C2                 C
                   C        INPUT A/L FOR NEXT CASE
                   C
0024               99 READ 1,AOL
0025                      IF (AOL.LT.0.0) GO TO 104
0026                      IF (K.EQ.50) GO TO 104
0027                      K=K+1
0028                      TAOL(K)=AOL
0029                      AOL2=AOL*AOL
0030                      AOL3=AOL2*AOL
0031                      AOL4=AOL3*AOL
0032                      RL=A/AOL
                   C
                   C        LABEL OUTPUT AND ZERO SUMMATION TABLES
                   C
0033                      PRINT 11,AOL
0034                      DO 100 I=1,3
0035                      SUM(I)=0.0
```

```
* FORTRAN IV G LEVEL  21

0036          100 CONTINUE
                C
                C        CALCULATE AMPLITUDE AND SLOPE AT 100 POINTS ALONG EACH OF
                C        FIVE OCEAN WAVE SHAPES.
                C
0037                XOL=0.0
0038                DXOL=0.01
0039                TP=0.0
0040                DO 2 I=1,100
                C
                C        SINUSOIDAL WAVE
                C
0041                Y(I,1)=A*DCOS(TWOPI*XOL)
0042                DYDX(1)=-TWOPI*AOL*DSIN(TWOPI*XOL)
                C
                C        4TH ORDER STOKES WAVE
                C
0043                Y(I,2)=A*DCOS(TWOPI*XOL)
                   1      +(0.5*TWOPI*A*AOL+(17.0/24.0)*TWOPI3*A*AOL3)*DCOS(FOURPI*XOL)
                   2      +(3.0/8.0)*TWOPI2*A*AOL2*DCOS(SIXPI*XOL)
                   3      +(1.0/3.0)*TWOPI3*A*AOL3*DCOS(ATEPI*XOL)
0044                DYDX(2)=-TWOPI*AOL*DSIN(TWOPI*XOL)
                   1         -(TWOPI2*AOL2+(17.0/12.0)*TWOPI3*AOL4)*DSIN(FOURPI*XOL)
                   2         -(9.0/8.0)*TWOPI3*AOL3*DSIN(SIXPI*XOL)
                   3         -(4.0/3.0)*TWOPI4*AOL4*DSIN(ATEPI*XOL)
                C
                C        TROCHOIDAL WAVE
                C
0045                DT=TWOPI/1000.0
0046                T=TP
0047          101   T=T+DT
0048                V=T/TWOPI-AOL*DSIN(T)
0049                IF (V.LT.(XOL-EPS)) GO TO 101
0050                IF (V.GE.(XOL-EPS).AND.V.LE.(XOL+EPS)) GO TO 102
0051                T=T-DT
0052                DT=0.5*DT
0053                GO TO 101
0054          102   DT=TWOPI/1000.0
0055                TP=T
0056                Y(I,3)=A*DCOS(TP)
0057                T1=TP-0.5*DT
0058                X1=RL*(T1/TWOPI-AOL*DSIN(T1))
0059                Y1=A*DCOS(T1)
0060                T2=TP+0.5*DT
0061                X2=RL*(T2/TWOPI-AOL*DSIN(T2))
0062                Y2=A*DCOS(T2)
0063                DYDX(3)=(Y2-Y1)/(X2-X1)
                C
```

C3

AD-A066 741 COMPUTER GENETICS CORP WAKEFIELD MASS F/G 8/10
SUMMARY AND EXPERIMENTAL PLAN FOR REMOTE SENSING OF SUBSURFACE --ETC(U)
JUL 77 D A LEONARD, B CAPUTO N00014-76-C-1007
UNCLASSIFIED CGC-RN105-77 NL

2 OF 2
ADA
066741

END
DATE
FILMED
5-79
DDC

```
C          CALCULATE THE DEPTH CORRECTION, DCOR, FOR THIS 'X' POSITION
C          ON EACH OF THE THREE WAVE SHAPES.
C
0064            DO 3 J=1,3
0065            TI=DATAN(DYDX(J))
0066            TT=DARSIN(DSIN(TI)/N)
0067            TD=DABS(TI)-DABS(TT)
0068            DCOR(I,J)=1.0-DCOS(TD)
0069            CDCOR(I,J)=DCOR(I,J)
0070            SUM(J)=SUM(J)+DCOR(I,J)
0071          3 CONTINUE
0072            IF ((I/2)*2.NE.I) PRINT 12,XOL,(Y(I,J),DYDX(J),DCOR(I,J),J=1,3)
0073            XOL=XOL+DXOL
0074          2 CONTINUE
C
C          CALCULATE THE H/L AND AVERAGE DEPTH CORRECTION VALUE
C          FOR EACH WAVE SHAPE.
C
0075            DO 103 J=1,3
0076            HOL(J,K)=(Y(1,J)-Y(51,J))/RL
0077            ADCOR(J,K)=SUM(J)/100.0
C
C          SORT IN ASCENDING ORDER THE 100 DEPTH CORRECTION VALUES
C          FOR EACH WAVE SHAPE.
C
0078            DO 106 M=1,100
0079            VAL=CDCOR(I,J)
0080            INDEX=1
0081            DO 105 I=2,100
0082            IF (VAL.LE.CDCOR(I,J)) GO TO 105
0083            VAL=CDCOR(I,J)
0084            INDEX=I
0085        105 CONTINUE
0086            CDCOR(INDEX,J)=2.0
0087            SDCOR(M)=VAL
0088        106 CONTINUE
C
C          SAVE THE MINIMUM, 10 PERCENT, 90 PERCENT AND MAXIMUM DEPTH
C          CORRECTION VALUES OVER EACH OF THE THREE WAVE SHAPES.
C
0089            DCORMN(J,K)=SDCOR(1)
0090            DCOR10(J,K)=SDCOR(10)
0091            DCOR90(J,K)=SDCOR(90)
0092            DCORMX(J,K)=SDCOR(100)
0093        103 CONTINUE
0094            GO TO 99
C
C          PRINT SUMMARY SHEET OF DEPTH CORRECTIONS FOR EACH OF THE
```

```
• FORTRAN IV G LEVEL  21

C
C          THREE WAVE SHAPES CONSIDERED VS A/L AND H/L.
0095          104 PRINT 10,(TAOL(I),HOL(1,I),DCORMN(1,I),DCOR10(1,I),ADCOR(1,I),
                 1 DCOR90(1,I),DCORMX(1,I),I=1,K)
0096               PRINT 13,(TAOL(I),HOL(2,I),DCORMN(2,I),DCOR10(2,I),ADCOR(2,I),
                 1 DCOR90(2,I),DCORMX(2,I),I=1,K)
0097               PRINT 14,(TAOL(I),HOL(3,I),DCORMN(3,I),DCOR10(3,I),ADCOR(3,I),
                 1 DCOR90(3,I),DCORMX(3,I),I=1,K)
0098               CALL EXIT
0099               END
```

C5

DEPTH CORRECTION SUMMARY SHEET FOR A SINUSOIDAL OCEAN WAVE

A/L	H/L	MINIMUM	10 PERCENT	AVERAGE	90 PERCENT	MAXIMUM
0.0010	0.0020	0.0	1.935D-08	6.159D-07	1.189D-06	1.232D-06
0.0015	0.0030	0.0	4.354D-08	1.386D-06	2.674D-06	2.772D-06
0.0020	0.0040	0.0	7.740D-08	2.464D-06	4.754D-06	4.927D-06
0.0030	0.0060	0.0	1.742D-07	5.543D-06	1.070D-05	1.109D-05
0.0040	0.0080	0.0	3.096D-07	9.854D-06	1.901D-05	1.971D-05
0.0050	0.0100	0.0	4.838D-07	1.540D-05	2.971D-05	3.079D-05
0.0060	0.0120	0.0	6.966D-07	2.217D-05	4.278D-05	4.433D-05
0.0080	0.0160	0.0	1.238D-06	3.940D-05	7.603D-05	7.879D-05
0.0100	0.0200	0.0	1.935D-06	6.155D-05	1.188D-04	1.231D-04
0.0150	0.0300	0.0	4.354D-06	1.384D-04	2.669D-04	2.766D-04
0.0200	0.0400	0.0	7.740D-06	2.457D-04	4.737D-04	4.909D-04
0.0300	0.0600	0.0	1.741D-05	5.509D-04	1.061D-03	1.100D-03
0.0400	0.0800	0.0	3.095D-05	9.747D-04	1.875D-03	1.942D-03
0.0500	0.1000	0.0	4.836D-05	1.514D-03	2.907D-03	3.010D-03
0.0600	0.1200	0.0	6.963D-05	2.164D-03	4.147D-03	4.293D-03
0.0700	0.1400	0.0	9.475D-05	2.920D-03	5.582D-03	5.777D-03
0.0710	0.1420	0.0	9.748D-05	3.001D-03	5.736D-03	5.936D-03
0.0715	0.1430	0.0	9.885D-05	3.042D-03	5.814D-03	6.016D-03
0.0725	0.1450	0.0	1.016D-04	3.125D-03	5.970D-03	6.178D-03
0.0750	0.1500	0.0	1.088D-04	3.336D-03	6.370D-03	6.590D-03
0.0800	0.1600	0.0	1.237D-04	3.777D-03	7.201D-03	7.448D-03
0.0900	0.1800	0.0	1.566D-04	4.728D-03	8.988D-03	9.293D-03
0.1000	0.2000	0.0	1.932D-04	5.768D-03	1.093D-02	1.129D-02
0.1500	0.3000	0.0	4.340D-04	1.206D-02	2.241D-02	2.310D-02
0.2000	0.4000	0.0	7.696D-04	1.961D-02	3.559D-02	3.657D-02
0.3000	0.6000	0.0	1.719D-03	3.597D-02	6.224D-02	6.361D-02
0.4000	0.8000	0.0	3.026D-03	5.180D-02	8.572D-02	8.726D-02
0.5000	1.0000	0.0	4.670D-03	6.605D-02	1.052D-01	1.067D-01
0.6000	1.2000	0.0	6.624D-03	7.857D-02	1.210D-01	1.226D-01
0.8000	1.6000	0.0	1.135D-02	9.910D-02	1.448D-01	1.462D-01
1.0000	2.0000	0.0	1.696D-02	1.150D-01	1.615D-01	1.628D-01

DEPTH CORRECTION SUMMARY SHEET FOR A 4TH ORDER STOKES OCEAN WAVE

A/L	H/L	MINIMUM	10 PERCENT	AVERAGE	90 PERCENT	MAXIMUM
0.0010	0.0020	0.0	1.984D-08	6.159D-07	1.194D-06	1.232D-06
0.0015	0.0030	0.0	4.521D-08	1.386D-06	2.693D-06	2.771D-06
0.0020	0.0040	0.0	8.140D-08	2.464D-06	4.798D-06	4.925D-06
0.0030	0.0060	0.0	1.879D-07	5.545D-06	1.080D-05	1.109D-05
0.0040	0.0080	0.0	3.427D-07	9.860D-06	1.913D-05	1.973D-05
0.0050	0.0100	0.0	5.495D-07	1.541D-05	2.977D-05	3.084D-05
0.0060	0.0120	0.0	8.123D-07	2.220D-05	4.306D-05	4.443D-05
0.0080	0.0160	0.0	1.523D-06	3.950D-05	7.706D-05	7.909D-05
0.0100	0.0200	0.0	2.511D-06	6.179D-05	1.196D-04	1.239D-04
0.0150	0.0301	0.0	6.491D-06	1.396D-04	2.711D-04	2.809D-04
0.0200	0.0402	0.0	1.089D-05	2.497D-04	4.867D-04	5.049D-04
0.0300	0.0608	0.0	1.953D-05	5.715D-04	1.131D-03	1.175D-03
0.0400	0.0819	0.0	2.704D-05	1.042D-03	2.128D-03	2.211D-03
0.0500	0.1037	0.0	5.538D-05	1.685D-03	3.599D-03	3.784D-03
0.0600	0.1264	0.0	5.402D-05	2.537D-03	5.727D-03	6.196D-03
0.0700	0.1502	0.0	3.935D-05	3.648D-03	8.875D-03	9.822D-03
0.0710	0.1526	0.0	3.724D-05	3.775D-03	9.338D-03	1.026D-02
0.0715	0.1538	0.0	3.615D-05	3.840D-03	9.576D-03	1.049D-02
0.0725	0.1563	0.0	3.389D-05	3.973D-03	1.007D-02	1.096D-02
0.0750	0.1625	0.0	2.794D-05	4.319D-03	1.117D-02	1.225D-02
0.0800	0.1752	0.0	1.550D-05	5.080D-03	1.330D-02	1.516D-02
0.0900	0.2016	0.0	8.369D-07	6.902D-03	2.004D-02	2.267D-02
0.1000	0.2296	0.0	2.037D-05	9.175D-03	2.859D-02	3.259D-02
0.1500	0.3999	0.0	3.939D-04	2.839D-02	9.851D-02	1.096D-01
0.2000	0.6369	0.0	4.365D-03	7.195D-02	1.663D-01	1.758D-01
0.3000	1.3994	0.0	6.421D-02	1.729D-01	2.238D-01	2.283D-01
0.4000	2.6950	0.0	1.648D-01	2.169D-01	2.398D-01	2.419D-01
0.5000	4.7011	0.0	2.171D-01	2.286D-01	2.454D-01	2.463D-01
0.6000	7.5955	0.0	2.353D-01	2.360D-01	2.476D-01	2.480D-01
0.8000	16.7597	0.0	2.451D-01	2.427D-01	2.491D-01	2.492D-01
1.0000	31.6088	0.0	2.474D-01	2.439D-01	2.495D-01	2.496D-01

DEPTH CORRECTION SUMMARY SHEET FOR A TROCHOIDAL OCEAN WAVE

A/L	H/L	MINIMUM	10 PERCENT	AVERAGE	90 PERCENT	MAXIMUM
0.0010	0.0020	0.0	2.159D-08	6.159D-07	1.194D-06	1.232D-06
0.0015	0.0030	0.0	4.888D-08	1.386D-06	2.696D-06	2.771D-06
0.0020	0.0040	0.0	8.746D-08	2.464D-06	4.797D-06	4.926D-06
0.0030	0.0060	0.0	1.993D-07	5.543D-06	1.082D-05	1.108D-05
0.0040	0.0080	0.0	3.588D-07	9.854D-06	1.916D-05	1.972D-05
0.0050	0.0100	0.0	5.679D-07	1.540D-05	2.981D-05	3.082D-05
0.0060	0.0120	1.388D-17	8.284D-07	2.217D-05	4.302D-05	4.439D-05
0.0080	0.0160	2.776D-17	1.658D-06	3.943D-05	7.704D-05	7.894D-05
0.0100	0.0200	4.163D-17	2.600D-06	6.161D-05	1.195D-04	1.236D-04
0.0150	0.0300	8.327D-17	6.614D-06	1.387D-04	2.700D-04	2.791D-04
0.0200	0.0400	1.527D-16	1.112D-05	2.466D-04	4.825D-04	4.988D-04
0.0300	0.0600	3.053D-16	2.085D-05	5.560D-04	1.102D-03	1.140D-03
0.0400	0.0800	4.857D-16	2.853D-05	9.902D-04	2.001D-03	2.071D-03
0.0500	0.1000	6.939D-16	6.311D-05	1.552D-03	3.214D-03	3.332D-03
0.0600	0.1200	9.159D-16	7.745D-05	2.240D-03	4.790D-03	4.976D-03
0.0700	0.1400	1.138D-15	8.998D-05	3.062D-03	6.735D-03	7.080D-03
0.0710	0.1420	1.166D-15	9.177D-05	3.152D-03	7.007D-03	7.329D-03
0.0715	0.1430	1.180D-15	9.267D-05	3.193D-03	7.113D-03	7.453D-03
0.0725	0.1450	1.193D-15	9.447D-05	3.284D-03	7.307D-03	7.704D-03
0.0750	0.1500	1.249D-15	9.203D-05	3.519D-03	7.852D-03	8.346D-03
0.0800	0.1600	1.374D-15	1.004D-04	4.013D-03	9.139D-03	9.783D-03
0.0900	0.1800	1.596D-15	1.086D-04	5.101D-03	1.233D-02	1.324D-02
0.1000	0.2000	1.818D-15	1.147D-04	6.318D-03	1.573D-02	1.769D-02
0.1500	0.3000	2.887D-15	1.965D-04	1.320D-02	3.595D-02	8.729D-02
0.2000	0.4000	3.803D-15	1.240D-04	1.187D-02	3.284D-02	6.722D-02
0.3000	0.6000	5.246D-15	1.032D-04	7.846D-03	2.124D-02	3.254D-02
0.4000	0.1878	6.287D-15	1.238D-04	5.771D-03	1.548D-02	2.189D-02
0.5000	0.1623	7.064D-15	1.022D-04	4.308D-03	1.132D-02	1.527D-02
0.6000	0.1425	7.674D-15	8.495D-05	3.343D-03	8.590D-03	1.134D-02
0.8000	0.1153	8.549D-15	5.838D-05	2.194D-03	5.508D-03	7.104D-03
1.0000	0.0965	9.145D-15	4.180D-05	1.554D-03	3.882D-03	4.892D-03

APPENDIX D

DEPOLARIZATION CALCULATIONS

This appendix summarizes calculations which show the scaling of the depolarization produced by small angle scattering during transmission of light through natural ocean waters as a noise source in addition to the depolarization produced by the water Raman scattering.

Consider a beam of light with polarized component I_{p_o} and unpolarized component I_{u_o} incident upon a transmission medium characterized by a differential depolarization coefficient ρ_s defined by the following expression:

$$\frac{dI_p}{dx} = -\rho_s I_p$$

At some transmission distance, X_1, the polarized component will become

$$I_{p_1} = I_{p_o} e^{-\rho_s X_1}$$

and the unpolarized component will increase to become

$$I_{u_1} = I_{u_o} + I_{p_o} (1 - e^{-\rho_s X_1})$$

(The above argument neglects attenuation and assumes a homogeneous medium.)

If at the transmission distance, X_1, the Raman backscattering process is now allowed to occur the polarized component I_{p_1} will be converted via the Raman process into two orthogonal polarization components, I_A and I_B

where $\rho_R = I_A / I_B$ and $I_A + I_B = I_{p_1}$

The resultant polarized and unpolarized components present following the Raman process are therefore

$$I_{p_2} = \frac{1 - \rho_R}{1 + \rho_R} I_{p_1}$$

$$I_{u_2} = I_{u_1} + \frac{2\rho_R}{1 + \rho_R} I_{p_1}$$

If the receiver is co-located with the transmitter, the Raman scattered light undergoes further depolarization during transit through the water from the transmission distance, X_1, back to the transmitter/receiver location. The return signal is thus

$$I_{p_s} = I_{p_2} e^{-\rho_s X_1}$$

$$I_{u_s} = I_{u_2} + I_{p_2} (1 - e^{-\rho_s X_1})$$

Or expressing the return signal in terms of the initial conditions

$$I_{p_s} = I_{p_o} \left(\frac{1 - \rho_R}{1 + \rho_R} \right) e^{-2\rho_s X_1}$$

$$I_{u_s} = I_{u_o} + I_{p_o} \left[1 - \left(\frac{1 - \rho_R}{1 + \rho_R} \right) e^{-2\rho_s X_1} \right]$$

Analyzers sensitive to orthogonal polarization components would then detect for maximum polarization ratio, two polarization components, I_{M_1} and I_{M_2}, as follows:

$$I_{M_1} = I_{p_s} + \frac{1}{2} I_{u_s}$$

$$I_{M_2} = \frac{1}{2} I_{u_s}$$

where the overall depolarization ratio for the two-way water transmission and the Raman process may be states as

$$\rho = \frac{I_{M2}}{I_{M1}} = 1 - \frac{2\left(\frac{1-\rho_R}{1+\rho_R}\right) e^{-2\rho_s X_1}}{1+\left(\frac{1-\rho_R}{1+\rho_R}\right) e^{-2\rho_s X_1} + \frac{I_{u_o}}{I_{p_o}}}$$

APPENDIX E

(This research note will appear in Geophysical Research Letters, July 1977.)

CGC-RN102-77

EXPERIMENTAL REMOTE SENSING OF SUBSURFACE TEMPERATURE IN NATURAL OCEAN WATER

D. A. Leonard, B. Caputo and R. L. Johnson

Computer Genetics Corporation, Lakeside Office Park, Wakefield, Massachusetts 01880

F. E. Hoge

NASA Wallops Flight Center, Wallops Island, Virginia 23337

Abstract. A remote sensing laser Raman backscattering technique has made the first field measurements, from a boat, of subsurface temperature in natural ocean waters. These results and the measurement systems rapidly developing from them open wide areas of exploitation. The technique utilizes the observation of the 3400 cm^{-1} O-H stretching Raman band of liquid water. The spectral data were analyzed to obtain the subsurface water temperature in accordance with previous laboratory studies. The importance of such a measurement by the Raman scattering technique is that it now enables depth resolved profiles of ocean water temperature to be obtained by remote sensing from airborne platforms that can be adapted for application to many problem areas of physical oceanography, meteorology, climatology, ocean technology, and thermal discharge management. An accuracy of $\pm 2^{\circ}C$ has been obtained in the initial field experiments. A more refined system has been designed which will permit accuracies of better than $\pm 1^{\circ}C$ in the first one or two optical attenuation lengths of depth.

The purpose of this communication is to report the first successful depth resolved remote sensing measurements of subsurface ocean water temperature in a boatborne field experiment. Such measurements have strong implications for research and technology in the general areas of ocean and coastal physics, oceanography and weather and climate prediction and in thermal pollution management. The temperature measurement was obtained by spectral analysis of the 3400 cm^{-1} O-H stretching Raman band of liquid water in accordance with previously reported laboratory experiments [Walrafen, 1961; Schwiesow, 1971; Chang, et al, 1974].

The physical basis of the measurement is the fact that (a) liquid water exists in at least two forms, monomers and dimers; (b) the two forms are in chemical equilibrium as a function of temperature; (c) the O-H Raman stretching frequency is significantly different for the monomer and dimer forms; (d) the relative concentration of monomer vs. dimer can be determined from the Raman spectrum and, thus, the temperature can be inferred.

The major advantage of the Raman scattering remote sensing technique, especially when adapted to airborne versions, is that it can rapidly and economically measure subsurface water temperature profiles over large areas. As such it has direct application to the elucidation of such specific temperature related problems (among others) as input to sea-air interaction modeling, the physics of oceanic mesoscale systems, behavior of ocean fronts and other mixed layer dynamics, synoptic behavior of sound propagation, monitoring of thermal discharges and validation of thermal discharge models, etc.

A laser Raman lidar system was assembled and operated to obtain Raman spectra of ocean water aboard the Computer Genetics Corporation research vessel Makai. The purpose of the effort was to demonstrate remote subsurface temperature measurements in natural waters. Although laboratory experiments had been performed previously, Raman temperature measurements of natural ocean water had never before been obtained under in situ conditions and there were unanswered questions as to the extent to which naturally occurring interferences, such as fluorescence, would place a limit on the accuracy and the resolution of the laser Raman technique especially in coastal zones. An experimental program has been designed to answer these questions. This paper reports initial results.

The block diagram of the laser Raman system that was operated aboard the Makai is shown in Figure 1. The laser source was a pulsed nitrogen laser operating at a wavelength of 337.1 nanometers and producing pulses of 100 kilowatts peak power with an effective pulse duration of 10 nanoseconds at a pulse repetition rate of 500 Hertz.

The output from the laser is passed through an interference filter which passes the 337.1 nm laser line with high efficiency but blocks spontaneous emission occurring in the laser gas discharge in the O-H Raman spectral region near 3800 Å. An attenuator is also placed in the laser beam to provide a beam power attenuation of the order of X100 so that a photon counting detection system previously employed in atmospheric Raman measurement applications system could be used in the liquid water studies.

As shown in the block diagram a bistatic arrangement of the transmitter and receiver optics functions to define a volume of subsurface water from which the laser Raman scattering is detected. Operation in such a bistatic mode is adequate for experimental studies in the first few tens of meters of depth. This configuration is being modified for deeper penetration application by utilizing electronic range gating techniques and a more suitable blue-green laser wavelength.

The photons collected by the receiver optics are passed through a double 1/4 meter focal length scanning spectrometer having a 0.5 nanometer spectral resolution. The wavelength scanning of the spectrometer is controlled by the computer. The function of the spectrometer is to produce a spectral scan of the liquid water Raman O-H stretching band with sufficient resolution so that the monomer and dimer components can be resolved and a temperature determined.

The Raman photon output from the spectrometer is detected by a RCA 1P128 photomultiplier and amplified by an Ortec Model 454 timing filter amplifier. The conditioned Raman photon signal and a gate pulse suitably synchronized and delayed with respect to the laser firing are combined in a coincidence circuit the

output from which is recorded using direct memory access (DMA) techniques with a Data General NOVA 1200 computer. The number of pulses occurring during the same data taking interval is also recorded. The ratio of the Raman photons to laser pulses recorded over a given time interval is the basic data obtained.

The data taking is fully automated. The computer can be directed through the teletype (TTY) to specify the number of laser pulses over which to record data at each wavelength and the maximum and minimum wavelengths and the wavelength increments of each spectral scan. The data obtained are printed on the TTY in tabular form listing "wavelength", "data", "cumulative data" and "drift". Successive rapid spectral scans to construct a "cumulative data" record allows the spectral information to be added coherently, thus, increasing the signal to noise ratio. The "drift" data record is a real time diagnostic that allows the operator to easily recognize during an experiment the occurrence of large error signals as soon as they may occur.

Initial Raman spectral data have been obtained from the research vessel Makai on November 3, 5 and 6, 1976 and March 26, 27 and 30, 1977 at various depths from the surface to 10 meters below the surface in the Annisquam River, a tidal estuary in Massachusetts. A typical sample of such data obtained at a depth of 1 meter below the surface is shown in Figure 2. The measurements were made under a high tidal flow condition in waters polluted by industrial and other urban runoff. It was estimated that the diffuse absorption coefficient was of the order $K = 0.3\ m^{-1}$. The range limitation in this prototype bistatic experiment was a geometrical one due to the inability to spatially resolve the intersection of the focussed spectrometer slit on the laser beam at depths greater than 10 meters.

Figure 2 is a plot of the number of Raman photoelectrons collected per 0.5 nanometer spectral interval per 10,000 laser pulses as a function of wavelength. Shown are two sets of data, the dashed curve obtained as an instrument calibration in the laboratory with a water sample at 22°C and the solid curve obtained in the Annisquam River water at 6°C, according to "ground truth" temperature readings obtained with a pair of calibrated mercury thermometers.

A temperature can be obtained from the Raman spectra by comparing the height of the band contour at the peak, which corresponds to mostly monomer contributions, to the height of the contour at the inflection point on the short wavelength side which corresponds to mostly dimer contributions. These spectral features are labeled monomer and dimer respectively on Figure 2. A scale showing the height of the dimer inflection point as a function of temperature has been calculated from previously published laboratory data [Walrafen, 1961] and is shown on Figure 2 as a reference. Based on this scale an Annisquam River temperature of 4°C is inferred from the spectra and is consistent with the ground truth temperature of 6°C to within the shot noise limited statistical precision of the Raman measurement which was ±2°C.

Based on the results of the initial experimental field measurements, the performance of a fully developed airborne laser Raman water temperature measurement system can now be estimated with a high degree of confidence using standard lidar engineering calculations. The operating map of Figure 3 has been calculated for a typical open ocean measurement situation with a mixed layer depth of 100 meters. The basic parameters on the map are the number of Raman photoelectrons collected as the ordinate with the depth as measured in attenuation lengths displayed on the abscissa. The derived quantities of temperature precision in °C and the depth in meters as a function of water quality are also shown as alternate ordinate and abscissa quantities respectively. An experimentally measured [Slusher and Derr, 1975] cross-section of $4.5 \times 10^{-29}\ cm^2/molecule\text{-}sr$ was used in the calculations.

The operating lines on the map are drawn for various values of the parameter M where

$$M = \left(\frac{P_L}{20}\right)\left(\frac{\Delta h}{10}\right)\left(\frac{1}{R}\right)^2 T \qquad (1)$$

and P_L is the averaged laser power in watts, Δh is the depth resolution in meters, R is the altitude of the aircraft in kilometers and T is the integration time of the measurement in seconds. Thus, for example, for a system with $P_L = 0.2$ watts, $\Delta h = 10$ meters, $R = 1$ kilometer and $T = 1$ second, the map parameter would be $M = 0.01$. This means that with such a system the allowed region of the operating map of Figure 3 is to the left of the line labeled $M = 0.01$. A typical operating point is shown corresponding to a temperature accuracy of 1°C and a depth penetration of 60 meters.

Also shown on the operating map is an upper boundary labeled "volume depolarization interference limit". This represents the most significant interference to the measurement and is caused by depolarization due to transmission of light through natural waters. Analysis of published data [Duntley, 1971] has shown that the depolarization effect will produce an uncertainty in the measurement of 0.1°C per attenuation length.

Acknowledgements. This work was supported in part by NASA Wallops Flight Center and the Office of Naval Research.

References

Chang, C. H., Young, L. A. and Leonard, D. A., Remote measurement of fluid temperature by Raman scattered radiation, U.S. Patent 3,986,775 filed December 26, 1974.

Duntley, S. Q., Underwater lighting by submerged lasers and incandescent sources, Scripps Institution of Oceanography Report SIO-71-1, June 1971.

Schwiesow, R. L., Raman scattering studies of pollutant systems, AIAA Paper 7-1086, November 1971.

Slusher, R. B. and Derr, V. E., Temperature dependence and cross-sections of some Stokes and anti-Stokes Raman lines in ice, Applied Optics, 14, 2116 (1975).

Walrafen, G. E., J. Chem. Phys., 55, 768 (1961).

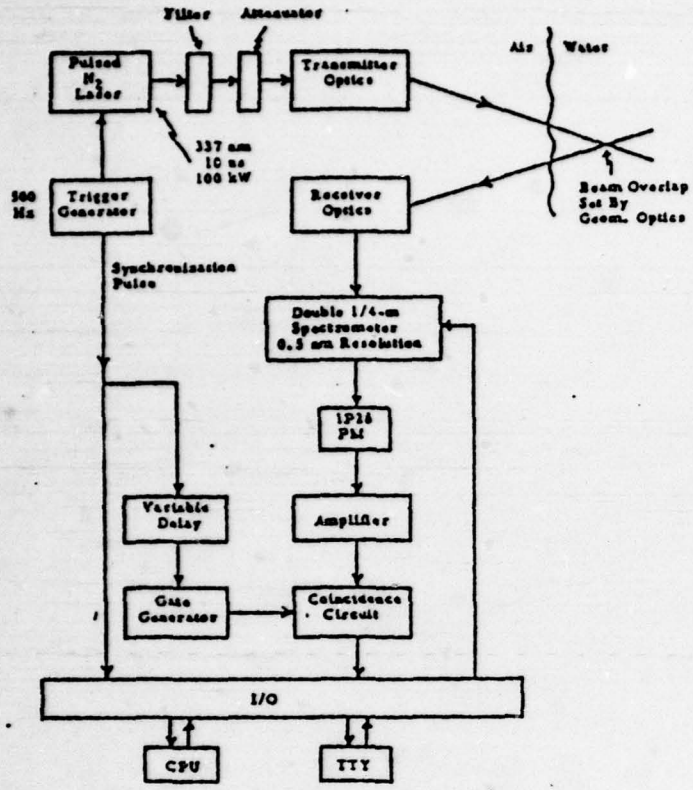

Fig. 1. Block diagram of laser Raman system currently operational on research vessel Makai.

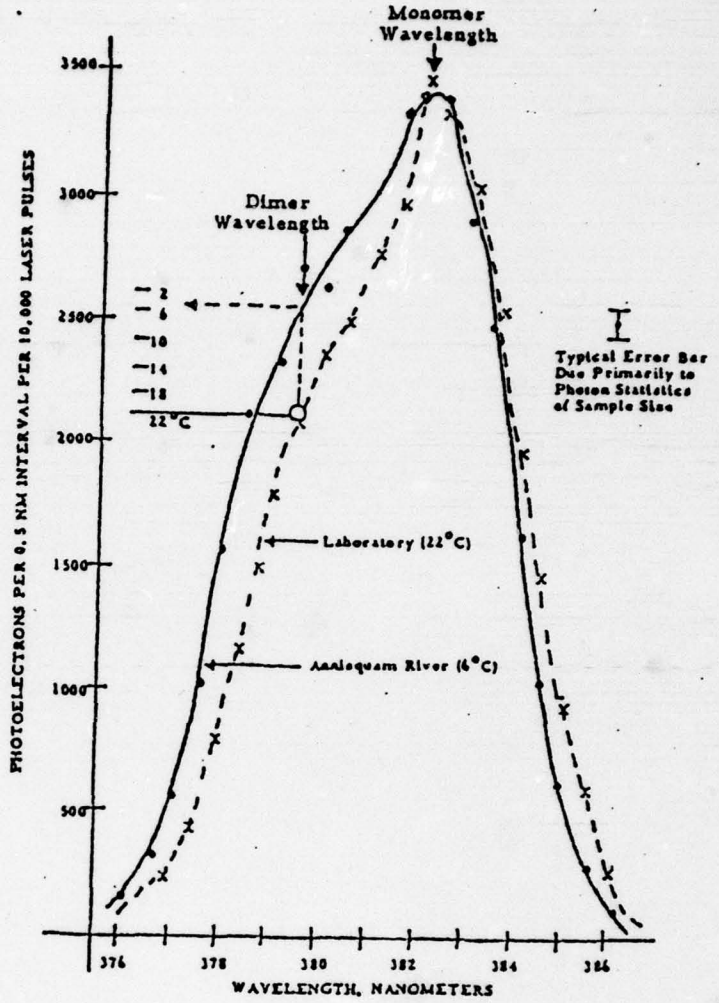

Fig. 2. Raman spectral data for liquid water.

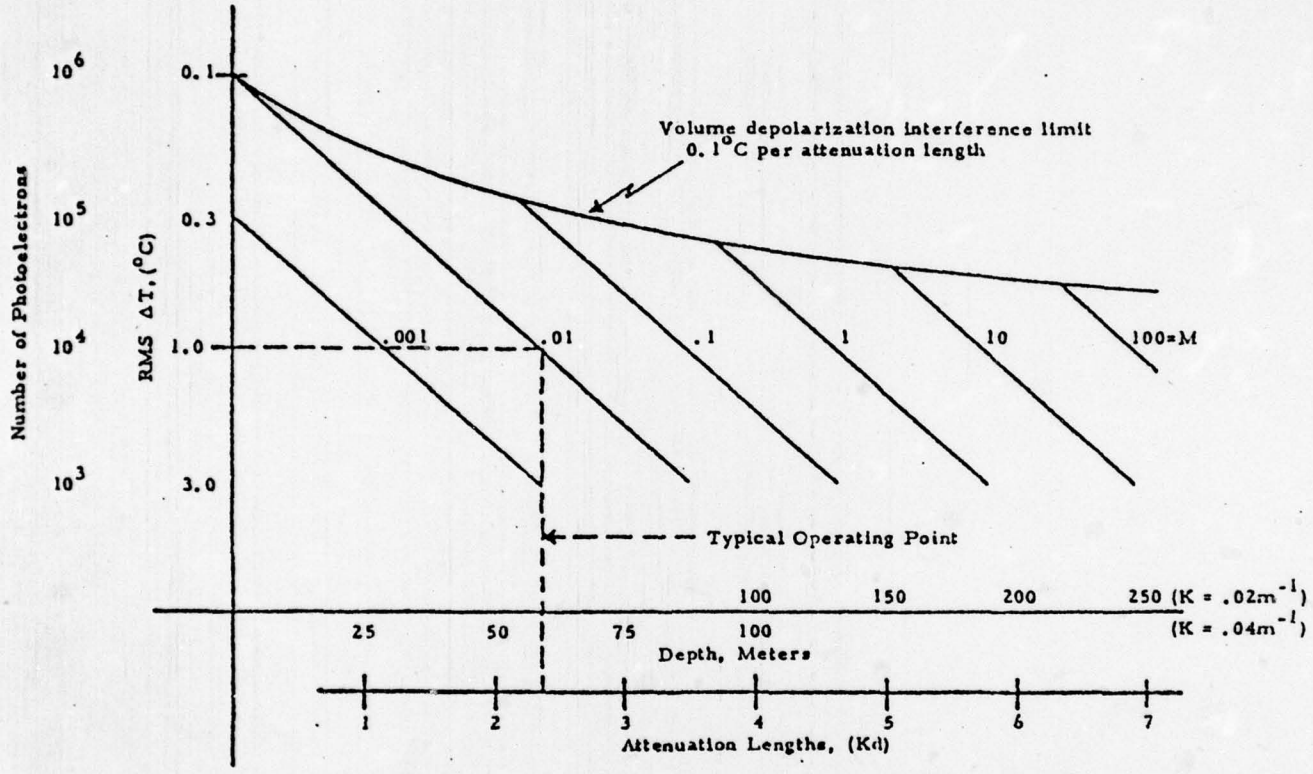

Fig. 3. Typical system operating map (100 meter mixed layer).